POLYTHIOURETHANES FOR ADVANCED APPLICATIONS

by

Gregory Ellson

APPROVED BY SUPERVISORY COMMITTEE:

_____

Dr. Walter E. Voit, Chair

_____

Dr. Yves J. Chabal

_____

Dr. Ray A. Baughman

_____

Dr. Ronald A. Smaldone

_____

Dr. Matthew Di Prima

POLYTHIOURETHANES FOR ADVANCED APPLICATIONS

by

GREGORY ELLSON, MS

DISSERTATION

Presented to the Faculty of

The University of Texas at Dallas

in Partial Fulfillment

of the Requirements

for the Degree of

DOCTOR OF PHILOSOPHY IN

MATERIALS SCIENCE AND ENGINEERING

THE UNIVERSITY OF TEXAS AT DALLAS

August 2017

ACKNOWLEDGMENTS

This work would never have been possible without the efforts and support of my family, friends, and colleagues. I want to point out my parents and loved ones who have been infinitely patient and understanding during my graduate studies. Individuals such as Walter Voit, Reena Schellenberg, and the McDermott family were instrumental in enabling my growth as a researcher. Special thanks go out to the small army of undergraduate, graduate, post-doctoral researchers, and research scientists who made up for my lack of skill, time, or patience by helping gather the data presented here.

June 2017

POLYTHIOURETHANES FOR ADVANCED APPLICATIONS

Gregory Ellson, PhD
The University of Texas at Dallas, 2017

Supervising Professor: Walter E. Voit

Photopolymer systems, such as those based on acrylate or thiol-ene chemistries, see widespread use due to the utility and convenience in the ability to rapidly cure the resin via light exposure. These materials are used in fields such as lithography, medicine, adhesives, and printing. However, these materials have drawbacks that limit their expansion into certain areas. Both acrylic and thiol-ene photopolymers tend to have poor mechanical strength and inadequate thermal performance for use in additive manufacturing and softening bioelectronics. Thiol-isocyanate resins have potential to demonstrate the mechanical and thermal properties needed in these fields, but an effective photo-curing system has been elusive. This work presents the design, synthesis, and effectiveness of quaternary ammonium salts as photo-catalysts for thiol-isocyanate resins. Photopolymer resins are designed which increase the toughness of photopolymer 3D printing systems by an order of magnitude, and the heat deflection temperature by over two times. This brings performance in-line with commonly used engineering polymers. Resins are also designed which exhibit improved softening and durability as substrates for bioelectronics devices. Functional intracortical probes are shown to minimize micromotion induced stresses and successfully record neuronal activity. Further applications in fused filament

fabrication and dielectric elastomer actuators are explored and validated, showing that thiol-isocyanate photopolymer resins might have wide-ranging use in multiple industries.

TABLE OF CONTENTS

LIST OF FIGURES

LIST OF TABLES

CHAPTER 1

INTRODUCTION

1.1 Motivation

The objective of this research is to use thiol-isocyanate click chemistry to solve or mitigate fundamental materials challenges in the emerging areas of 3D printing, bioelectronics, and artificial muscles. Photopolymer resins for 3D printing known as stereolithography (SLA) tend to have poor mechanical performance due to processing and materials limitations often resulting from the use of acrylate chemistry. Parts made via SLA tend to be fragile or have poor thermal resistance. Interpenetrating networks have improved the thermomechanical performance to a degree, but preferred systems in this space require extensive thermal post-treatment to obtain the final part properties. This has resulted in very limited adoption of 3D printing for end-use applications. Bioelectronics have traditionally relied on substrates such as tungsten or silicon for easier fabrication of microelectronics, but a growing body of evidence suggests that these rigid materials are poorly suited for chronic use in the human body. Softening polymer substrates which more closely match the modulus of human tissue have shown promising results for chronic behavior. However, the materials used thus far suffer from frequent mechanical failure, degradation *in vivo*, and do not fully soften to match neural tissue. Artificial muscles have promised to expand robotics for some time, but an effective low-cost approach has eluded researchers thus far. One of the more promising routes, dielectric elastomer actuators, has demonstrated power densities surpassing that of human muscle. However, the voltages required to actuate these materials is typically in the kV range due to the poor dielectric behavior of the polymers used. Materials with high dielectric constants which preserve the mechanical

performance necessary for effective actuation have similarly been elusive. Each of these fields stands to benefit from the unique chemical, mechanical, and electrical properties of properly prepared and processed thiourethane polymers.

1.2 Thiol-Isocyanate & Thiol-"Click" Chemistry

The thiol-isocyanate reaction involves the base-catalyzed addition of a thiol to an isocyanate, yielding a thiourethane linkage (*1*). It has recently been described as a click reaction due to its favorable reaction conditions (*2, 3*). A thiol will readily lose a proton in the presence of a base, yielding a thiolate anion. The thiolate anion attacks the positively charged carbon in the center of the isocyanate group. This yields a negatively charged secondary nitrogen, which abstracts a proton from a nearby thiol to stabilize the thiourethane linkage and propagate the reaction (Figure 1.1). This reaction has been extensively used for end-functionalization and surface synthesis (*4, 5*). It has only seen limited use in polymer synthesis due to the rapid reaction kinetics. With reaction times frequently measured in seconds it is difficult to handle and mold thiol-isocyanate solutions after catalyst has been added, unlike more common thiol-epoxy systems that typically react on hour scales (*3, 6, 7*). Thus, most thiol-isocyanate research has been in the context of ternary networks where thermosets are produced by joint thiol-ene/isocyanate or thiol-isocyanate-acrylate reactions. These networks have been shown to have increased network uniformity and T_g along with excellent mechanical performance due to the extensive hydrogen bonding present from the thiourethane linkage (*8-10*). Additionally, the large presence of sulfur and polar moieties in the thiourethane bond cause these materials to have high refractive indices compared to other thiol-click materials. As a result, there is industrial interest in the use of thiourethane-containing polymers as optical lenses (*11, 12*). To date there has been

little investigation into the dielectric behavior of these materials. It is likely that the high loading of sulfur and polar bonds in these polymers will result high dielectric constants in comparison to other thiol-click materials, as they have increased the refractive index. However, to fully access the many benefits of thiourethane polymers a substantial effort must be made to develop photo-latent bases which are dark-stable but capable of rapidly curing the resin upon exposure to ultraviolet or visible light. The inability to photo-polymerize polythiourethanes is one of the primary reasons that other thiol-click polymers such as thiol-enes have been more often studied in the open literature.

While this work focuses primarily on the reactions of thiols with isocyanate groups, thiols will readily react with a variety of other functional groups (*3, 13*). The thiol-ene and thiol-epoxy reaction are of particular interest, as they are the most widely utilized thiol-click reactions for polymer synthesis. The thiol-ene reaction is a radical-mediated reaction where a radical initiator abstracts a proton radical from the thiol. The resultant thiyl radical will attack unsaturated carbon-carbon pi bonds such as those in vinyl or acrylate functionalities. Polymers produced through the thiol-ene reaction are characterized by high network uniformity and low glass transition temperature due to the flexible thioether linkage. The thiol-epoxy reaction proceeds by an anionic mechanism similar to that of the thiol-isocyanate reaction. Thiol-epoxy polymers exhibit high uniformity similar to that of thiol-ene materials, but tend to exhibit slightly higher glass transition temperatures and hydrogen bonding due to the formation of hydroxyl moieties during the epoxide ring-opening reaction. However, the thiol-epoxy reaction proceeds at rates several orders of magnitude slower than thiol-ene and thiol-isocyanate coupling (*14*).

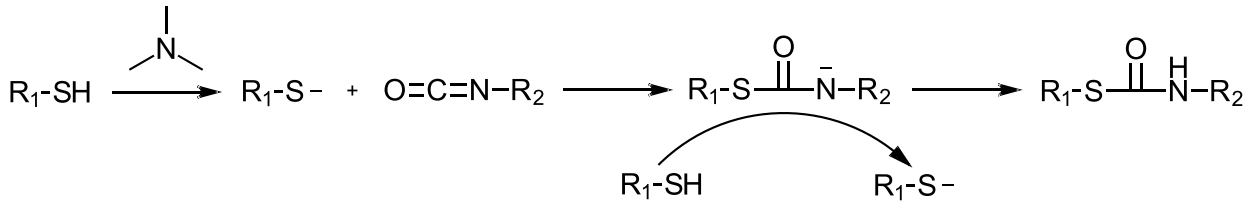

Figure 1.1. Thiol-isocyanate reaction mechanism; proton abstraction from the thiol by a tertiary amine initiates a nucleophilic addition to an isocyanate, forming the thiourethane bond and propagating the reaction further

1.3 Photo-Latent Bases

Photo-latent bases are organic molecules which break down into one or more basic components upon irradiation with light. While photo-radical initiators are well studied and available in many forms, photo-bases are much fewer in number and have only recently seen significant development. A number of photo-base classes have been identified; such as carbamates, amidinines, amineimides, and quaternary ammonium salts (*15-19*). Photo-labile carbamates are the most common photo-base initiator, devolving into primary or secondary amines either when heated or exposed to ultraviolet light. These have been used to cure a variety of polymer systems and have been adjusted to absorb UV radiation wavelengths as long as 400 nm (*20*). However, carbamates are not suitable for the curing of thiol-isocyanate systems, as the generated primary or secondary amine will react with the isocyanate to form a urea instead of catalyze the reaction. Photolatent amidinines are much fewer in number, but release strong bases such as diazabicyclononane. Efforts have been underway to increase the UV absorption peak of these photobases, with some products capable of absorbing at 365 nm wavelengths. These products have been able to cure thiol-epoxy systems to near-total conversion in under 10 seconds. However, the photolatent chemicals still have a relatively high pKa. This makes them unsuitable for reactions that are highly sensitive to basicity or applications requiring long shelf life (*21*).

Amineimide photobases have been described that decompose upon thermal or UV irradiation into a non-reactive primary amine and an undefined tertiary or aromatic amine. This class of photobase has been shown to absorb UV up to 365 nm and cure thiol-epoxy systems (*16*). The amine released by amineimides are able to catalyze the thiol-isocyanate system, albeit at relatively slow rates. In order to cure thiol-isocyanate polymers at rates comparable to thiol-ene materials a more potent base must be produced.

Quaternary ammonium salts are compounds that have been shown to release tertiary amines upon UV irradiation. They are a three component system consisting of a chromophore, a counter-anion capable of oxidation, and a tertiary amine. The chromophore determines the irradiation wavelength necessary to release the tertiary amine. Thus, aromatic systems are typically used with most absorbing in the sub-365 nm range as these are commonly available (*22-24*). Chromophores with reactivity near 400 nm are rare and include derivatives of thioxanthone, pyrene, and coumarin. These must be synthesized into the correct precursor before being able to form a quaternary ammonium salt (*25*, *26*).

The counter-anion must allow for single electron transfer to the chromophore, resulting in C-N bond cleavage to produce a tertiary amine and inert byproducts. The selection of the anion has a drastic effect on the organic solubility, solution stability, and reactivity of the ammonium salt. The most commonly implemented anion is tetraphenylborate. However others have studied other borate derivatives, dithiocarbamates, thiocyanates, and selenocyanate as possible replacements to improve the typically poor organic solubility of these materials while retaining dark stability and reactivity (*22, 24, 27-33*).

A tertiary amine must be used to form a quaternary ammonium salt. The choice is typically determined by the desired basicity of the released amine, although it has been shown that the amine structure can affect the reactivity of the photo-latent base (*22*). The most common amines are simple tertiary systems such as triethylamine. Others have implemented more effective catalysts such as dimethylaminopyridine, diazabicyclooctane, and diazabicycloundecene (*32*, *34*). Due to the non-nucleophilic nature of tertiary amines, they are an excellent choice for the catalysis of thiol-isocyanate systems. In fact, it has recently been demonstrated that quaternary ammonium salts releasing these catalysts can serve as effective initiators for the rapid polymerization of thiol-isocyanate systems, albeit at short-wavelength UV frequencies (*35*). Further development of the chromophore, counter-anion, and tertiary amines used in these photo-catalysts is crucial to enable rapid photo-curing of thiourethanes with commonly used light sources suitable for the applications discussed in this work.

1.4 Additive Manufacturing

Additive manufacturing is the act of synthesizing three-dimensional objects through successively forming layers of material from a computer model. It enables rapid prototyping and design optimizations that are unable to be produced through conventional manufacturing techniques (*36-38*). Additive manufacturing comes in many forms depending on the desired printing speed, resolution, material used, and quality of the final part. Solutions for polymer printing typically fall into one of three catetories; filament, powder-bed, and photopolymer.

Fused filament fabrication (FFF) is the most common 3D printing method implemented today. In FFF a plastic filament is fed into a heated print head, which melts the polymer and allows it to be extruded through the end of the print head. The extruded filament is laid down onto a print bed in

successive two-dimensional layers until the part is completed. The relative ease of processing materials in ways related to traditional thermoplastic processing in FFF has resulted in a myriad of available printing systems and filaments available for purchase. It is typically the least expensive and easiest to implement mode of additive manufacturing. It has the advantage of being scalable to large build volumes. Despite the ease of implementing FFF printing, it has had difficulty finding a significant place in industry thus far in large part due to the poor mechanical performance and poor surface finish of the final printed parts. Parts produced via FFF often have strength approaching that of the bulk material when stressed in-line with the filament orientation. However, when stressed perpendicular to the filament deposition axis or in the vertical direction of the build, parts fail prematurely due to poor adhesion between the printed layers. This is a result of inadequate mixing of deposited material onto the underlying part to fully "weld" and produce a full-strength bond (*36*). As such, FFF has remained in use primarily for early stage prototyping and hobbies. This will likely remain the reality until new chemistries or processes are developed which enable FFF-produced parts to exhibit mechanical uniformity on-par with those parts produced via traditional manufacturing techniques.

Powder bed systems utilize a bed of polymer powder that is either sintered with a high-power laser and/or bound together with a binding agent. These systems have the advantage of higher surface finish and a decreased layering effect in comparison to FFF-made parts. In addition, the printed part is suspended in the powder feedstock. This eliminates the need for support structures. These systems commonly print with polyamide feedstock designed to have a decreased melting temperature, such as copolymers of PA-11 or PA-12. While mechanical performance can be good, the performance of the printed materials tend to be substantially lower

than injection-molded counterparts. In addition, the cleanup requirements following printing are laborious and dirty. These systems require large upfront capital outlays, often costing upwards of $100,000, with powders sometimes approaching $1000 per kilogram, limiting their use in the consumer and research communities (*39, 40*).

Photopolymer printing techniques utilize a liquid resin which polymerizes upon exposure to UV light. There are two major photopolymer printing techniques; stereolithography (SLA) and polymer jetting. SLA is the oldest 3D printing method. It has the advantage of fabricating parts with improved mechanical isotropy and high surface finish. In SLA, a moveable build platform is placed in a bath of photo-curable pre-polymer resin. The platform is positioned so that a thin layer of resin is over the build platform. A laser or projector then selectively cures the thin layer into the desired shape. The build platform is then moved to flow another thin layer of resin on top of the initial cured layer. This process is repeated until the final three-dimensional part is formed. This can take place with the light source shining from either above or below the resin vat through a transparent window, depending on the system design. Following printing, the part is then removed from the resin bath, cleaned, and post-cured (*41*).

Polymer jetting, or inkjet printing, uses a piezoelectric print head much like in a common printer to selectively deposit resin on the build plate. A trailing UV lamp cures the resin as it is deposited. This technique has many advantages such as minimal resin waste, multi-material capability including removable support material, very high part fidelity, and reduced post-curing requirements. However, inkjet printers are more complex than SLA printing machines and are prone to failure unless operation is kept within strict guidelines. In addition, these machines have

limited resin compatibility due to the low viscosity needed to jet from the print head correctly (*42*).

The entire fabrication process may take between tens of minutes to hours depending on the part size, complexity, and photopolymer resin used. The vast majority of photopolymer resins rely on acrylate functionality. The wide commercial and synthetic availability of acrylate monomers allows for straightforward control of T_g, crosslink density, resin viscosity, and other properties (*43, 44*). This flexibility in combination with its rapid reaction kinetics has made it attractive for use in photopolymer resins. However, there are a number of difficulties present that limit its usefulness in additive manufacturing. Acrylic polymers tend to have insufficient mechanical performance for many applications, which often results in brittle parts that are unsuitable for structural components. Acrylates also undergo large volumetric shrinkage when curing (*45*). This results in cure stresses when combined with the early gelation at low conversion that is inherited from the chain-growth polymerization mechanism (*46*). The large cure stresses present in fully cured polyacrylates can cause large undesired deformations in the final printed part. There is a large amount of interest in polymer systems which undergo rapid curing but have reduced cure stresses and improved mechanics for use in photopolymer printing.

To combat the shrinkage and warping of pure acrylate materials, hybrid systems were developed which contain interpenetrating networks of acrylates and more slowly curing epoxide materials. This combines the rapid rate of acrylate polymerization with the low cure stress of epoxides. However, the epoxide functionality requires an extended thermal post-cure to obtain the final part properties. In addition, neither acrylates nor epoxides have high toughness. The resultant materials are typically still brittle (*47, 48*). Minor improvements have been made by

functionalizing urethane or cyanate ester oligomers with acrylate moieties for improved toughness or thermal resistance (*49*-*52*). However, these materials still perform poorly when compared to bulk engineering polymers. Some improvements have been made in both the speed and part toughness by using interpenetrating networks of acrylates and urethanes. However, these too require very long (~10 h) thermal post-cures before becoming mechanically stable (*53*). The inability to produce rapidly curing, highly tough photopolymers for 3D printing combined with the mechanical anisotropy found in most 3D printed parts has limited the proliferation of additive manufacturing systems in industries where toughness and speed are critical.

The approach presented in this work seeks to utilize the thiol-isocyanate click reaction to rapidly produce tough, thermally resilient 3D printed parts. Toughness is the ability of a material to dissipate mechanical energy exerted upon it before failure. There are two common metrics for toughness. Tensile toughness, measured in Joules per cubic meter, is the integrated area of the stress-strain curve in a tensile test prior to fracture (*54*). Fracture or impact toughness is determined through the Izod or Charpy test standards and is measured in Joules per square meter (*55*). Toughness in polymers is a complex phenomenon, affected by a multitude of material properties such as glass transition temperature (T_g), degree of hydrogen bonding, percent crystallinity, and crystal yield stress.(*56*) It is generally accepted that semi-crystalline polymers are capable of higher toughness than completely amorphous polymers due to interactions between the amorphous and crystalline fractions delaying or suppressing crack formation within the material (*57*).

Thermal resilience is typically quantified in the form of the heat deflection temperature as determined by the ASTM D648 or ISO 75 testing standards (*58*). While not a direct

measurement of a a thermomechanical phenomenon, heat deflection testing provides a practical means of determining the temperature at which a material begins to soften. This is typically used to establish the maximum thermal operating temperature of a given material. In polymers, the heat deflection behavior is closely related to the glass transition or crystal melt temperature. Photopolymers used in 3D printing systems are typically amorphous, therefore their heat deflection temperatures usually occur near their respective glass transition temperatures (*59-61*). These values are below the heat deflection temperatures of engineering thermoplastics such as polypropylene or polyamide, as their heat deflection temperatures are dictated by their crystal melts, which occur at higher temperatures (*62*).

The thiol-isocyanate click reaction proceeds quickly in the presence of a base such as tertiary amines generated by photo-latent bases. These materials have extensive hydrogen bonding and are capable of crystallization necessary to vastly improve the toughness and heat deflection temperature of 3D printed parts. This enables the rapid formation of tough thiourethane polymers from a low viscosity monomer solution. This is unique because it utilizes a fast anionic step-growth polymerization mechanism, which combines the rapid curing characteristics of radical initiated systems with the low cure stress and toughness of cationic systems. 3D printing techniques such as stereolithography or polymer jetting allow parts to be produced with internal geometries that vastly reduce the amount of resin used. This reduces both the part cost and mass. The ability to develop tough, thermally resilient parts stands to push additive manufacturing from light use to displacing conventional manufacturing techniques.

1.5 Softening Bioelectronics

Bioelectronics are devices designed to exchange information between the human body and an external device in order to restore or supplement function to areas such as the nervous system (*63-66*). The ability of bioelectronic devices to stimulate and record signals from neural tissue has resulted in large advances in recovering from debilitating neurological conditions and injuries (*67-69*). Solutions such as pacemakers and cochlear implants have demonstrated the feasibility of applying bioelectronics on large scales. Other more advanced applications are still in development such as enabling lifelike artificial limbs, stimulating neural growth, and interfacing with the human brain. The ability to record and stimulate neural signals in real-time stands to drastically alter the way medicine is conducted by moving from reactive treatment of illness to proactive treatment. The initial iterations of these devices have been used successfully in acute conditions. However, more widespread use of these devices is limited due to poor chronic neural recording (*70*). Specific solutions to limit chronic failure in neural interfaces are difficult to implement even as the underlying mechanisms continue to be better understood. The investigation done thus far suggests that a combination of the neuroinflammatory response, device failure, and chronic damage to surrounding tissue contribute to the various failure modes of neural interfaces over longer spans of time (*71-79*). There is substantial evidence that these sources of failure are rooted in the substrate used during fabrication.

Bioelectronic devices have historically been fabricated on materials such as tungsten and silicon due to their extensive use in semiconductor fabrication. Examples of these designs include the Michigan and Utah microelectrode arrays. Tungsten and silicon have very high elastic moduli of over 3 GPa. Brain tissue, in comparison, has a modulus of approximately 5 kPa. This represents a difference in modulus of six orders of magnitude. An ever-increasing body of research is

beginning to demonstrate that this mechanical mismatch is closely linked to the device failure modes discussed previously. Marginally softer materials such as polyimide have been used to fabricate electrode arrays, but with moduli still in the GPa range they offer little improvement over tungsten or silicon substrates. Others have fabricated microelectronics on polydimethylsiloxane, which more closely matches brain tissue with a modulus of 0.1 to 1 MPa (*80*). Unfortunately, the permanent soft behavior makes it particularly difficult for devices to be implanted into the body. Devices frequently break during insertion or highly invasive procedures are necessary to effectively implant the device. Therefore, an adaptive substrate which is rigid enough to be easily inserted into the body but softens in vivo following surgery is the optimal solution.

Initial efforts to produce mechanically adaptive substrates made use of nanocomposites which swelled in the presence of water to soften by up to three orders of magnitude. These substrates were shown to substantially reduce the initial swelling response in the human brain following implantation and may produced less micromotion-induced stresses in the brain (*81, 82*). Fabricating complex microelectronics proved to be more difficult; substrates had low device yield and the large degree of water uptake caused severe delamination of the electronics and resulted in device failure (*83*). Newer iterations of these nanocomposites have improved their processing, but do not yet reach the complexity of tungsten or silicon-based devices. An alternative approach has been the use of shape memory polymers to induce softening. Shape memory polymers are materials which undergo a glass transition resulting in a large decrease in modulus. These were first demonstrated in acrylic networks which softened upon exposure to physiological temperatures and moisture. However, the acrylic substrates had large cure stresses

which made it difficult to fabricate electronics (*84*). This was largely remedied through the use of thiol-ene/acrylate shape memory polymers. These substrates were shown to soften by approximately two orders of magnitude following insertion into the body. The low cure stress of these substrates allowed microelectronics to be fabricated using established photolithographic techniques. These substrates have demonstrated near-chronic stability and decreased physiological response to implantation. However, they soften to 20-100 MPa and are prone to mechanical failure (*80, 85, 86*). Alternative chemistries may improve the softening and mechanical performance of shape memory polymer substrates and improve chronic viability. Thiourethane polymers have a number of characteristics that may improve the effectiveness of softening bioelectronics. As shown in previous works, the thiourethane linkage is more rotationally rigid than the thioether bond formed during the thiol-ene reaction. This increases the glass transition temperature compared to similarly structured thiol-ene networks (*8, 10*). Therefore, it is likely that thiourethane networks may be used to synthesize low-crosslink density networks capable of softening more than previous thiol-ene substrates. The high loading of thiourethane bonds in these materials also imparts a large degree of hydrogen bonding in the material. This hydrogen bonding between the polymer chains may improve the toughness of the substrate compared to the previously used thiol-ene materials which have few macromolecular interactions, as large deformations will require more mechanical energy. This may also result in improved plasticization of the substrate *in vivo* due to increased water uptake. Thus, thiourethane substrates may serve as a platform to reduce device failure due to mechanical failure or neuroinflammatory response.

1.6 Dielectric Elastomer Artificial Muscles

Artificial muscles are synthetic materials designed to mimic the actuation of human muscle. Human skeletal muscle is noted for its impressive actuation properties, with strains greater than 40%, pressures over 350 kPa, and a specific energy density of 0.07 J g^{-1} (*87-89*). Currently, the majority of robotics applications make use of electromagnetic (EM) motors for actuation. These have drawbacks such as high power consumption as size decreases, large gearing requirements, noise and heat generation, and the inability to provide "give" like natural muscle. This leads to bulky actuation systems requiring large power sources, reducing the effective energy density (*90*). Dielectric actuators (DEAs) are an artificial muscle solution that has the potential to solve many of these problems.

Dielectric actuators operate as flexible capacitors, decreasing in thickness and increasing in area in the presence of an applied field. These devices are electrostatic, only consuming power when actuating. They produce strains over 200%, pressures over 7 MPa, and have very high work densities and efficiencies (*87, 88, 90-94*). Most of the materials used for DEAs are commercially available, such as 3M VHB acrylic elastomers, silicones, and polyurethanes. Each of these materials have their own drawbacks such as low dielectric constant, low stresses, or low strains (*87, 95*). In order to develop high performance DEAs it is necessary to investigate polymer systems that may be tuned to minimize their weaknesses and maximize their strengths for the desired application. This is most often done by attempting to increase the dielectric constant of the actuator material. Efforts to improve the dielectric constant of DEA materials tends to fall under two categories; grafting molecules with strong dipole moments onto the polymer backbone, or adding high-k filler materials to the polymer matrix.

Grafting is typically accomplished by functionalizing existing DEA materials such as silicones and attaching polar side chains to the backbone. This approach has the advantage of high homogeneity in the polymer matrix, which reduces the risk of causing premature dielectric breakdown. However, the polar groups used typically have detrimental effects on the mechanical performance of the material. Typical results show that meaningful increases in the dielectric constant are only obtained after the mechanical performance has decayed too much to be useful (*87, 96, 97*).

The most commonly used approach for improving the dielectric constant is by adding high-k filler material to the polymer matrix. This can take the form of non-conductive particles such as TiO_2 or conductive media such as carbon powder or metallic particles. This method typically yields much larger increases in effective dielectric constant due to the very high dielectric constant of the particles used. The primary drawback of filler materials is that it usually results in decreased dielectric strength, decreasing the overall strain performance compared to non-filled materials (*98-101*). This has been somewhat mitigated through the use of functionalized nanoparticles to improve homogeneity, but the rigid filler still tends to degrade the mechanical performance of the material (*102*). As both common methods for improving the dielectric behavior of these materials tend to have poor results, further materials development is needed to improve the usefulness of DEA polymers.

Thiourethane elastomers may be uniquely poised to act as high-performance DEA materials. The wide availability of both thiol and isocyanate monomers allows the mechanical properties of the resultant networks to be finely tuned to the appropriate modulus for DEA operation. The polar moieties added to the polymer chain by the thiourethane linkage in addition to the high molar

refractivity of sulfur may result in an improved dielectric constant over the materials currently used in DEAs (*103*). This may prove to be a superior method of increasing the dielectric performance of DEA materials. Since the dielectric behavior will be an intrinsic property of the material the dielectric strength may remain high compared to grafted or filled polymers with lower homogeneity. Improvements in the dielectric constant would reduce the field requirements of DEAs, aiding their safety and design requirements.

1.7 Objectives and Overview of Results

The goal of this research is to design, synthesize, and characterize photo-polymerized thiourethane polymers to solve fundamental materials challenges in photopolymer 3D printing, bioelectronics substrates, and dielectric elastomer actuator films. Advances in photo-cured thiourethane polymers will enable stronger 3D printed parts, improve the softening ability of bioelectronics substrates, and enhance the performance of dielectric elastomer artificial muscles. Thus, this research has the following aims:

(1) **Enable** photo-cured polythiourethanes by synthesizing photo-latent bases which are dark-stable and capable of curing bulk thiol-isocyanate resins in under one minute upon UV irradiation, comparable to thiol-ene or acrylate radical chemistries.

(2) **Toughen** 3D printed parts by developing a thiourethane photo-polymer resin which has an integrated stress-strain curve of at least 50 MJ m^{-3} when 3D printed; five times that of typical "tough" photopolymer resins.

(3) **Interface** with the nervous system by creating polythiourethane substrates which soften to less than 10 MPa *in vivo* and demonstrate that neural interface devices can be fabricated on the substrate and successfully record neural signals when implanted.

(4) **Decrease** the field requirements of dielectric actuators by synthesizing polythiourethane elastomers with dielectric constants above 8, twice that of the state of the art materials currently in use

Chapter 3 illustrates thiol-isocyanate elastomers cured in reaction times comparable to thiol-ene systems using novel photo-latent bases. These networks are highly tough due to their extensive hydrogen bonding and semi-crystalline nature. Chapter 4 describes the 3D printing of

thiourethane resins using photo-latent tertiary amines. These resins are compatible with the light sources in commercial printing systems and have cure rates comparable to commercial resins, but are many times tougher. This tough polymer system is extended to fused filament fabrication printing in Chapter 5. Chapter 6 demonstrates that thiourethane thermosets may be used to synthesize robust substrates for bioelectronics which soften by three orders of magnitude for improved physiological response and recording. Chapter 7 suggests that photopolymerized thiourethane elastomers may improve the performance of dielectric actuators due to having easily tuned thermomechanical properties and dielectric constants larger than the most effective polymers used today.

CHAPTER 2

MATERIALS AND METHODS

2.1 Materials

4-(bromomethyl)benzophenone, 2-iodobenzoic acid, 4-methylbezenethiol, copper iodide, N-bromosuccinimide (NBS), 1,5-diazabicyclo[4.3.0]non-5-ene (DBN), sodium tetraphenylborate, pentaerythritol tetrakis(3-mercaptopropionate) (PETMP), trimethylolpropane tris(3-mercaptopropionate) (TMTMP), hexanedithiol, and isophorone diisocyanate were purchased from Sigma Aldrich. 2,2'-(ethylenedioxy)diethanethiol (EDDT), hexamethylene diisocyanate, trimethylhexamethylene diisocyanate were purchased from TCI America (Portland, OR). Anhydrous dichloromethane, hydrochloric acid, sulfuric acid, potassium hydroxide, and anhydrous magnesium sulfate were purchased from Fischer Scientific. Tris(6-isocyanatohexyl)isocyanurate (HDI-T, or Desmodur N3300A) was kindly donated by Covestro (Leverkusen, Germany). All chemicals were used without further purification.

2.2 Nuclear Magnetic Resonance Spectroscopy

Nuclear magnetic resonance spectroscopy (NMR) is an analytical technique which employs the magnetic properties of atomic nuclei to provide information on their bonding environment and chemical state. When placed in a magnetic field, atomic nuclei will absorb electromagnetic radiation at a characteristic frequency. The nuclear magnetic resonance response, known as the free induction delay, is recorded by the instrument. A Fourier transform is used to extract the frequency-domain spectrum from the raw data, which provides the chemical shifts used for analysis. The chemical shift will vary depending on the electronic environment of the atomic

nucleus. For well-characterized nuclei such as H_1, the chemical shifts for most bonding environments are known and are predictable. The predictability of H_1 chemical shifts in combination with the speed of data acquisition and ubiquity of hydrogen in organic molecules makes H_1 NMR an invaluable tool for determining the structure of small molecules and polymers.

2.3 Gel Permeation Chromatography

Gel permeation chromatography (GPC) is an analytical technique used to determine the molecular weight distribution of a polymer. In GPC, a polymer dissolved in an eluent (solvent) is passed through a gel with a precisely controlled pore size. If the radius of gyration of the dissolved polymer is sufficiently small, it will enter the pores of the gel and take longer to pass through the column. For linear polymers, this is directly related to the molecular weight. Thus, the elution time is inversely related to the molecular weight of the polymer. A detector at the base of the column is used to determine how much dissolved polymer passes through the column as a function of time. When compared to a standard, typically of highly uniform dispersity polystyrene, the molecular weight and polydispersity index of the sample can be determined to a high degree of accuracy.

2.4 Thermogravimetric Analysis

Thermogravimetric analysis (TGA) is a thermal analysis technique that measures the mass of a sample as it is heated. The sample is placed in an empty crucible whose mass has been previously recorded. The TGA then takes the mass of the sample and initiates a heating ramp from a set starting temperature to a target end temperature. As the sample heats, it may undergo a

number of chemical reactions depending on its composition. These reactions typically have an associated change in mass. In this work the mass changes are negative, reflecting the degradation of the polymer as the temperature exceeds that which the bonds can sustain. Thus, TGA is used to define the degradation temperature T_d of the polymer systems discussed.

2.5 Differential Scanning Calorimetry

Differential Scanning Calorimetry (DSC) measures the difference in the amount of heat necessary to heat a sample with regards to a reference as a function of temperature. This information may be used to determine changes in enthalpy or the specific heat capacity of the sample as a function of temperature. This allows DSC to identify first and second order phase transitions. In the context of this work, it may be used to determine glass transition and crystalline melt temperature (T_m). The T_g is indicated by a step change in the heat flow into the sample. Melting point is indicated by an endotherm. Further calculation and analysis can show the hysteresis between the melt and recrystallization as well as the percent crystallinity. In this work, samples were subjected to a heat-cool-heat-cool-heat cycle to first erase thermal history by heating above T_g but below T_d. The sample is then cooled to the desired start temperature of the experiment and heated through the desired temperature range twice to analyze and confirm the thermal behavior of the material.

2.6 Dynamic Mechanical Analysis

Dynamic mechanical analysis (DMA) is a thermomechanical characterization technique that shows the viscoelastic behavior of materials as a function of temperature and frequency of deformation. This test can be conducted in a wide variety of conditions such as tension, shear,

compression, and flexion. During a test the sample is held in a clamping assembly and subjected to a small sinusoidal deformation of a set frequency and amplitude. Assuming that the deformation of within the elastic regime of the material, the stress and strain waves may be used to calculate the complex modulus (E*) and phase angle (δ). The storage modulus (E') and loss modulus (E'') may be determined by the relationship between E* and δ as shown in equations 1 and 2.

$$E^* = E' + iE'' \tag{1}$$

$$\tan(\delta) = \frac{E''}{E'} \tag{2}$$

DMA is unique in that it can provide information about the thermal, mechanical, and time-dependent behavior of a material in a single test. The typical test used in this work shows how a sample changes in stiffness as a function of temperature through the measurement of E' and its damping capability with regards to temperature by measuring tan(δ). The glass transition temperature may be found at the peak of tan(δ). This behavior will change as a function of the oscillation frequency and is easily determined using multi-frequency testing protocols that modern instruments are capable of performing.

2.7 Rheology

Rheology (rheometry) is the study of the flow properties of a liquid or semi-solid. Rheology is an important characterization tool for polymers, for characterizing the behavior of both polymer resins and melts depending on the target application. In a typical testing scenario, a thin film of liquid is placed between a static plate and another plate rotating at a known rate. The rotation speed determines the shear rate applied to the material, and the torque needed to maintain the

rotation may be used to calculate the viscosity of the liquid. Viscosity is often dependent on temperature, and may be dependent on the shear rate. Viscosity control is crucial for effective processing in extrusion, stereolithography, or polymer jetting applications.

2.8 Fourier Transform Infrared Spectroscopy

Fourier transform infrared spectroscopy (FTIR) is a spectroscopic technique which is capable of quickly and reliably determining the functional groups present in a material. It relies on the fact that infrared radiation will excite vibrational modes of atomic pairs that cause a change in the molecular dipole moment. The excitation frequency is dependent on the atoms in the pair, their bonds with each other, and their neighboring bonds. As a result, FTIR is capable of discerning between specific functional groups present in small molecules or polymers. The simple sample preparation and rapidity of measurement has made FTIR an invaluable tool for chemists to confirm structures of small molecules or track polymerizations. Real-time infrared spectroscopy techniques allow reactions between small molecules or polymerizations to be tracked as the reaction progresses, giving chemists the ability to reaction kinetics and rate constants.

2.9 Uniaxial Tensile Testing

Tensile testing is a method of measuring the stress-strain response of a material from the linearly elastic region until failure at a set temperature. It is considered a quasi-static test; where deformation rates are low enough to consider the results equivalent to the static performance of the material at a given strain. Polymers exhibit wide ranges of properties in tension depending on their T_g and crystalline fraction. Below T_g, most polymer networks exhibit high modulus, brittle behavior. As the temperature passes through and beyond the T_g, the modulus decreases and

failure strain increases until the material exhibits elastomeric behavior. Semi-crystalline systems exhibit a more complex response, showing larger stresses and lower strains than amorphous polymers beyond the T_g until reaching the crystal melt temperature. Uniaxial tensile testing may also be used to determine toughness by integrating the stress-strain curve, giving the amount of energy per unit volume required to fracture the sample. Semi-crystalline thermoplastics tend to have high toughness due to their ability to withstand high stresses at high elongations.

2.10 Heat Deflection Testing

Heat deflection testing is used to provide a practical measurement of the maximum thermal operating temperature of a material. Two commonly employed testing standards are ASTM D648 and ISO 75. Both standards employ a rectangular test specimen placed in a three-point bending configuration submerged in a temperature controlled circulating oil bath. A static load is placed on the sample to produce a bending stress of 0.455 or 1.82 MPa, and the temperature is increased at 2 °C min^{-1} until the sample deflects to a strain of 0.002 (*58*). In polymers, this point typically correlates with either the glass transition temperature or crystal melt.

2.11 Stereolithography

Stereolithography is the process of using an ultraviolet laser or projector to selectively cure material in a vat of photopolymer resin. Most SLA machines in use today operate by shining a UV laser or projector up through the bottom of a transparent vat containing the photopolymer. The bottom of the vat is coated with an oxygen-permeable material such as polydimethylsiloxane to inhibit the polymerization at its surface and prevent sticking to the bottom of the vat. A moveable build plate is lowered into the vat, upon which successive layers of material are cured

by lifting the plate from the resin bath in increments ranging from 10 to 100 μm while curing (*36, 48*). More recent developments have eliminated the layer approach by utilizing highly oxygen permeable membranes as the vat window to allow for continuous curing while the plate is lifted from the solution. This has been shown to drastically reduce print times and yield mechanically isotropic parts with excellent surface finish (*53*).

2.12 Polymer Jetting

Polymer jetting is a 3D printing technique in which a photopolymer resin is selectively deposited on a build plate by a piezoelectrically driven inkjet head. On each pass, a trailing ultraviolet light cures the deposited resin. Drop sizes are on the order of 3 picoliters, resulting in an effective voxel resolution of as low as 10 μm × 10 μm × 10 μm. Additional print heads can utilize different resins to allow multi-material printing, which is unique among photopolymer printing techniques. The primary limitation of these systems is the strict viscosity requirements for the printing resin, which needs to be sufficiently low to successfully pass through the inkjet head. Heated print heads can help reduce viscosity as the resin enters the head, but excessive heating runs the risk of causing premature polymerization of the resin prior to deposition (*39*).

2.13 Fused Filament Fabrication

Fused filament fabrication is a 3D printing technique which feeds a thermoplastic filament into a heated extrusion head. The extrusion head is fixed to a motorized system which controls the position of the extrusion head in the x, y, and z axes. Parts are printed in layers between 10 μm and 500 μm thick, depending on the surface finish and print speed that is desired (*36*). FFF is compatible with a wide range of thermoplastic feedstocks such as polylactic acid, acrylonitrile-

butadiene-styrene, high impact polystyrene, thermoplastic polyurethane elastomers, and nylon copolymers. This allows parts to be printed with a wide variety of mechanical and thermal behaviors. Due to its relative simplicity, low cost, and safe operation, filament based systems are the most widely sold and utilized 3D printers available on the market today despite having relatively poor surface finish and anisotropic mechanical properties (*40*).

CHAPTER 3

QUATERNARY AMMONIUM SALTS FOR RAPID LONG-WAVELENGTH PHOTOPOLYMERIZATION OF TOUGH POLYTHIOURETHANES

3.1 Introduction

One of the premier advantages of thiol-ene polymers is the ability to rapidly photo-cure thermoset materials to high degrees of completion under mild conditions. The ease of synthesizing thiol-ene polymers and adjusting their properties has resulted in increasingly more use as smart materials. However, their utility is limited due to their characteristically low glass transition temperatures and poor mechanical strength. Another less studied thiol-click reaction is the coupling of thiols and isocyanates. This reaction occurs rapidly in the presence of a tertiary amine catalyst. The resultant materials are characterized by high glass transition temperatures and toughness due to extensive hydrogen bonding in the resultant thiourethane linkage. The bulk polymerizations of polythiourethane thermosets have not been studied in detail due to the difficulty in controlling the reaction. This will remain the case until efficient photo-catalysts are developed which release highly basic tertiary amines under irradiation by common ultraviolet curing sources.

This work describes the synthesis of quaternary ammonium salts which release the strong base 1,5-diazabicyclo[4.3.0]non-5-ene (pKa ~13.5) upon irradiation with light between 300 nm and 400 nm. The excitation wavelength may be adjusted by altering the structure of the chromophore. It is demonstrated that the quaternary ammonium salts degrade and release DBN quickly upon irradiation, resulting in a rapid change in pH. This is sufficient to catalyze the near quantitative reaction of polythiourethanes in as little as a few seconds of irradiation. Bulk

polymerization of polythiourethane thermosets is achieved quickly under mild reaction conditions.

3.2 Experimental Procedure

3.2.1 Nuclear Magnetic Resonance Spectroscopy

1D proton NMR was performed on a Bruker AVANCE III 500. Approximately 15 mg of samples were dissolved in 0.5 mL of deuterated chloroform or dimethyl sulfoxide. Samples underwent 16 scans at 500 MHz. Processing and peak integrations were performed using the Bruker TopSpin software.

3.2.2 Real-time Fourier transform infrared spectroscopy

Real-time FTIR was performed on a Shimadzu IRAffinity-1 with an attenuated total reflection (ATR) attachment. Stoichiometric mixtures of 2,2'-(ethylenedioxy)diethanethiol (EDDT) and hexamethylene diisocyanate (HDI) were mixed with 0.1 wt% of photo-catalyst. The solutions were dropped onto the liquid-ATR cell and continuously scanned between 700 cm^{-1} and 4000 cm^{-1} with 0.5 cm^{-1} resolution with a sampling rate of 2.3 seconds per scan. Higher scanning rates were obtained by scanning the isocyanate peak only between 2000 cm^{-1} and 2500^{-1}. Samples were exposed to 365 nm irradiation using a handheld UV LED emitter. Irradiation remained on until completion of the test.

3.2.3 UV-visible spectroscopy

UV-visible absorption spectroscopy was performed on an Agilent Cary 5000 UV-Vis-NIR spectrophotometer. Solutions were mixed containing 0.5 wt% photo-catalyst in acetonitrile. The

solution was dispensed into 1 mL cuvettes which were then irradiated by 365 nm or 385 nm light for up to 10 minutes. Samples were either then scanned immediately between 200 nm and 450 nm or had 1 mM phenol red solution in acetonitrile added prior to scanning between 300 nm and 700 nm.

3.2.4 Dynamic mechanical analysis

A stoichiometric mixture of pentaerythritol tetrakis(3-mercaptopropionate) and isophorone diisocyanate was mixed with 0.1 wt% of QAS-BP and cured for 30 minutes under 365 nm irradiation in a UVP CL-1000L between glass slides separated by 500 μm spacers. This was followed by one hour of thermal post-curing at 150 °C in vacuum. Samples were cut into rectangular bars approximately 30 mm x 3 mm x 0.5 mm. Dynamic mechanical analysis was performed on a Mettler Toledo DMA/SDTA831e in tension from 0 °C to 200 °C at 2 °C min^{-1} with an oscillation at 1 Hz, 5 N force limit, 0.2 % strain limit, and 300% offset. Glass transition temperature was taken as the peak of tan δ.

3.3 Results

3.3.1 Synthesis of QAS-BP

4-(bromomethyl)benzophenone (2.0 g) was added to a dry nitrogen-purged round-bottom flask and dissolved in anhydrous dichloromethane (100 mL). 1,5-Diazabicyclo[4.3.0]non-5-ene (930 mg) was dissolved in anhydrous dichloromethane (10 mL) and added dropwise to the flask. A white precipitate formed almost immediately. The reaction was allowed to progress for two hours prior to extracting the product with water (200 mL). The water was removed via rotary

evaporation, and the remaining viscous liquid re-dissolved into methanol (200 mL). Sodium tetraphenylborate (2.04 g) was dissolved in methanol (50 mL) and added dropwise to the methanol solution while stirring. A thick white precipitate formed immediately. The solution was allowed to stir for one hour before separating the solid by vacuum filtration. The solid was dried under dessication and confirmed to be 5-(4'-(bromomethyl)benzophenone)-1,5-diazabicyclo[4.3.0]non-5-ene tetraphenylborate by H_1 NMR (3.5 g, 75% yield).

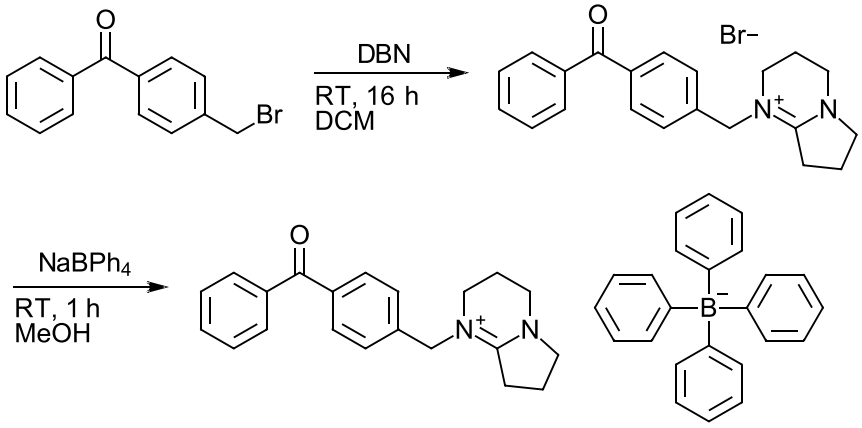

Figure 3.1. Synthetic schematic of QAS-BP; DBN performs a nucleophilic addition to the bromomethyl group on the benzophenone, yielding an ammonium bromide salt. The bromine anion is replaced with tetraphenylborate via a metathesis in methanol

3.3.2 Synthesis of QAS-MTX

2-iodobenzoic acid (3.5 g), 4-methylbenzenethiol (1.75 g), potassium hydroxide (3.96 g), and copper iodide (0.27 g) were dissolved with water (mL) in a round-bottom flask. The solution was refluxed for 12 hours, then acidified using 10% hydrochloric acid solution. A white precipitate formed upon acidification, which was filtered and confirmed to be 2-[(4-methylphenyl)thio]-benzoic acid via ^{1}H NMR (4.05 g, 84% yield).

2-[(4-methylphenyl)thio]-benzoic acid (4.05 g) was dissolved in concentrated sulfuric acid (20 mL) and heated to 110 °C for 4 hours while stirring. The solution was pipetted into water

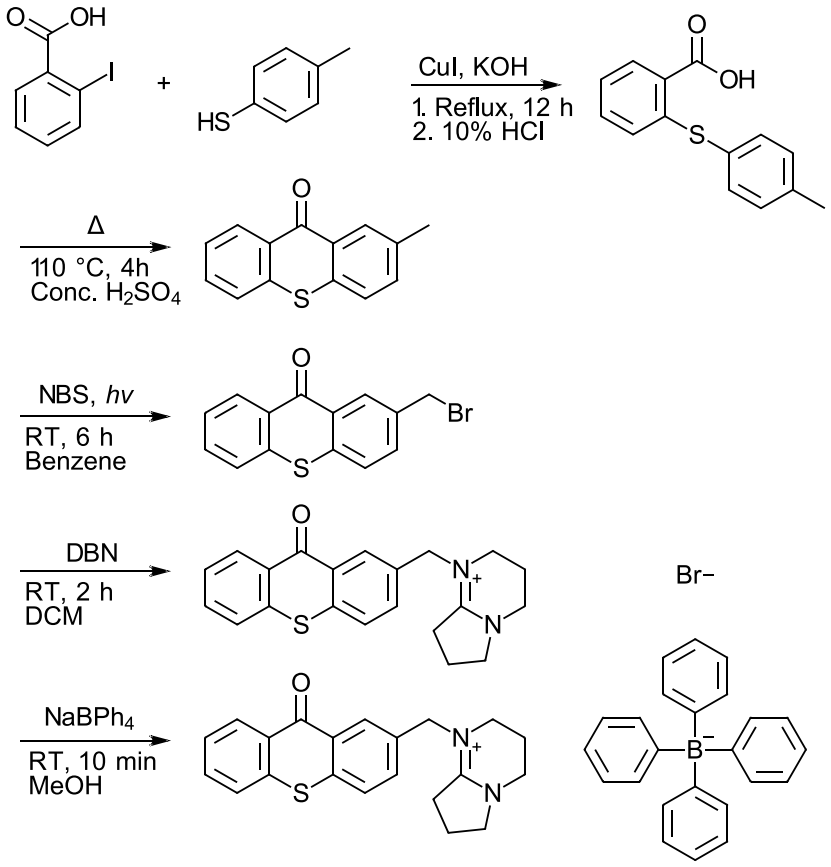

Figure 3.2. Synthetic schematic of QAS-MTX; 2-(methyl)thioxanthone is formed via the copper iodide catalyzed reaction between 2-iodobenzoic acid and 4-methylbenzenethiol followed by ring-closing in concentrated sulfuric acid. The methyl group is brominated using NBS, which is then displaced by DBN in a nucleophilic addition to form an ammonium bromide salt. The bromide anion is replaced by tetraphenylborate in a metathesis in methanol

(200 mL) in an ice bath while stirring. A yellow precipitate formed immediately, which was filtered and washed with 10% sodium bicarbonate solution (100 mL). The remaining product was confirmed to be 2-(methyl)thioxanthone via ^{1}H NMR (3.45 g, 92% yield).

2-(methyl)thioxanthone (1.00 g) was added to a dry round-bottom flask with N-bromosuccinimide (0.79 g) in benzene (10 mL). The solution stirred at room temperature under nitrogen and halogen illumination for 6 hours. The solution was washed with water (20 mL) to

remove succinimide byproduct, then the benzene was removed by rotary evaporation. The remaining solid was found to be 2-(bromomethyl)thioxanthone via ^{1}H NMR (1.15 g, 85% yield). 2-(bromomethyl)thioxanthone (2.00 g) was added to a dry nitrogen-purged round-bottom flask and dissolved in anhydrous dichloromethane (150 mL). 1,5-Diazabicyclo[4.3.0]non-5-ene (0.82 g) was dissolved in anhydrous dichloromethane (5 mL) and added dropwise to the flask while stirring. The reaction progressed for 2 hours before extracting the product with water (300 mL).

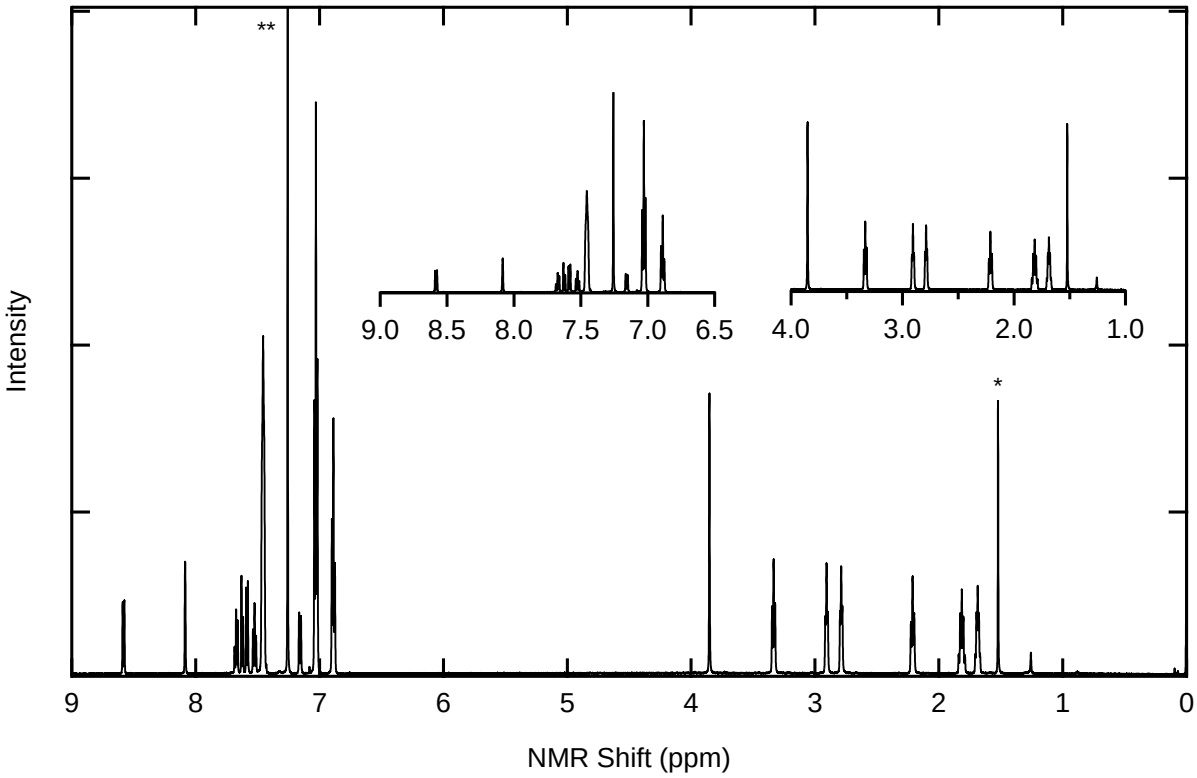

Figure 3.3. ^{1}H NMR of QAS-MTX. Shielded protons in the thioxanthone and tetraphenylborate are up-shifted to between 8.6 and 6.8 ppm. The methylene bridge protons between the thioxanthone and ammonium show near 3.9 ppm. The DBN protons are spread between 3.4 ppm and 1.7 ppm.

The water was removed by rotary evaporation and the remaining product dissolved into methanol (300 mL). Sodium tetraphenylborate (2.24 g) was dissolved in methanol (20 mL) and added dropwise to the bromide salt solution while stirring. A thick white precipitate formed

immediately, which was isolated by vacuum filtration. The solid was dried under dessication and confirmed to be 5-(2'-(methyl)thioxanthone)-1,5-diazabicyclo[4.3.0]non-5-ene tetraphenylborate by H_1 NMR (3.42 g, 78% yield).

3.3.3 UV-Visible Spectroscopy

UV-visible spectroscopy was performed to determine both the wavelength sensitivity of the photo-catalysts and confirm the release of a base following irradiation. The absorbance spectra of QAS-BP between 300 and 400 nm shows an excitation peak ranging from approximately 310 nm to almost 400 nm, peaking at 340 nm. This absorption peak shows an upward shift in absorbance as the solution is irradiated with 365 nm light, eventually doubling in absorbance after ten minutes of exposure (Figure 3.4).

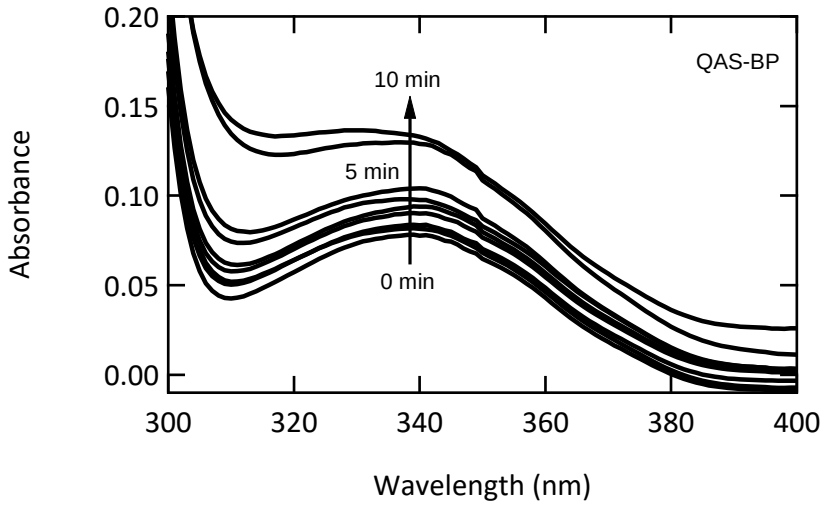

Figure 3.4. UV-vis tests on photolysis of QAS-BP shows spectral changes following irradiation with 365 nm light. The primary absorption spectrum rests between 310 nm and 390 nm, with a peak at 340 nm. The spectrum increases in absorbance as the initiator is irradiated.

Changes in absorption are noticeable almost immediately, even after only 30 seconds of exposure. QAS-BP continues to undergo photolysis up to at least 10 minutes of irradiation. The addition of phenol red indicator shows the change in pH as the 0.1 wt% acetonitrile solution is irradiated with 365 nm light (Figure 3.5). No visible change is seen until 8 minutes of irradiation, after which the solution begins to indicate a strongly basic environment.

QAS-MTX displays similar spectral behavior with some notable variation. The absorbance spectrum of QAS-MTX is red-shifted in comparison to QAS-BP, with the absorbance peak near 380 nm (Figure 3.6). A less drastic change in absorbance is seen following the initial dose of irradiation. A slight upward trend in the absorption peak is visible as irradiation continues, but not to the degree seen in QAS-BP. Phenol red indicator added to the solution following irradiation shows conversion to a basic solution following five minutes of irradiation (Figure 3.7). The conversion to a basic pH occurs more rapidly than seen in QAS-BP, indicating higher photo-reactivity at 365 nm.

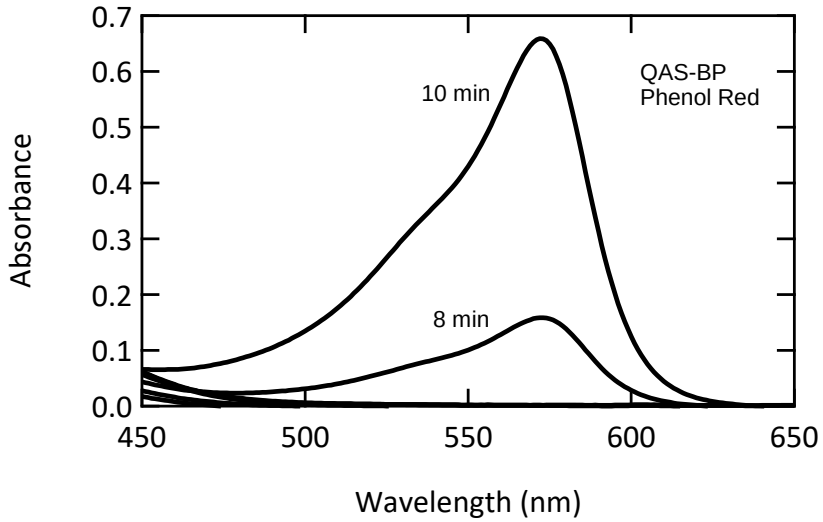

Figure 3.5. UV-vis tests with phenol red solution added following 365 nm irradiation show an increase in solution pH after 8 minutes of exposure.

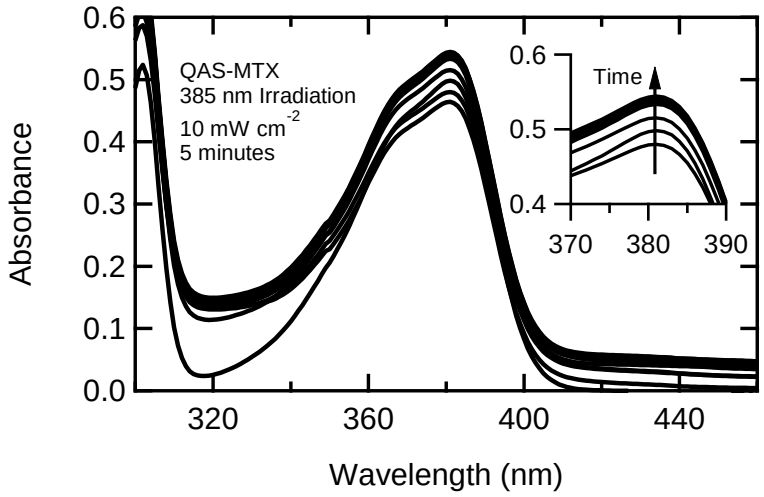

Figure 3.6. UV-vis tests on photolysis of QAS-MTX show a primary absorption spectrum between 320 nm and 410 nm, with a peak at 380 nm. The absorption coefficient increases as the molecule is exposed to 385 nm light.

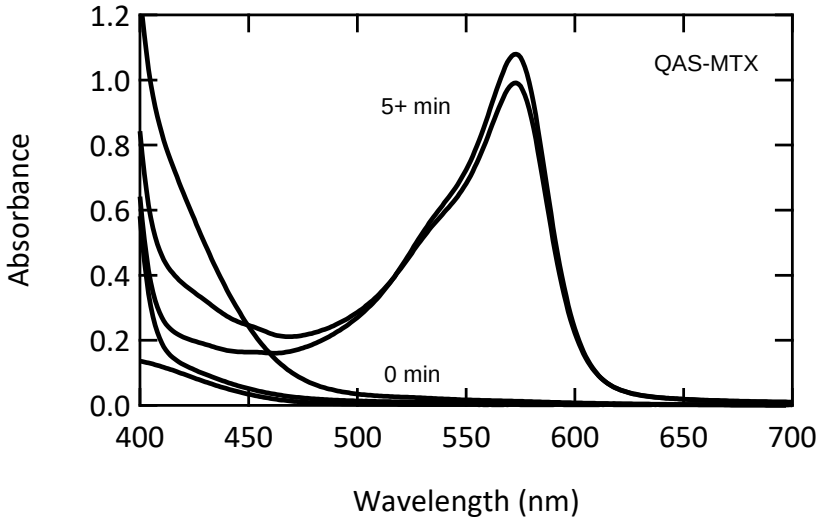

Figure 3.7. Addition of phenol red to irradiated QAS-MTX shows large indication of basicity after undergoing 5 minutes of 365 nm exposure

3.3.4 Polythiourethane Cure Study

The ability of QAS-MTX to catalyze the thiol-isocyanate reaction was studied using FTIR (Figure 3.8). A stoichiometric mixture of EDDT and HDI were mixed with 0.1 wt% of QAS-

MTX and irradiated using a handheld 875 mW 365 nm LED lamp. Prior to irradiation there is a noticeable isocyanate peak near 2250 cm^{-1}. No change in solution viscosity or FTIR signal was seen for up to ten minutes prior to exposure with the UV LED. Following 25 second of irradiation the isocyanate peak becomes substantially smaller in size. This is accompanied by the appearance of peaks at 3300, 1600, 1500, and 1250 cm^{-1} which represent the appearance of the amine, carbonyl, and amide functionalities present in the thiourethane linkage. This suggests that the photo-release of DBN via 365 nm light may rapidly catalyze thiol-isocyanate coupling.

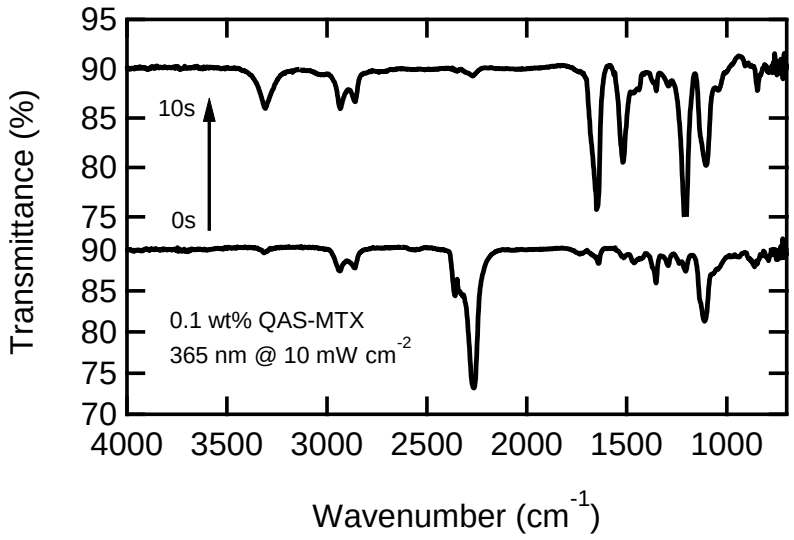

Figure 3.8. Irradiation of pre-polymer resin with QAS-MTX by 365 nm light results in rapid polymerization within 10 seconds, with near complete disappearance of the isocyanate peak near 2250 cm^{-1} and the appearance of secondary amine and urethane peaks at 3300, 1600, 1500, and 1250 cm^{-1}

The reaction rates of EDDT-HDI resin using 0.1 wt% of QAS-MTX was studied by tracking isocyanate conversion during irradiation (Figure 3.9). Thiol content was not tracked due to the extremely weak thiol FTIR signal. The QAS-MTX resin was irradiated using a handheld 365 nm LED with an irradiation intensity of 10 mW cm^{-1}. The resin cures very quickly upon exposure to

an ultraviolet light source. The QAS-MTX resin reaches virtually 100% conversion within 7 seconds of irradiation, a time scale similar to the cure rate of acrylic polymers.

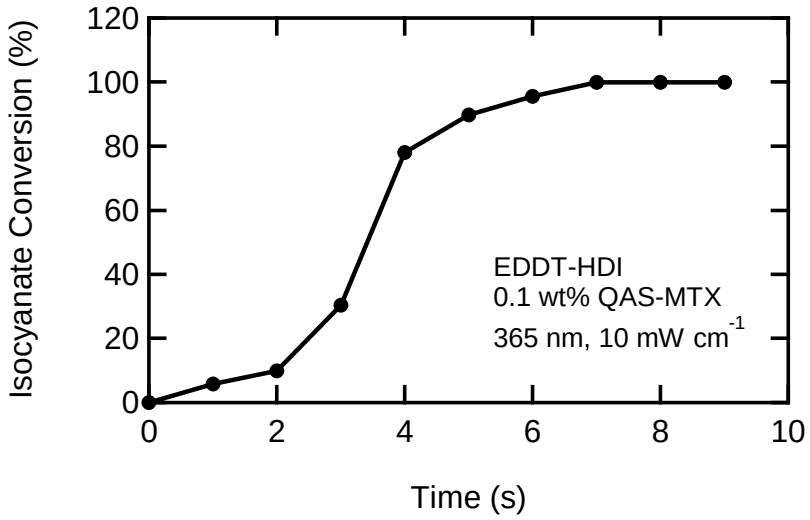

Figure 3.9. Stoichiometric mixtures of EDDT and HDI with 0.1 wt% QAS-MTX cure to complete conversion within 7 seconds of irradiation using a 365 nm source at 10 mW cm^{-1}

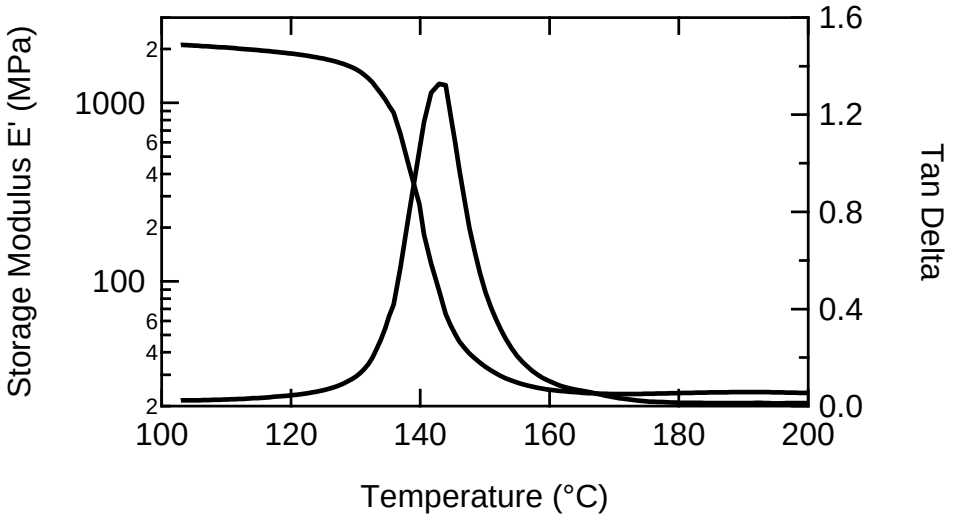

Figure 3.10. Photo-cured polythiourethane thermosets using QAS-BP show high network uniformity achieved with simple cure conditions. A PETMP-IDI tan delta has a full width half max of 10 °C with a peak at 142 °C.

A model polythiourethane thermoset material was cured using QAS-BP to demonstrate the effectiveness of the photo-catalysts for bulk polymerizations. Dynamic mechanical analysis was performed to assess the degree of curing and network uniformity (Figure 3.10). The narrow peak of *tan* δ indicates that the material cured into a homogenous network.

3.4 Discussion

The synthesis of QAS-BP is relatively straightforward due to the availability of brominated precursor material and the drastic solubility changes which occur during the reaction. In both steps, the reaction product precipitates from the solvent while any unreacted material and byproducts remain dissolved. This allows for simple vacuum filtration to isolate the final product with high purity. The reaction scheme of QAS-MTX is more difficult, as the required brominated precursor material is not commercially available in quantities appropriate for research at this time. However, the types of reactions necessary to produce 2-(bromomethyl)thioxanthone are not difficult and are conducted frequently on industrial scales. Once the brominated precursor is obtained, the synthetic procedure is similar to that of QAS-BP and is done with relative ease. The ability to synthesize and purify both photo-catalysts using established techniques lends itself well to increasing the scale of the reactions if needed.

Both photo-catalysts appear to be stable in solution in the dark and for at least six months in ambient conditions when in solid form. Upon exposure to the appropriate wavelength of light however, they rapidly undergo photolysis and release DBN into the solution. Both initiators are photo-active at 365 nm, which is frequently used for initiating polymerizations. QAS-MTX appears to release DBN at a higher rate than QAS-BP at this irradiation wavelength as indicated by phenol red indicator. The absorption peak of QAS-BP has a maximum at 340 nm and

decreases by over half at 365 nm. QAS-MTX has a peak near 380 nm and has substantially higher absorbance throughout this region. In addition to the more conveniently located absorption peak, the QAS-MTX chromophore seems to be a more effective light-absorbing species as indicated by the order of magnitude increase in absorption compared to QAS-BP at similar solution concentrations. This is supported by the reduced irradiation time necessary to induce a change in the phenol red indicator.

FTIR and bulk polymerization testing indicates that the photo-catalysts will serve as highly effective UV-curing agents for thiol-isocyanate polymers. FTIR demonstrates that the tertiary amine released via C-N bond cleavage is capable of catalyzing the thiol-isocyanate coupling which results in thiourethane polymers. Real-time data shows that both the QAS-BP and QAS-MTX initiators are capable of curing resins to near total conversion within 30 seconds of irradiation. QAS-MTX is notably effective as a photo-catalyst, reaching high conversion in under 10 seconds of 385 nm irradiation. However, the absorption spectrum extends slightly above 400 nm, which makes accidental catalysis via ambient light a concern. The decreased excitation spectrum of the QAS-BP initiator allows for easier handling while retaining very high reaction rates.

The bulk-cured polythiourethane network formed via the reaction between PETMP and IDI is highly uniform as determined by DMA. The ability to cure polythiourethane thermosets quickly under mild reaction conditions could prove useful to those working in the thiol-click polymers space. The characteristically high glass transition temperatures and hydrogen bonding present in polythiourethanes are valuable for high-temperature shape memory materials, smart polymers, or other innovative applications.

Future work includes refinement of the synthetic procedure of QAS-MTX for higher yields at larger batch sizes. This initiator has excellent performance in the upper UV range, has high solubility in thiol monomers, and catalyzes polymerization rapidly upon irradiation. It will be important to not only improve synthesis efficiency, but perform further studies on shelf life, dark-stability, resin stability, and potential hazards if this material is to be used in a commercial venue.

3.5 Conclusion

Quaternary ammonium salts have been synthesized which release the strong base 1,5-diazabicyclo(4.3.0)non-5-ene (pKa ~13.5) following irradiation with light. The release occurs rapidly upon irradiation with an oxidation-capable anion such as sodium tetraphenylborate. The required irradiation wavelength is controlled via the choice of the brominated chromophore. The wavelength excitation spectrum for DBN release may be controlled between 300 nm and 400 nm by using benzophenone or thioxanthone derivatives. The photo-catalysts are soluble in thiol-isocyanate monomer solutions and have no observed curing effects in the dark. The initiators cure thiol-isocyanate resins into with almost quantitative conversion upon seconds of irradiation. This enables thiol-isocyanate resins to be processed similarly to the radical initiated thiol-ene polymers, possibly opening a new class of tough high glass transition thermoset materials cured using common ultraviolet and visible light sources.

CHAPTER 4

TOUGH SEMI-CRYSTALLINE THIOURETHANE PHOTOPOLYMERS FOR ADDITIVE MANUFACTURING

Authors – Gregory Ellson, Xavier Carrier, Thomas J. Wallin, Walter E. Voit

The Department of Materials Science and Engineering, RL10

The University of Texas at Dallas

800 West Campbell Road

Richardson, Texas 75080-3021

4.1 Introduction

Photopolymer 3D printing techniques such as stereolithography, digital light synthesis, and polymer jetting are methods which selectively deposit or cure a light-sensitive resin to form a polymer part. These techniques have the advantages of relatively fast print speed, high resolution, and high surface finish. More advanced techniques are able to produce mechanically isotropic parts or simultaneously deposit multiple materials. However, these printing methods are heavily limited by the selection of photopolymers available for use. These materials tend to be acrylate-based oligomers which have mechanical and thermal performance well below that of engineering polymers. The brittle, low glass transition properties of available photopolymers have mostly relegated photopolymer systems to prototyping applications. Further development of tough photopolymers with high heat deflection temperatures are needed to make photopolymer 3D printing an industrially relevant process.

A novel approach to 3D printing resins is described using photo-cured polythiourethanes in place of traditional acrylate chemistries. Quaternary ammonium salts are used to release a strong base catalyst under irradiation with 385 nm light. The ensuing polymerization reaction occurs rapidly in the photo-defined area, allowing complex objects to be generated. The resulting materials may be semi-crystalline, demonstrating toughness and heat deflection temperatures similar to that of high-performance engineering thermoplastics. 3D printed parts utilizing these materials are demonstrated via stereolithography and polymer jetting.

4.2 Experimental Methods

4.2.1 Resin Preparation

The pre-polymer resin was prepared by mixing stoichiometric mixtures of 2,2'-(ethylenedioxy)diethanethiol (EDDT), decanedithiol (DDT), hexamethylene diisocyanate (HDI), tris(6-isocyanatohexyl)isocyanurate (HDI-T), and trimethylhexamethylene diisocyanate (TMHDI) in a planetary mixer. Samples for bulk testing utilized 0.25 wt% QAS-MTX to catalyze the reaction. These samples were cured between glass slides separated by 500 μm spacers in a 365 nm UVP CL-1000L ultraviolet crosslinker for one hour prior to undergoing an 85 °C anneal overnight. Resin for 3D printing used 0.50 wt% of QAS-MTX in order to catalyze the reaction at the projector wavelength in a sufficiently short time for printing.

4.2.2 Photo-Rheometry

Photo-rheometry was performed on a TA Instruments DHR-3 with a UV Light Guide Accessory. The UV source was an Excelitas Omnicure S2000 outputting filtered 365 nm light to the rheometer plates at an intensity of 89.4 mW cm-2, 29.5 mW cm-2, or 8.9 mW cm-2. Resin for TU Tough or TU Durable with 0.1, 0.25, 0.5, or 1.0 wt/wt% of photo-catalyst was pipetted between the plates at room temperature. The measurement was initiated to establish a baseline viscosity reading prior to the UV source being turned on. The light source remained on until the conclusion of the test. All samples were tested in triplicate.

4.2.3 Differential Scanning Calorimetry

Differential scanning calorimetry was performed on a Mettler Toledo DSC1/700. Samples were cut into circular disks 3 mm in diameter and 500 μm thick and placed in 40 μL aluminum

crucibles. Samples were inserted at 50 °C and cooled to -20 °C before undergoing three heating and cooling cycles between -20 °C and 160 °C. The second and third cycles were used to determine polymer T_g. All heating rates were 10 °C min^{-1}. Glass transition temperature was determined using the Mettler Toledo STARe Thermal Analysis Suite. Melting point was taken as the peak of the melt endotherm. At least three samples were tested for each polymer composition.

4.2.4 Heat Deflection Testing

Heat deflection testing specimens were cast in a machined aluminum mold and milled to ASTM D648-16 specifications. Testing was performed by Element Materials Technology (Warren, MI) according to the ASTM D648-16 standard. All samples were tested in triplicate.

4.2.5 Polarized Light Microscopy

Polarized light microscopy was performed on an Olympus BX43 microscope under a cross-polarizing filter. The microscope was fitted with an Olympus DP27 camera system and images were acquired using the Olympus cellSens software suite.

4.2.6 Dynamic Mechanical Analysis

Dynamic mechanical analysis was performed on a Mettler Toledo DMA/SDTA861e. Samples were cut into rectangular bars 30 mm long, 3 mm wide, and 500 µm thick. Samples were loaded into the large tension assembly and underwent a heating ramp from -50 °C to 150 °C at 2 °C min^{-1}. The samples were oscillated at 1 Hz with a force limit of 5 N and strain limit of 0.2% with

a 300% offset. The glass transition by DMA was determined as the peak of tan δ. At least three samples were tested for each polymer composition.

4.2.7 Uniaxial Tensile Testing

Tensile testing was performed on bulk-cured samples and printed dog bones in the x, y, and z axis orientations according to ASTM standard D-638-V. Tests were performed on a Lloyd Instruments (West Sussex, UK) LR5K Plus Universal Materials Testing Machine with a 500 N load cell and Laserscan 200 laser extensometer. At least five samples of each type were strained at a rate of 50 mm min^{-1} until sample failure. Tensile strength was taken as the maximum stress experienced by the polymer. Toughness was taken as the area under the stress-strain curve from the origin to the point of failure.

4.2.8 3D Printing

Stereolithography was performed using an in-house system utilizing a Keynote Photonics LC-4500UV projector outputting 385 nm light with irradiation power of approximately 10 mW cm^{-1}. The printer design utilized the "top down" configuration in which the projector shines down onto the surface of the resin, polymerizing the layer on the uppermost surface exposed to the air (Figure 4.1). To minimize resin use the vat was filled with Fomblin M03, a low-viscosity perfluorinated polyether oil. Fomblin has a high density of 1.85 g cm^{-3}, is chemically inert, and is immiscible with the thiol-isocyanate resin. The thiol-isocyanate resins sit on top of the Fomblin, with no detectable physical or chemical interactions between the two. To refresh a layer of resin over the cured material, a New Era Pump Systems NE-1000L syringe pump fitted with two 140 mL syringes was used to add enough Fomblin to the vat to fully wet the surface of the cured part

and then remove enough Fomblin to leave a 100 μm layer of resin on the surface of the part. An Arduino-controlled stepper motor moved the projector vertically to keep in focus with the current layer. The projector then cured the next layer and the process was repeated until the desired part was formed. The part was removed from the vat and washed with ethyl acetate before undergoing a 60 minute post-cure at 140 °C to complete the polymerization process. Tough samples were post-cured at 180 °C. Durable and Tough samples were then annealed at 85 °C for at least 12 hours. Elastomeric samples were not annealed and were able to be tested immediately.

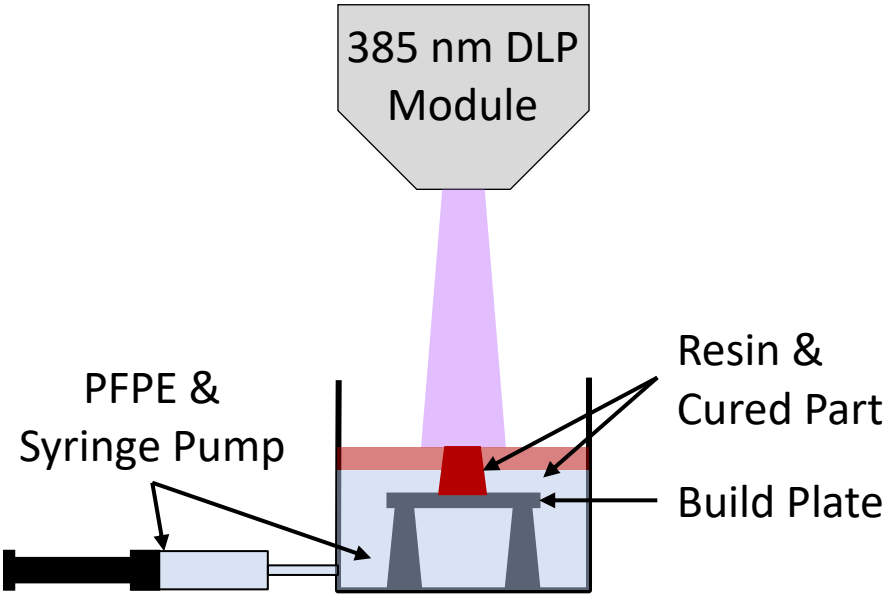

Figure 4.1. Schematic representation of top-down printing configuration; a 385 nm DLP projector patterns light on the surface of the resin, curing the part. A syringe pump controls the amount of Fomblin M03 in the vat, controlling the height of the resin.

Polymer jetting was performed in collaboration with the Computational Fabrication Group at the Massachusetts Institute of Technology. The *TU Tough*, *Durable*, and *Elastic* resins were printed on the MultiFab printer with no necessary modifications. Parts were fully cured following printing, requiring no post-cure.

4.2.9 Scanning Electron Microscopy

Scanning electron microscopy was performed on cold-fractured specimens using a Zeiss Supra 40. Specimens were coated with 3 nm of gold-titanium using a Hummer VI sputter deposition system prior to imaging. Images were taken at 5.00 kV using a 30.00 μm aperture.

4.3 Results

4.3.1 Resin Formulation

Polymers comprised of EDDT, DDT, HDI, HDI-T, and TMHDI were cured in order to produce a polymer system with tunable thermo-mechanical performance via control over crystallinity. The base material used for this study is the *TU Durable* material, which is composed of EDDT, HDI, and a small amount of HDI-T to crosslink the polymer and allow printing. Two variants of this resin, *TU Tough* and *TU Elastic*, were designed containing DDT or TMHDI in addition to the base monomers (Table 4.1).

Table 4.1. Monomer formulations for *Tough*, *Durable*, and *Elastic* thiourethane thermoset photopolymers

Sample	EDDT	DDT	HDI	TMHDI	HDI-T
TU Durable	100	0	94	0	6
TU Tough	45	55	94	0	6
TU Elastic	100	0	44	50	6

4.3.2 Photo-rheometry

Photo-rheometry was performed to confirm the ability to cure the *TU Tough* and *TU Durable* resins fast enough to allow printing via stereolithography. Cure times are dependent on both the

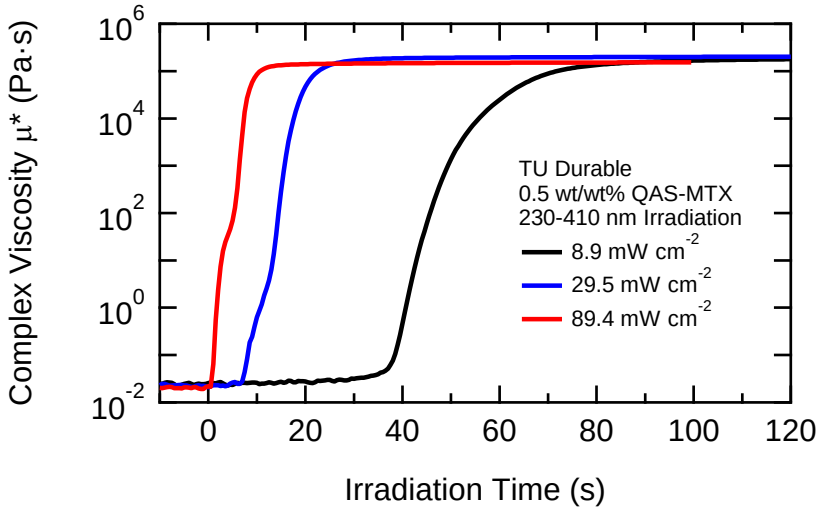

Figure 4.2. Power-dependent photo-rheometry of *TU Durable* resin containing 0.5 wt/wt% of QAS-MTX. Gel initiation occurs immediately at higher irradiation levels, with full cure achieved in as little as 10 seconds.

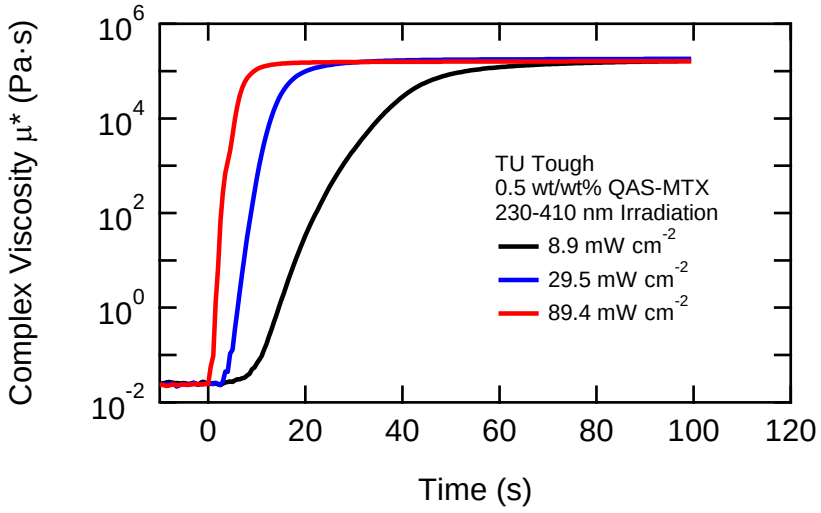

Figure 4.3. Power-dependent photo-rheometry of *TU Tough* resin containing 0.5 wt/wt% of QAS-MTX. Gel initiation occurs immediately at higher irradiation levels, with full cure achieved in as little as 5 seconds. Curing speed is increased in comparison to the Durable composition.

irradiation intensity and loading fraction of QAS-MTX. TU Tough containing 0.5 wt% of QAS-MTX hardens in as little as 9 seconds under 230-410 nm irradiation at 89.4 mW cm^{-2} (Figure 4.2). Hardening time increases to 22 and 80 seconds as the UV intensity is reduced to 29.5 mW

cm^{-2} and 8.9 mW cm^{-2}, respectively. There is a similar correlation to the gel initiation point, indicated as the time at which the viscosity begins to increase. At high power, gelling starts immediately upon the light source turning on. This initiation time increases to 8 and 35 seconds as the power is decreased. The *TU Tough* resin cures more rapidly at 0.5 wt/wt% QAS-MTX (Figure 4.3). Hardening times decrease to 7, 20, and 60 seconds with gel initiation points of 0, 3, and 10 seconds at 89.4, 29.5, and 8.9 mW cm^{-2}, respectively.

4.3.3 3D Printing

3D printing was demonstrated using the *TU Durable*, *TU Tough*, and *TU Elastic* photopolymer resins. *TU Durable* and *TU Elastic* required 6 seconds or irradiation per layer for appropriate curing, while *TU Tough* required only 3 seconds per layer with 0.5 wt/wt% of QAS-MTX.

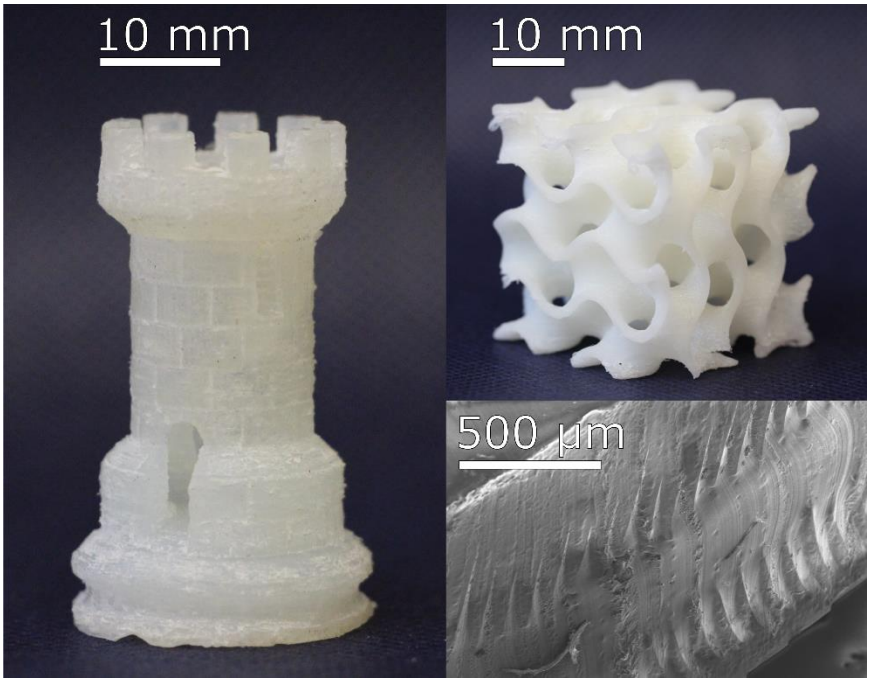

Figure 4.4. 3D printed chess rook with an internal staircase and 35 mm x 35 mm x 35 mm gyroid cube. Scanning electron microscopy of fractured samples shows 100 µm layering

Printed parts had layer heights of 100 µm or 150 µm, depending on the height of the part and the desired printing time. In addition to testing specimens, complex structures such as a chess rook and gyroid cube were fabricated (Figure 4.4). These specimens have complex internal structures that are difficult or impossible to produce via traditional manufacturing processes.

A calibration pattern was printed with the *TU Durable* material on the MultiFab polymer jetting printer to demonstrate the resolution capability of the system (Figure 4.5). Feature sizes less than 1 mm are clearly discernable. The print utilized a 20 µm layer height, resulting in high surface finish and no discernable layering in the printed object.

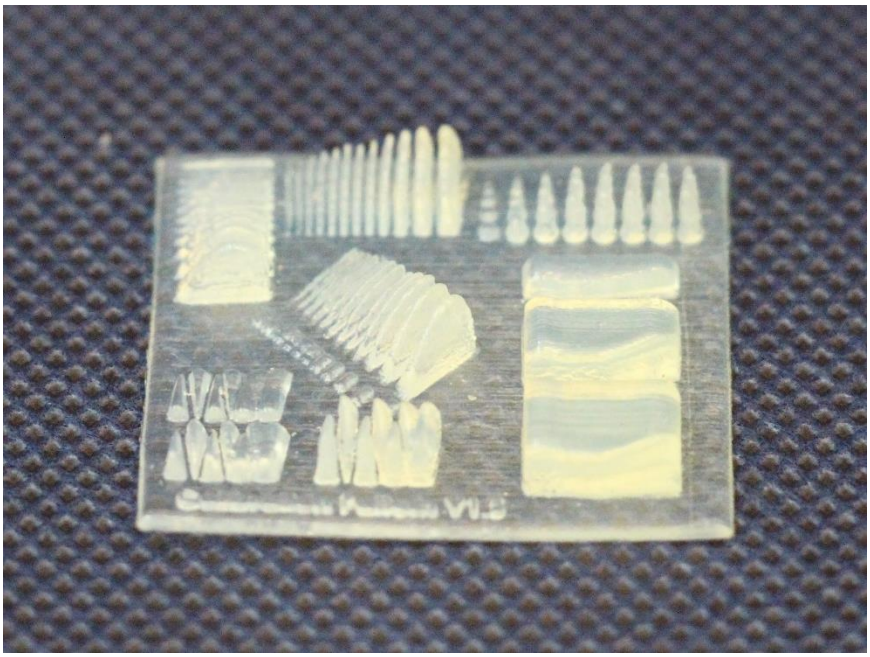

Figure 4.5. Calibration pattern printed using *TU Durable* on a MultiFab printer. Feature sizes less than 1 mm are clearly defined with a 20 µm layer height.

4.3.4 Thermal Analysis

The effects of altering the base material formulation are shown via differential scanning calorimetry (Figure 4.6). The base *Durable* material using only EDDT as the dithiol chain

extender has a glass transition temperature near 11 °C with a crystal melt occurring between 100 °C and 120 °C. Crystallinity is enhanced when replacing EDDT with DDT. In the DDT-containing *Tough* material, the glass transition temperature remains near 11 °C, but the crystal behavior changes. The melt transition increases in temperature to between 130 °C and 155 °C and the magnitude of the melt endotherm is larger than for the *Durable* composition. The crystal melt transitions of *TU Durable* and *TU Tough* correlate well to their 0.45 MPa heat deflection temperatures as determined by ASTM D648, with respective values of 101.4 ± 3.5 °C and 136.1 ± 1.8 °C. Crystallinity is reduced when replacing the HDI with TMHDI. Glass transition temperatures remain at 11 °C for the *Elastic* material containing TMHDI, but the crystal melt previously seen in the *Durable* material disappears entirely. As a result, the *Elastic* composition is completely amorphous.

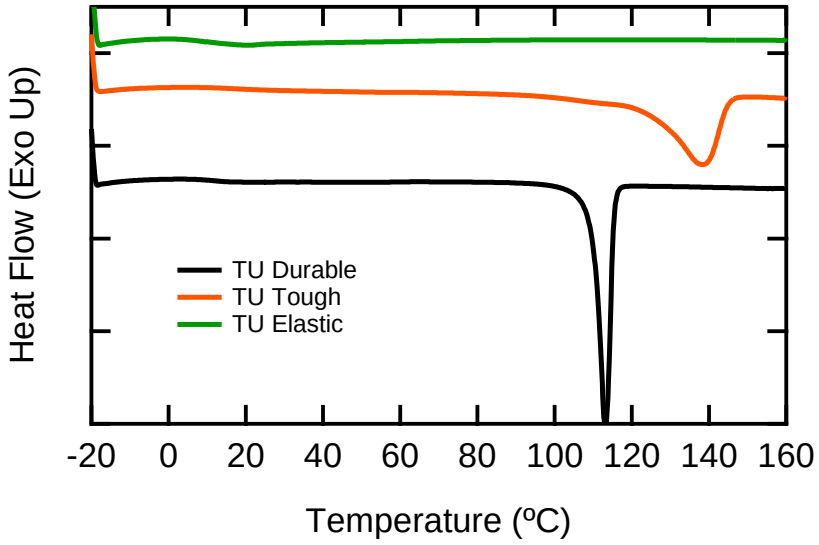

Figure 4.6. Differential scanning calorimetry showing variation in glass transition temperature and crystallinity with addition of DDT or TMHDI to base composition. All samples have glass transition temperatures of 11 °C. *TU Durable* has a crystal melt near 110 °C, while *TU Tough*'s melt is near 140 °C. *TU Elastic* is amorphous and has no crystal melt.

DSC was also used to assess any differences between the materials when cast in the bulk versus when they are printed (Figure 4.7). The *TU Durable* resin shows no change in glass transition temperature when printed, remaining at 11 °C. The crystal melt endotherm is broadened slightly, taking place between 90 °C and 120 °C when printed in comparison to 100 °C to 120 °C in the bulk. Neither resin recrystallizes immediately upon cooling, requiring annealing at 85 °C in order to recrystallize.

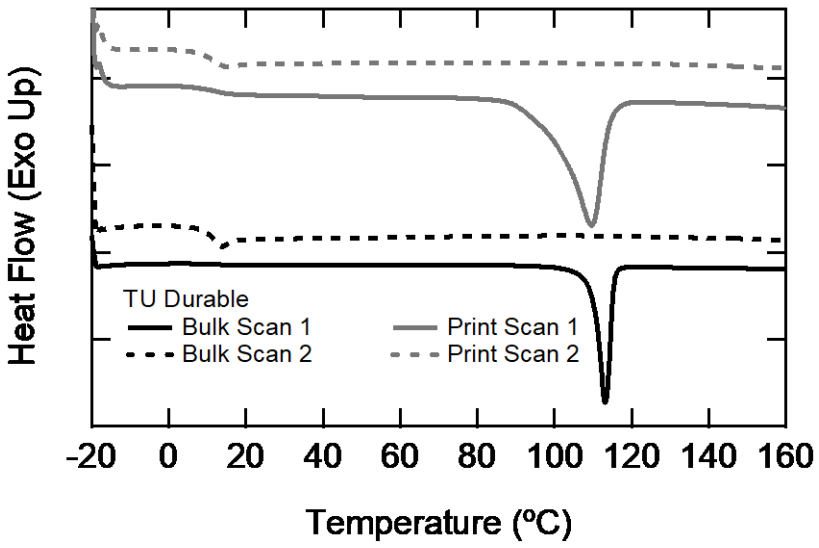

Figure 4.7. Differential scanning calorimetry of *TU Durable* in the bulk and when 3D printed following post cure and annealing. Little variation exists in DSC between bulk and printed samples, with glass transition and crystal melt transitions remaining near 11 °C and 110 °C.

4.3.5 Uniaxial Tensile Testing

Tensile behavior shows a pattern dependent on the polymer crystallinity (Figure 4.8, Table 4.2). *TU Durable* is a flexible material with a yield stress of about 36 MPa, straining afterwards at a relatively constant 31 MPa until failure at 46 MPa and 255% strain. The higher crystallinity *Tough* polymer has an increased yield and failure stress, at 50 MPa and 60 MPa respectively. The failure strain is statistically identical to *TU Durable*. The amorphous *TU Elastic* resin

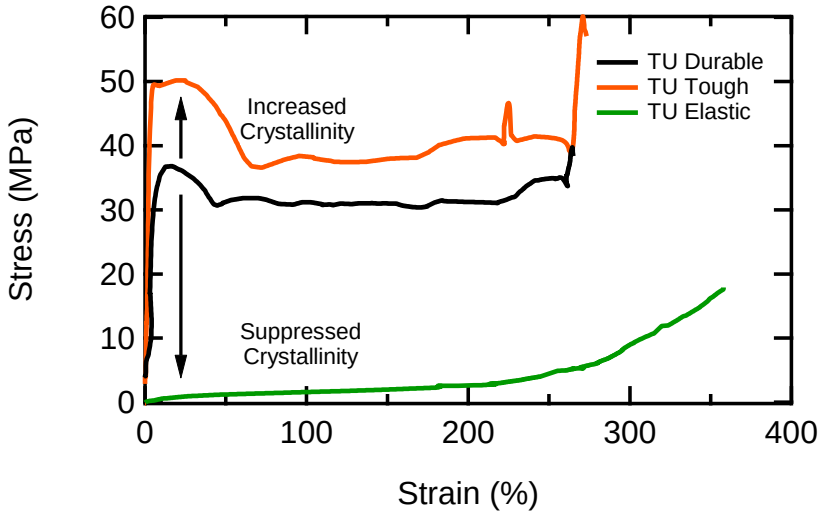

Figure 4.8. Tensile properties of *TU Durable*, *Tough*, and *Elastic* resins in the bulk change as a function of crystallinity. Semi-crystalline resins undergo yielding and plastic deformation. Yield and failure stresses increase or decrease with crystallinity. Amorphous samples behave as elastomers.

behaves as an elastomer, showing no yield point and straining to 360% strain before failing at 19 MPa.

Differences between bulk and printed parts are only apparent in mechanical testing, where the yield stress shows a tendency to decrease as the layering effect is increased (Figure 4.9, Table 4.2). The bulk *TU Durable* material yields near 36.3 ± 1.7 MPa and strains at approximately 30 MPa until failure at 254 ± 35% strain. X-axis dog bones show a slightly decreased yield of 31.8 ± 1.0 MPa. The yield stress continues to decrease in the Y and Z-axis dog bones, with respective yield stresses of 25.7 ± 2.1 MPa and 22.2 ± 0.8 MPa. However, it is important to note that the failure strains remain similar for the bulk and both printed orientations, in the 240% to 280% range. As a result, the toughness of the printed *TU Durable* material remains quite high even in the Z-axis, at 53.5 ± 10.5 MJ m^{-3}. While this represents a 40% decrease in toughness compared to the bulk material, it remains over twice as large as the comparable acrylic photopolymer. The

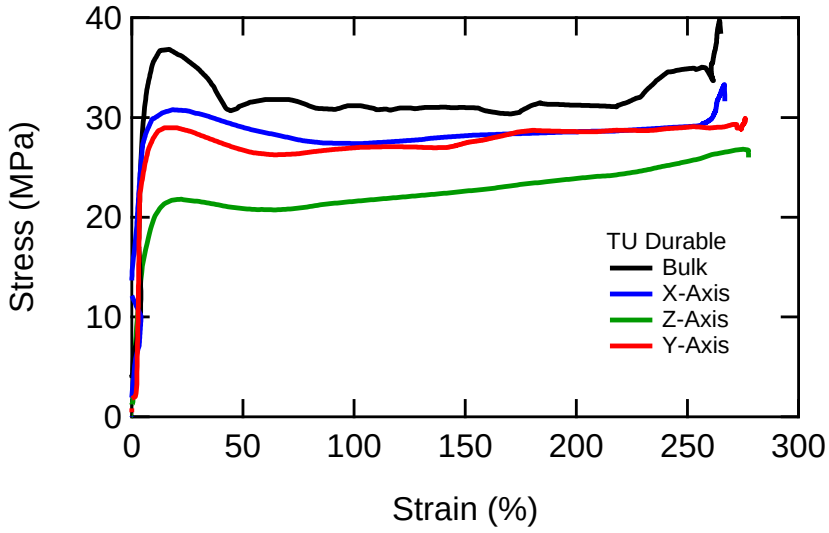

Figure 4.9. Tensile performance of *TU Durable* in the bulk and when tested in the X, Y, and Z orientations. Performance decreases with respect to the bulk material as the layering effect is increased from the X, to Y, to Z orientations. Yield stresses decrease from 36 MPa to 22 MPa, while failure strains remain largely the same.

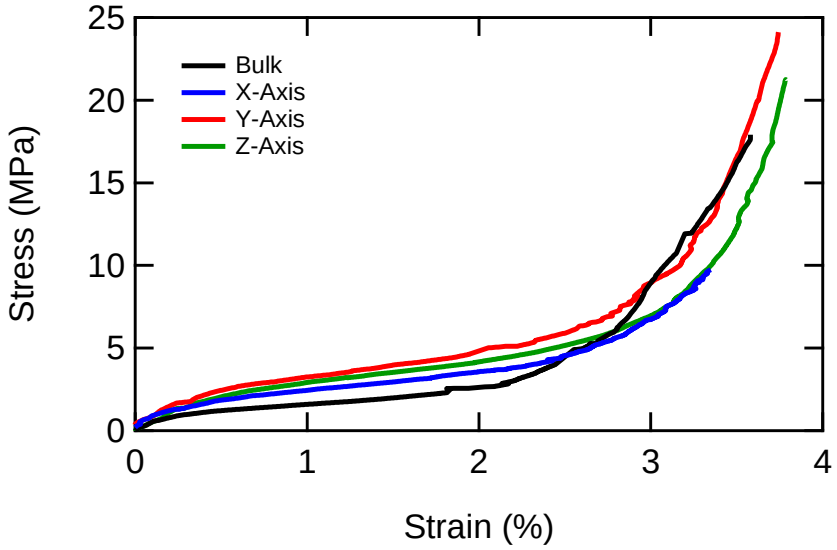

Figure 4.10. Tensile performance of *TU Elastic* in the bulk and when tested in the X, Y, and Z orientations. Failure stresses and strains are statistically equal, although stresses in the bulk sample tend to be lower than printed parts prior to failure.

amorphous *TU Elastic* shows no significant degree of anisotropy, with failure stresses and strains in the range of 19 MPa and 350% for the bulk material and 3D printed parts in the Y and Z testing orientation (Figure 4.10). X-axis samples are the exception, with decreased tensile stress of 9.5 ± 2.3 MPa while retaining high failure strains of 363 ± 39%.

Table 4.2. Tensile properties of polythiourethane resins in the bulk and when printed in the x, y, and z axis orientations via stereolithography

Sample	Axis	Yield Stress (MPa)	Tensile Strength (MPa)	Failure Strain (%)	Toughness (MJ m^{-3})
TU Durable	Bulk	36.29 ± 1.71	46.40 ± 7.79	254.08 ± 35.26	90.35 ± 10.64
	X	31.82 ± 0.97	32.57 ± 6.23	253.92 ± 59.82	71.28 ± 15.80
	Y	25.70 ± 2.05	30.91 ± 4.69	236.41 ± 34.80	62.43 ± 12.59
	Z	22.17 ± 0.80	26.23 ± 2.96	239.00 ± 40.02	53.46 ± 10.51
TU Tough	Bulk	49.84 ± 0.93	55.27 ± 9.48	290.32 ± 20.83	119.55 ± 14.64
TU Elastic	Bulk	-	19.59 ± 5.30	352.76 ± 27.05	15.46 ± 3.54
	X	-	9.53 ± 2.25	362.71 ± 39.50	14.33 ± 2.08
	Y	-	21.81 ± 8.08	358.91 ± 35.92	19.64 ± 5.43
	Z	-	18.74 ± 9.84	355.69 ± 29.73	17.21 ± 5.98

4.4 Discussion

3D printing has been touted as a revolution in manufacturing for decades. However, these predictions have not yet come to pass because of a number of technological hurdles. Photopolymer systems such as stereolithographic addition, continuous digital light processing, and polymer jetting are of particular interest due to their high speed, surface finish, and detail.

However, parts produced via these printing methods famously suffer from brittle behavior and poor thermal resilience. This is directly caused by the acrylate chemistry used in the photopolymer resins, as acrylic materials are tend to have high degrees of crosslinking, low glass transition temperatures, and weak chain interactions. The response of materials scientists so far has been to use interpenetrating networks of epoxides or polyurethanes, where the acrylic material serves to hold the shape of the part while the secondary network is thermally cured following printing. This has improved mechanical toughness to a degree, but heat deflection temperatures remain low. The best "engineering grade" photopolymers today will soften prior to reaching 60 °C, which is inferior to temperatures achievable with typically used materials such as polyamides. Photopolymer 3D printing systems simply will not see adoption on an industrial scale until chemistries are developed which enable printing parts as mechanically and thermally tough as common injection molded materials.

There is compelling evidence that photo-cured polythiourethanes offer the combination of rapid cure kinetics, low cure stress, high toughness, and thermal resilience necessary to make photopolymer 3D printing an industrially viable manufacturing method. Section 4.3.2 demonstrates that polythiourethanes can be photo-cured using the novel quaternary ammonium salt photo-catalyst described in Chapter 3. The step-growth mechanism of the thiol-isocyanate coupling allows the polymer to gel late in the polymerization process. This reduces the warping and shrinking experienced by the material in comparison to acrylates, whose chain-growth mechanism causes early gelation and extensive warping. Cure times are similar to acrylates, with layer cure times below 5 seconds possible using commercially available light sources for additive manufacturing systems. Short cure times are critical for ensuring brief fabrication times.

The semi-crystalline nature of the thiourethane system presented here is unique to photo-cured materials. Acrylate-based photopolymers are almost always amorphous materials. A polymerized acrylate chain will not crystallize on its own. Since the photopolymer resin itself must have adequately low viscosity to print, a crystallizing oligomer is virtually impossible to print. The thiourethane system is unique because the monomers are very low viscosity, yet crystallize upon curing. This is due to the thiourethane bond formed during curing.

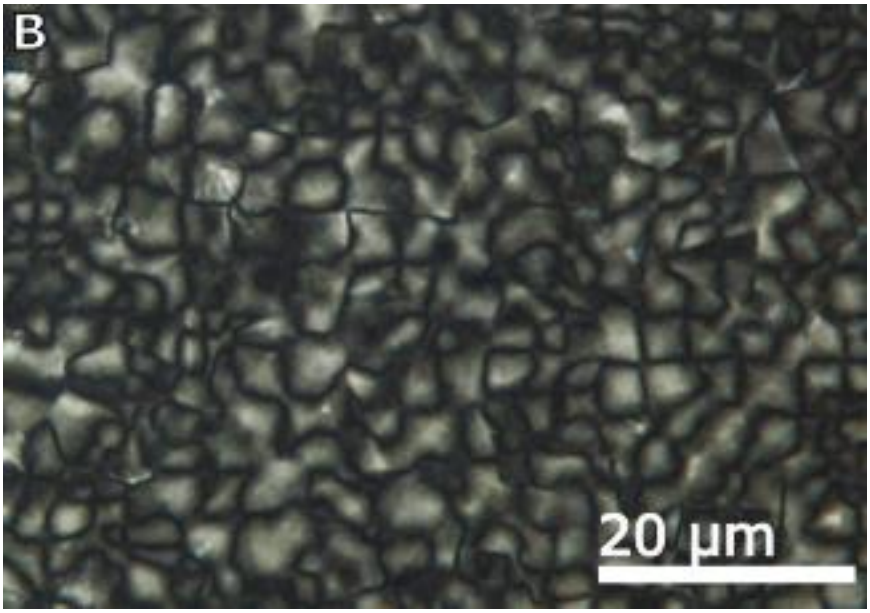

Figure 4.11. Polarized light microscopy of *TU Durable* shows 5 to 10 µm spherulites surrounded by rubbery, amorphous material. This microstructure is similar to that of polypropylene.

The unreacted thiol and isocyanate monomers have low polarity, but the thiourethane bond is highly polar and is an excellent hydrogen bonding site. This change is what supports the crystallinity that is seen via DSC in Section 4.3.4. The result is that the thiourethane photopolymer has a microstructure composed of spherulites 5 to 10 µm in size surrounded by amorphous regions of rubbery material, similar to polypropylene (Figure 4.11).

The materials formulated in Section 4.3.1 have excellent thermo-mechanical behavior, with high toughness and heat deflection temperatures. The base resin, *TU Durable*, compares well to polypropylene with similar yield stresses and strain capacity (Figure 4.12). Bulk polypropylene is capable of strains of up to 450%, whereas the thiourethane reaches 260% strain prior to failure. In comparison, "polypropylene simulation" acrylic resin will fail at under 100% strain and has a low yield stress of only 22 MPa. Similar behavior is seen when comparing *TU Tough* to commercially available acrylics and engineering materials (Figure 4.13). Tough acrylic resins are designed to simulate the mechanical performance of ABS, which they do successfully. Both the acrylics and ABS have yield stresses in the 40-50 MPa range and fail at less than 20% strain. The thiourethane also yields near 50 MPa but strains up to 260% before failure. This behavior is more like a polyamide, which demonstrates yield stresses between 25 MPa and 60 MPa and failure strains between 250% and 500% depending on the grade. Notably, only specific grades of polyamides are capable of 3D printing in filament and powder bed sintering systems, and have substantially reduced mechanical performance compared to the bulk properties shown here. Similarly, the *TU Elastic* material brings performance in-line with EPDM rubber, a widely used commercial elastomer. EPDM has a strain capacity of up to 600%, whereas the thiourethane is capable of straining up to 350%. Acrylic materials are only capable of 200% strain at best.
The similarity in tensile behavior to the engineering materials is reflected in the toughness, taken as the integrated area of the stress-strain curve (Figure 4.15, Figure 4.16, Figure 4.17). The tough, durable, and elastic thiourethane photopolymers have respective toughness of 112.4 MJ m^{-3}, 90.4 MJ m^{-3}, and 14.9 MJ m^{-3}. This represents an order of magnitude improvement over the acrylic counterparts in all cases, which have respective toughness of approximately 9.9 MJ m^{-3},

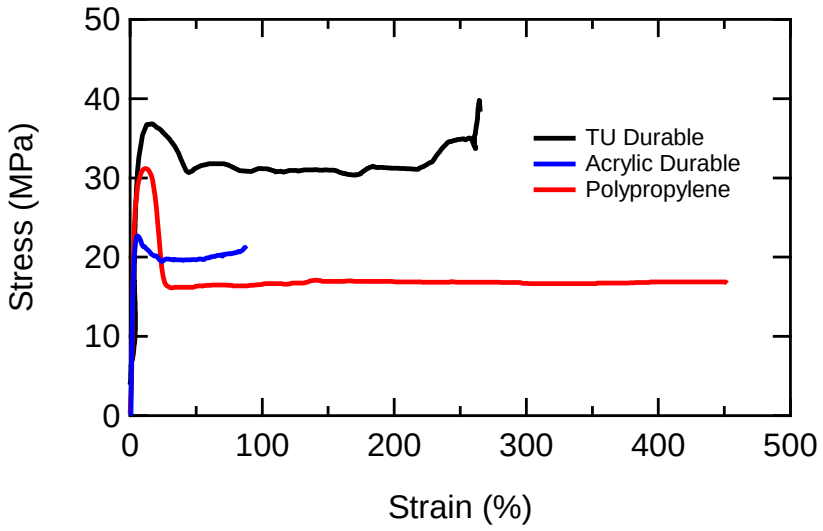

Figure 4.12. Tensile performance of *TU Durable* compared to polypropylene and a commercially available durable acrylic photopolymer resin. Failure stresses and strains of the thiourethane are much higher than the acrylic resin, with slightly higher yield stress than polypropylene but lower failure strain.

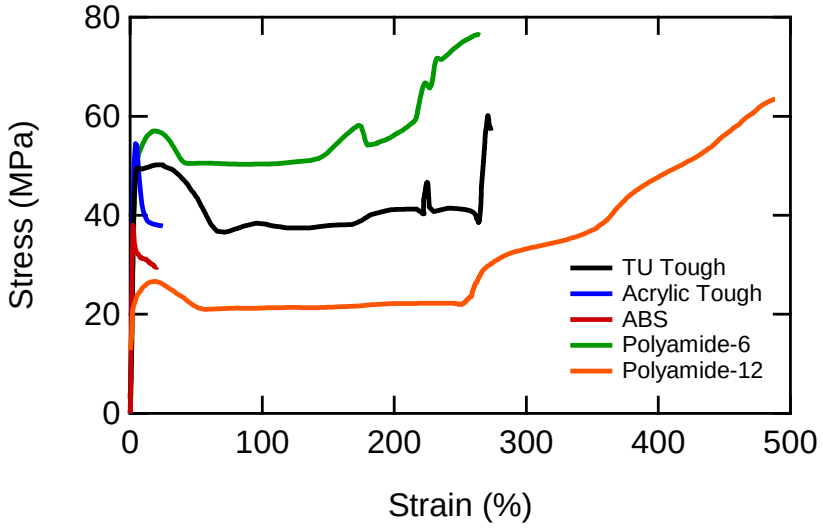

Figure 4.13. Tensile performance of *TU Tough* compared to a tough acrylic photopolymer resin, ABS, polyamide-6, and polyamide 12. The thiourethane has approximately 10 times the strain capacity of a tough acrylic or ABS, with tensile performance between that of polyamide-6 and polyamide-12.

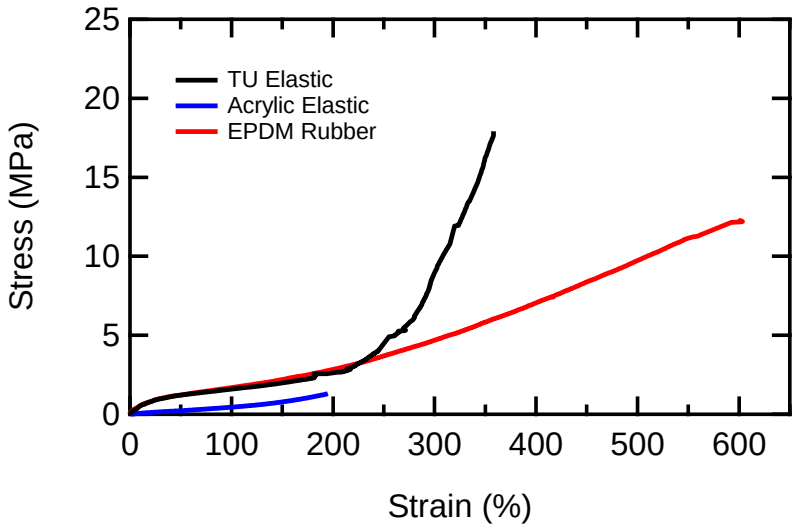

Figure 4.14. Tensile performance of *TU Elastic* compared to EPDM rubber and a commercially available elastomeric acrylic photopolymer resin. The thiourethane elastomer has initial tensile behavior much like EPDM before failing at a higher stress but lower strain. Stresses are much larger than that of a comparable acrylic.

17.5 MJ m^{-3}, and 1.0 MJ m^{-3}.(*59-61*) Toughness is now on the same order as polyamide, polypropylene, and EPDM rubber.

Also of interest is the heat deflection behavior of the semi-crystalline thiourethanes. Typical tough and durable acrylic photopolymers gain their flexibility by bringing the glass transition temperature close to ambient temperatures. While this improves the mechanical performance, it comes at the cost of reduced heat deflection temperatures. Example heat deflection temperatures of tough and durable acrylic photopolymers are 63 °C and 43 °C.(*59-61*) Because the mechanical performance of the thiourethane photopolymers are not linked to their glass transition, their mechanical strength is largely preserved up to the crystal melting point of the material. As a result, the *TU Tough* and *TU Durable* photopolymers have heat deflection temperatures of 136.1 °C and 104.4 °C, over double that of the corresponding acrylic materials. These temperatures are

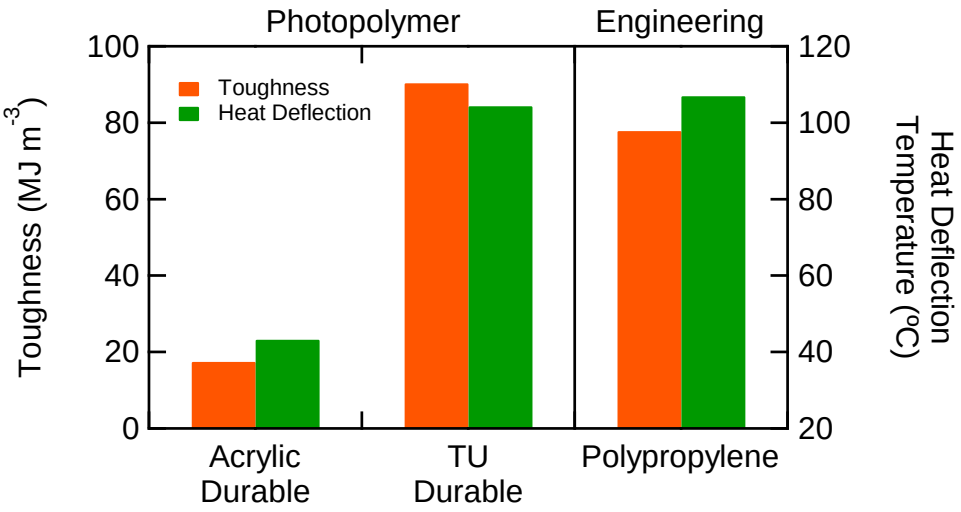

Figure 4.15. Toughness and heat deflection temperatures of *TU Durable*, polypropylene, and an acrylic polypropylene simulation. *TU Durable* has similar toughness and heat deflection to polypropylene, which several times the value of a the acrylic.

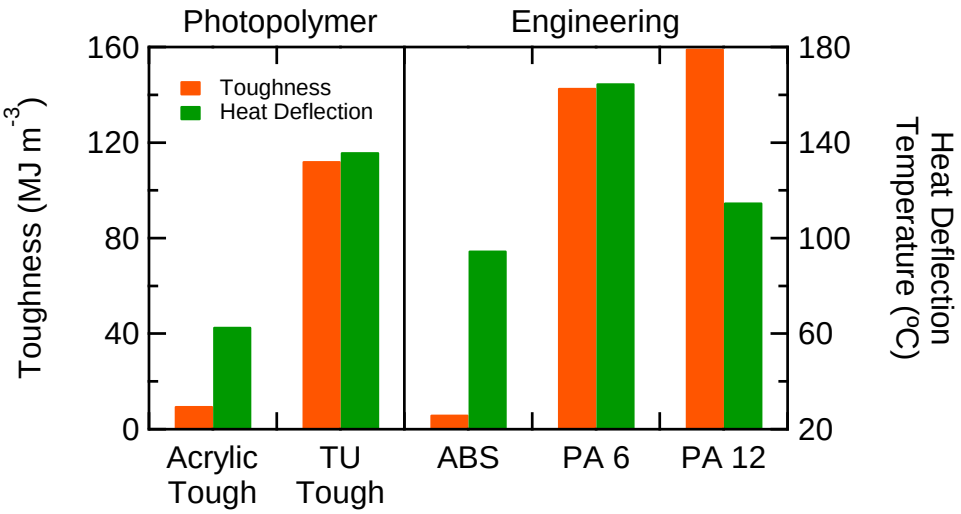

Figure 4.16. Toughness and heat deflection temperatures of *TU Tough*, a tough acrylic resin, ABS, polyamide-6, and polyamide-12. The thiourethane has slightly lower toughness than the polyamides, but is 10 times as large as ABS and the acrylic. Heat deflection temperature is over twice as high as the acrylic resin.

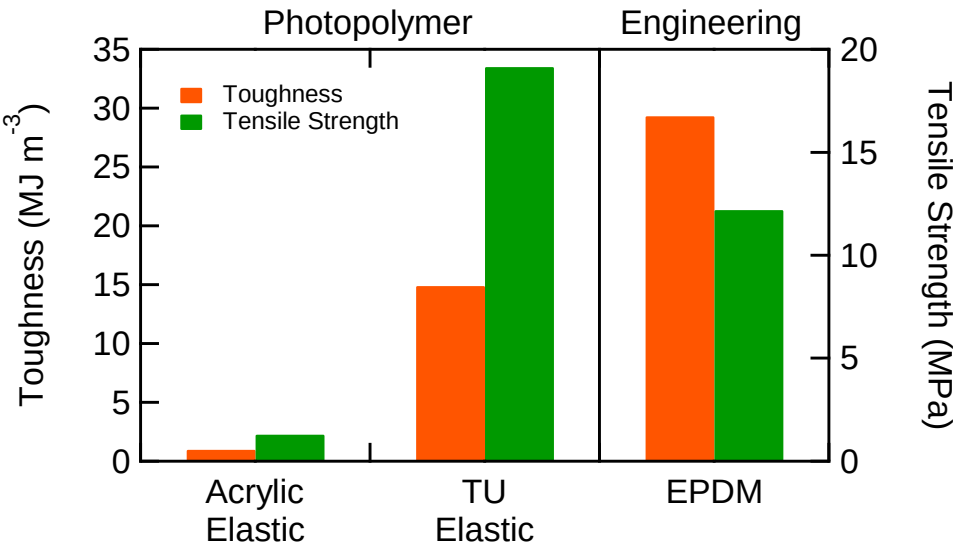

Figure 4.17. Toughness and tensile strength of *TU Elastic*, EPDM rubber, and an elastomeric acrylic material. *TU Elastic* has an order of magnitude increase in toughness and failure stress over the acrylic, with values similar to EPDM rubber.

also in-line with polyamide and polypropylene, whose heat deflection temperatures are also linked to their crystalline melt. *TU Tough* has a deflection point between PA-6 and PA-12, whereas *TU Durable* is nearly identical to polypropylene. While cyanate ester-based high temperature acrylics exist, they tend to be brittle. The author is unaware of any current 3D print-capable photopolymer existing today which has the combination of toughness and thermal resilience shown in this work.

4.5 Conclusion

Polypropylene, polyamide, and EPDM rubber are examples of engineering polymers that see wide use due to their excellent thermal and mechanical properties. Acrylate-based photopolymers have been unable to match the performance of these materials in 3D printing system due to limitations in their chemistry. We have demonstrated that photo-cured thiol-

isocyanate resins have dramatically improved toughness and heat deflection temperatures by virtue of their semi-crystalline nature. Toughness is improved by over 10 times and heat deflection by 2 times compared to similar acrylic materials. Performance now matches that of the engineering-grade resins, opening photopolymer 3D printing systems to functional applications that have been elusive thus far.

CHAPTER 5

TOUGH THIOURETHANE THERMOPLASTICS FOR FUSED FILAMENT FABRICATION

Authors – Gregory Ellson, Xavier Carrier, Jamie Walton, Samsuddin Faisal Mahmood, Kejia Yang, Joshua Salazar, Walter E. Voit

The Department of Materials Science & Engineering, RL10

The University of Texas at Dallas

800 W Campbell Road

Richardson, Texas 75080-3021

5.1 Introduction

Additive manufacturing is the act of synthesizing three-dimensional objects through successively forming layers of material from a computer model. It enables rapid prototyping and design optimizations that are unable to be produced through conventional manufacturing techniques. Additive manufacturing comes in many forms depending on the desired printing speed, resolution, material used, and quality of the final part. Fused filament fabrication (FFF) is the most common 3D printing method implemented today. In FFF a plastic filament is typically fed into a heated print head, which melts the polymer and allows it to be extruded through the end of the print head. The extruded filament is laid down onto a print bed in successive two-dimensional layers until the part is completed. One major difficulty that has been encountered in FFF is the incompatibility of commonly used engineering polymers with this printing technique. Many engineering polymers common to industry are unable to be printed via FFF due to their high processing temperatures, which commercial printing nozzles cannot reach. Some of these materials have been successfully modified for compatibility with FFF, but many remain out of reach. Thus, there is a growing amount of interest in leveraging existing chemistries to develop new materials that have desirable mechanical performance while retaining sufficiently low processing temperatures.

This work reports the synthesis of tough polythiourethane thermoplastics which are easily 3D printed and provide excellent mechanical performance. The polymer produced via the reaction of 2,2'-(ethylenedioxy)diethanethiol and hexamethylene diisocyanate is shown to be synthesized quickly and at scale. The material has a favorably low melting point, allowing it to be easily processed into filament and 3D printed under typical conditions. The material has very high

toughness in the bulk and printed state, outperforming a commercially available ionomer thermoplastic.

5.2 Experimental Methods

5.2.1 Synthesis of poly[2,2'-(ethylenedioxy)diethanethiol-co-hexamethylene diisocyanate]

227.88 g (1.25 mol) of EDDT and 210.24 g (1.25 mol) of HDI were added to a dried 5 L 3-neck round bottom flask with 650 mL of anhydrous DMF while stirring. 0.316 g (0.003 mol) TEA was dissolved into 100 mL DMF and transferred to an addition funnel. The flask was purged with dry nitrogen prior to the TEA solution being added dropwise over the course of two minutes. The reaction was allowed to proceed for 30 minutes at room temperature. Following completion of the reaction, the solution was poured into a deionized water bath, resulting in precipitation of the cured polymer. The material was washed further with water and dried under vacuum at 70 °C, leaving 430 g (99.97% yield) of poly[2,2'-(ethylenedioxy)diethanethiol-co-hexamethylene diisocyanate].

5.2.2 Gel-Permeation Chromatography

Gel permeation chromatography (GPC) was performed on a Shimadzu HPLC with refractive index detector and Agilent polystyrene columns. A polystyrene standard was used for calibration. Samples were dissolved into N,N'-dimethylformamide and passed through the system at 40 °C and 1 mL min^{-1}.

5.2.3 Nuclear Magnetic Resonance Spectroscopy

Nuclear magnetic resonance spectroscopy (NMR) was performed on a Bruker Avance III 500 MHz. Monomers were dissolved into chloroform-D and polymer samples were dissolved into DMSOD6 prior to undergoing 16 scans. NMR data was analyzed using Bruker TopSpin software.

5.2.4 Fourier-Transform Infrared Spectroscopy

Fourier-transform infrared spectroscopy (FTIR) was performed on a Shimadzu IRAffinity-1 with an ATR attachment. Samples were pressed into direct contact with the ATR crystal and scanned 48 times between 4000 cm^{-1} and 800 cm^{-1} at a resolution of 0.1 cm^{-1}.

5.2.5 Differential Scanning Calorimetry

Differential scanning calorimetry (DSC) was performed on a Mettler Toledo DSC 2. Approximately 10 mg of polymer was sealed in a 40 µL aluminum crucible. The sample was inserted at 50 °C and the temperature lowered to -50 °C. The sample then cycled between -50 °C and 200 °C three times. All heating rates were 10 °C min^{-1}.

5.2.6 Dynamic Mechanical Analysis

Dynamic mechanical analysis (DMA) was performed on a Mettler Toledo DMA/SDTA861e. Samples were cut into rectangular bars 30 mm long, 3 mm wide, and between 0.5 and 1 mm thick. Samples were inserted at room temperature and cooled to -50 °C. The sample was then heated to 100 °C at a rate of 2 °C min^{-1} while undergoing deformation at 1 Hz. The deformation was force limited to 5 N and deformation limited to 0.2% strain with a 300% offset.

5.2.7 Rheometry

Rheometry was performed on a TA Instruments DHR-3 with a Peltier heating plate. The neat polymer was melted and tested for viscosity at a constant shear rate of 30 s^{-1} between 160 °C and 180 °C.

5.2.8 Thermogravimetric Analysis

Thermogravimetric analysis (TGA) was performed on a Mettler Toledo TGA/DSC 1. Approximately 10 mg of polymer was placed into a 40 μL alumina crucible. The sample was heated under nitrogen flow from 25 °C to 700 °C at 10 °C min^{-1}.

5.2.9 Filament Extrusion

Filaments suitable for 3D printing were produced by extrusion through a Malvern Rosand RH-7 capillary rheometer with a 3 mm die. The 1 cm in diameter capillary column was filled and packed with 30 g of ground polymer. The chamber was heated to 170 °C over 30 minutes before compressing the column to a constant pressure of 12 MPa. As the extruded material exited the die opening, it was manually collected and held to the appropriate tension to retain a diameter near 2.85 mm across its length. Each column produced approximately 2 m of useable filament.

5.2.10 3D Printing

Test samples were printed using a stock Lulzbot Taz 6 with the Flexystruder V2 printing head, which is designed to guide flexible filaments to the nozzle. Test samples for dog bones consisted of vertical sheets 1 mm thick, 70 mm wide, and 70 mm tall. For all prints the extruder

temperature was set to 205 °C, the print head rastering speed set to 5 mm s^{-1}, with 0.20 mm layer heights and 100% infill. The polyethyleneimine print bed was heated to 85 °C.

5.2.11 Uniaxial Tensile Testing

Tensile testing was performed on a Lloyd LR5k Plus with a Laserscan 200 extensometer. Printed or molded sheets 1 mm in thickness were cut into ASTM D638-V dog bones using a certified cutting die. Printed samples were cut so that the deformation direction was at 0° or 90° to the layer direction. Dog bones were strained until failure at a rate of 50 mm min^{-1}. At least five samples were tested for the bulk, 0°, and 90° orientations.

5.3 Results & Discussion

5.3.1 Polymer Synthesis & Characterization

The polythiourethane for study was synthesized from an equimolar ratio of two widely available dithiol and diisocyanate monomers, 2,2'-(ethylenedioxy)diethanethiol and hexamethylene diisocyanate. The reaction was completed within 30 minutes after addition of triethylamine catalyst in dimethylformamide under a dry nitrogen environment. After precipitation in water and drying the reaction was found to have gone to 99.97% yield. This is an excellent example of the benefits gained through use of thiol-isocyanate polymerizations. Reaction times are decreased in comparison to similar alcohol-isocyanate polymerizations. Additionally the reaction was completed using a simple tertiary amine catalyst, whereas polyurethane syntheses require expensive inorganic catalysts to minimize unwanted reaction byproducts.

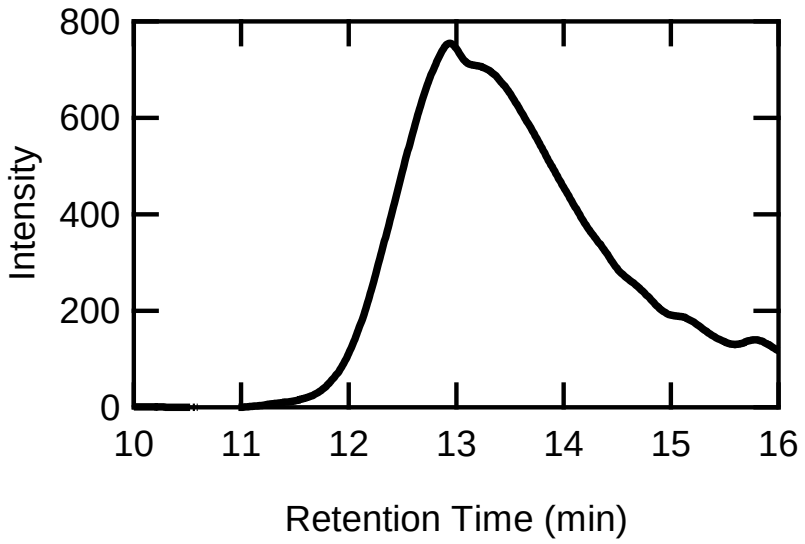

Figure 5.1. GPC trace of the thermoplastic poly(EDDT-HDI), with determined M_n 13411 g mol^{-1} and M_w 17222 g mol^{-1}.

The molecular weight was determined to be M_n = 14311 g mol^{-1} and M_w = 17222 g mol^{-1} by GPC (Figure 5.1). The dispersity index of 1.20 demonstrates that this reaction mechanism is capable of producing polymers with high uniformity under reaction conditions much more mild than what other chemistries require. Analysis via ^{1}H NMR (Figure 5.2) shows the peak shifts of the starting monomers and the final product. The spectrum agrees with the peak locations and integrations of the expected structure. The primary indicator of reaction success is the appearance of a signal at 8.1 ppm, which arises from the highly shielded secondary amine proton present in the thiourethane bond. This is supported by FTIR spectra showing absence of the strong isocyanate absorption peak between 2275 and 2250 cm^{-1} and the appearance of secondary amide/amine stretching peaks at 3360 cm^{-1} following curing (Figure 5.3). The speed and efficiency of the polymerization at this scale (430 g) shows that thiol-isocyanate polymerizations

may be effectively utilized to quickly produce large amounts of material without the need for complex reaction equipment and protocols.

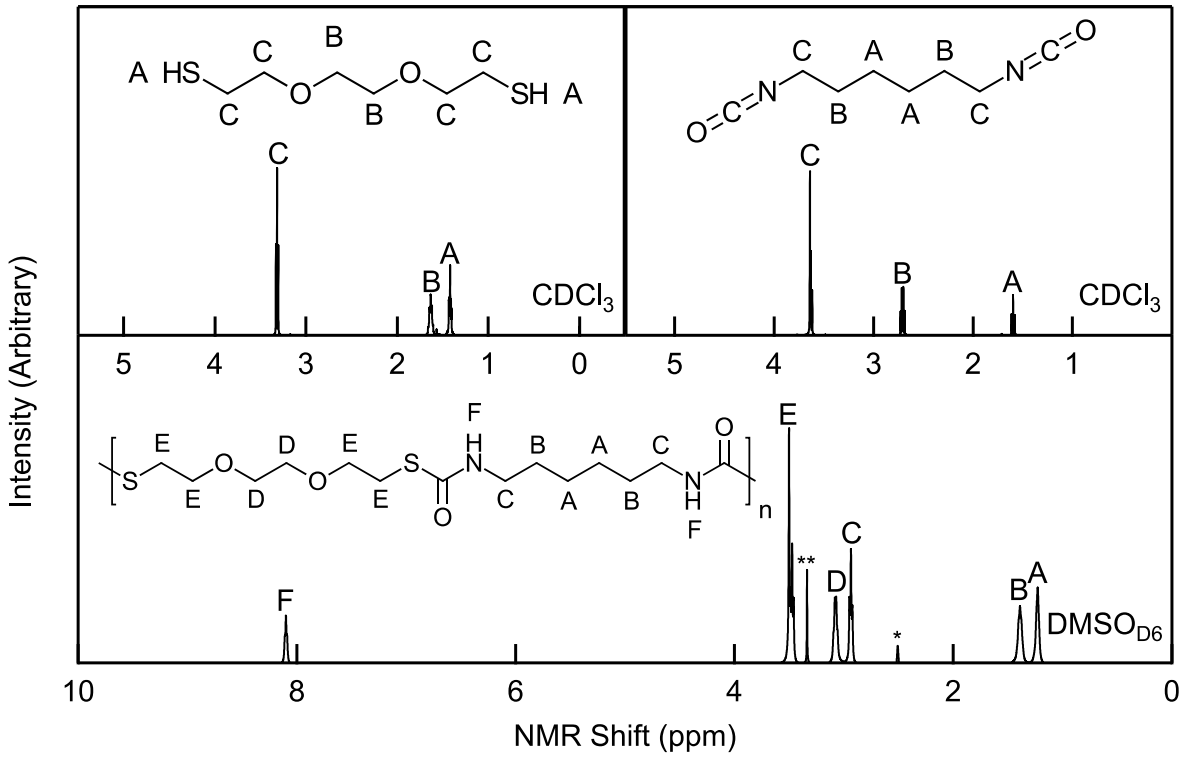

Figure 5.2. ^{1}H NMR spectrum of poly(EDDT-HDI) and its monomer units show the polymerization reaction produces the expected product. *Solvent peak **Water peak

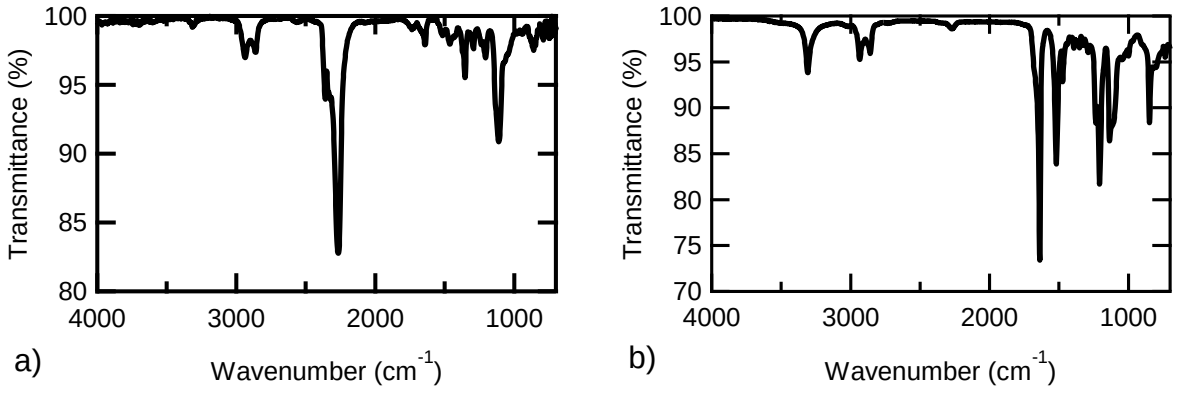

Figure 5.3. FTIR-ATR spectrum of (a) the EDDT-HDI pre-polymer resin prior to curing and (b) poly(EDDT-HDI) indicating presence of thiourethane bond and disappearance of thiol and isocyanate peaks

5.3.2 Thermal Properties

The thermomechanical properties of the synthesized polymer were studied via thermogravimetric analysis (TGA), differential scanning calorimetry (DSC), and dynamic mechanical analysis (DMA) to determine if the melt properties are suitable for 3D printing. DSC and DMA show a glass transition temperature (T_g) of approximately 10.5 °C with a crystal melt transition (T_m) at 110.5 °C (Figure 5.4 a, b). The melt onset occurs approximately 90 °C, giving an effective operating temperature range from sub-ambient temperatures to 90 °C. Within this range the material exhibits a storage modulus between 400 and 250 MPa.

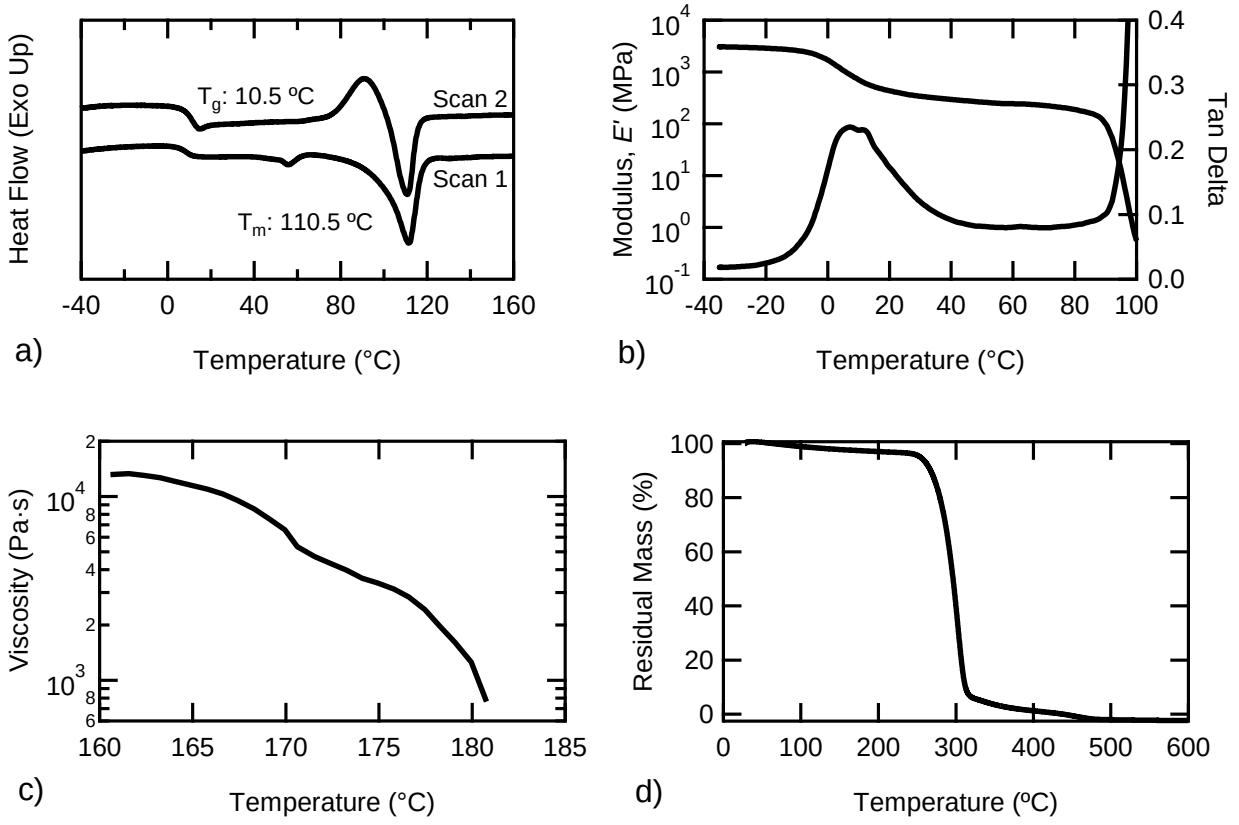

Figure 5.4. (a) Differential scanning calorimetry, (b) dynamic mechanical analysis, (c) rheology, and (d) thermogravimetric analysis of poly(EDDT-HDI) show glass transition, melt transition, flow behavior, and degradation.

Lower melting points are advantageous to 3D printing polymers, as print head temperatures commonly must be 50-60 °C higher than the melting point to allow for complete melting and adequately low melt viscosity. A melting point at 110 °C ensures that the required print temperature will not exceed what is possible with commercial print heads, as the melt viscosity decreases to a point suitable for extrusion into filaments at 170 °C and continues to decrease at higher temperatures (Figure 5.4c). The degradation onset via TGA is shown to be 260 °C (Figure 5.4d), providing a large thermal operating range between the melting and degradation points to obtain the optimal printing temperature.

5.3.3 Filament Processing & 3D Printing

Following determination of the thermal transitions, the material was either extruded into standard 2.85 mm thick filaments via a capillary rheometer or pressed into sheets at 170 °C. The filaments were printed into vertical 1 mm thick sheets using a Lulzbot Taz 6 with a Flexystruder V2 print head. The optimal printing temperature was found to be 205 °C as it provided the best surface finish, although prints were completed successfully at temperatures as high as 240 °C. 205 °C is the same temperature that is used to print the most commonly used poly(lactic acid) (PLA) filaments. This is relatively low in comparison to most mechanically robust 3D printing filaments, which have print temperatures as high as 280 °C. Higher performance polymers such as Nylon must be chemically modified to enable printing below 300 °C. Some specialty materials with processing temperatures suitable for 3D printing have been developed such as T-Lyne, a commercially available filament manufactured by Taulman. T-Lyne is composed of a poly(ethylene-co-zinc methacrylate) ionomer and can be printed at 230 °C. It was chosen as a comparison material due to its favorable combination of flexibility and stiffness, exhibiting much

higher durability than typically used PLA or acrylonitrile-butadiene-styrene filaments. In addition to printing test specimens, other objects such as a logo with raised lettering were easily fabricated (Figure 5.5).

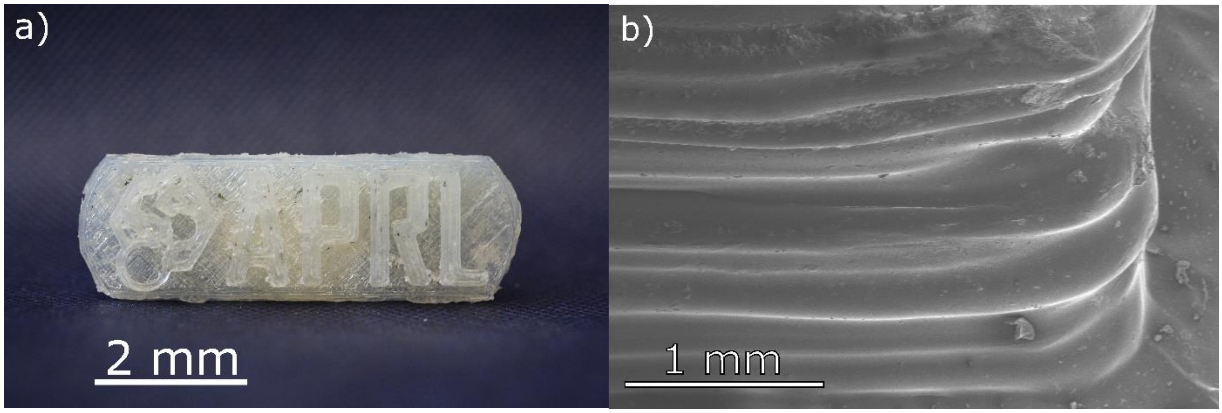

Figure 5.5. (a) 3D printed laboratory logo with raised lettering demonstrates the ability to print 3D objects. (b) Scanning electron microscopy of 3D printed polythiourethane parts.

3.4 Mechanical Testing

Dog bone samples underwent uniaxial tensile testing to determine the effects of printing in comparison to the toughness of the material in bulk and to observe variations in mechanical performance when the material is stressed in-line with the printed layers (0 °) or perpendicular to the layering (90°) (Figure 5.6). The tensile data shows highly comparable results to the commercial filament (Table 5.1). The bulk polythiourethane when pressed has mechanical performance surpassing that of the commercial material, with a yield stress of 26.2 MPa and undergoing failure at 308% strain and 48.3 MPa. In comparison, T-Lyne has a yield stress of 20.9 MPa and fails at 284% strain and 27.6 MPa. Both materials behave similarly when tested at the 0° orientation, in line with the print layer direction. The performance of the polythiourethane decreases when printed, but continues to perform well. The polythiourethane has a yield stress of

20.3 MPa, while T-Lyne has a yield stress of 18.1 MPa. There is substantial elongation prior to failure, with the polythiourethane breaking at 284% strain and 27.6 MPa and T-Lyne breaking at 269% strain and 24.8 MPa. While the 0° performance of the polythiourethane slightly improves upon the commercial filament, there is a larger difference in behavior when tested at 90°, perpendicular to the print axis. The polythiourethane filament fails at 7.3% strain and 21.5 MPa, which is near the yield point of the material when stressed in the 0° orientation. The commercial T-Lyne filament, however, experienced a higher loss in strength at 90°.

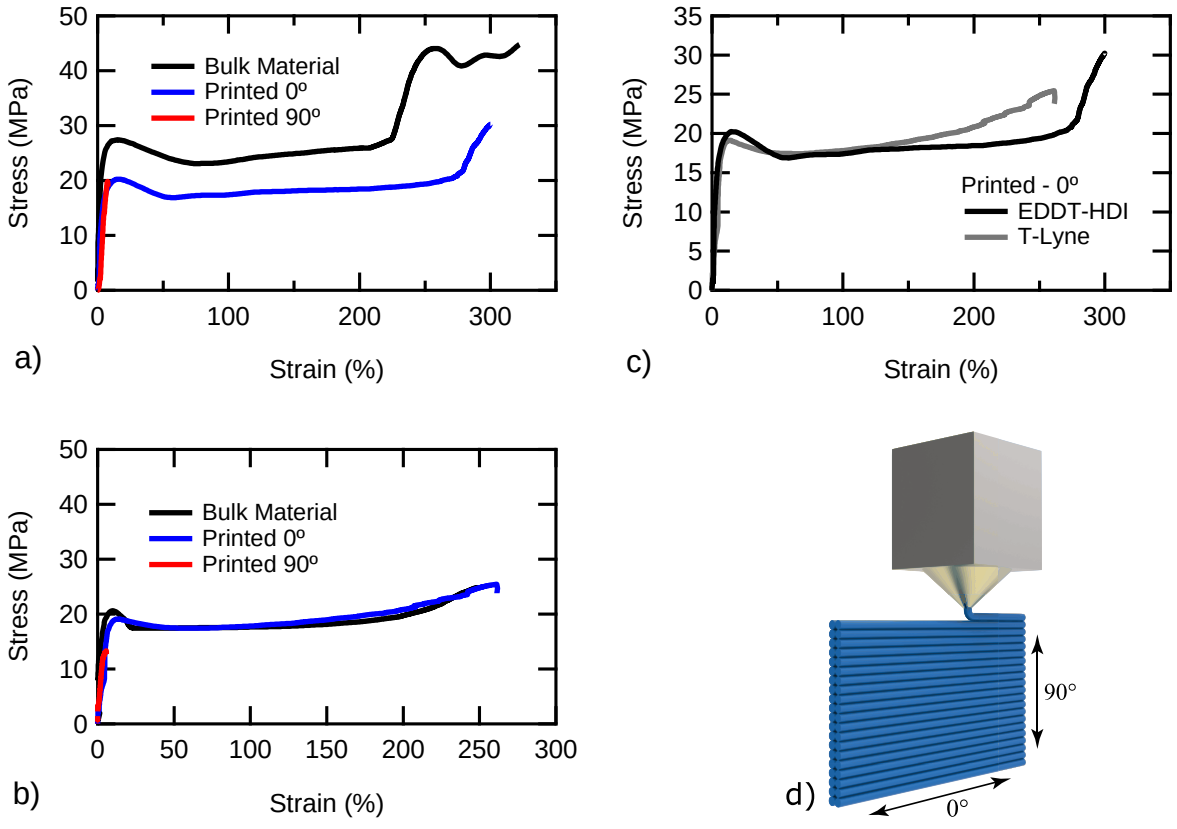

Figure 5.6. Tensile testing of (a)EDDT-HDI and (b)T-Lyne ionomer in bulk and printed at orientations parallel and perpendicular to the applied load. (c) Comparison of 0° orientation print performance of EDDT-HDI and T-Lyne shows comparable performance. (d) Schematic of FFF print head demonstrating the 0 ° and 90° orientations with relation to the raster direction.

It experienced failure at 4.7% strain and 11.6 MPa. This suggests that the commercial filament has poor layer adhesion properties, which are slightly improved in the polythiourethane. The lack of extension beyond the yield point is common within the FFF technique due to little mixing between printed layers. While the polythiourethane material still is not able to extend beyond the yield point in the 90° orientation, its ability to fail at the full yield stress of the 0° oriented parts is a substantial improvement over the performance of T-Lyne, which retains only 55% of its strength at 90°. The exact cause of this improved performance is under investigation, although it may be linked to forces such as hydrogen bonding between the thiourethane linkages increasing the degree of mixing between layers while material is being deposited.

The toughness of the materials, taken as the integrated area of the stress-strain curve, highlights the potential of the polythiourethane thermoplastics. Both polymers printed in the 0° orientation have similar toughness at 52.87 ± 3.66 MJ m^{-3} for the polythiourethane and 50.62 ± 5.45 MJ m^{-3} for T-Lyne. The improved layer adhesion of the polythiourethane compared to T-Lyne is also shown in the toughness data, with respective values of 0.54 ± 0.21 MJ m^{-3} and 0.31 ± 0.19 MJ m^{-3}. While low compared to the in-line toughness, the polythiourethane does indeed outperform the commercial material. The most interesting result is the toughness in bulk. T-Lyne has clearly been optimized for printing and has 0° performance matching its bulk properties. On the other hand, the bulk polythiourethane has a toughness of 91.95 ± 19.39, significantly higher than T-Lyne in any form and above what was achieved when printed. These results are quite encouraging, showing mechanical performance surpassing that of a high performance commercial filament. It is possible that further refinement of the filament extrusion and printing parameters may allow the 0° behavior to more closely match that of the bulk material.

Table 5.1. Mechanical behavior of polythiourethane and commercial filaments in uniaxial tension

Material	Orientation	Yield Stress (MPa)	Ultimate Tensile Strength (MPa)	Elongation at Failure (%)	Toughness (MJ m^{-3})
EDDT-HDI	Bulk	26.20 ± 1.05	48.30 ± 7.08	307.80 ± 40.29	91.95 ± 19.39
	0°	20.36 ± 0.13	27.56 ± 2.69	284.19 ± 15.58	52.87 ± 3.66
	90°	NA	21.48 ± 1.95	7.26 ± 0.96	0.54 ± 0.21
T-Lyne	Bulk	20.90 ± 0.41	27.77 ± 1.51	264.18 ± 16.41	49.26 ± 3.63
	0°	18.07 ± 0.80	24.76 ± 2.09	268.98 ± 18.78	50.62 ± 5.45
	90°	NA	11.55 ± 1.59	4.73 ± 1.56	0.31 ± 0.19

5.3.4 Conclusions

In summary, thiol-isocyanate chemistry has been utilized to synthesize a tough polymer with thermal properties well-suited for fused filament fabrication using a simple and scalable synthetic approach. The wide availability of thiol and isocyanate monomers in addition to the ease and speed of performing the polymerization reaction demonstrates the viability of this approach on a large scale. The characteristic low melting point of the sulfur-containing polymer lends itself well to FFF techniques, allowing it to be printed at temperatures typically used in these systems. Nevertheless, the mechanical performance of the material surpasses that of commercially available high performance filaments in-line and against the printed layer direction. The polythiourethane retains its full yield strength when stressed against the print layer direction, while the commercial comparison material loses 45% of its strength. This is a substantial improvement over the current state of the art and bodes well for the nascent field of polymers with properties optimized for additive manufacturing techniques. Considering the rapid

growth of additive manufacturing as a whole, engineering materials to be compatible with these processes is likely to become a field of increased importance in the coming years. This is expected to be driven by increased industrial adoption of 3D printing processes and an increased demand for materials that meet their needs and expectations. We hope that the results presented in this work will help provide a strong foundation of knowledge for the future development of additive manufacturing materials, such as those with larger thermal operating ranges and self-healing chemistries to promote inter-layer adhesion.

CHAPTER 6

POLYTHIOURETHANE SUBSTRATES FOR DURABLE SOFTENING BIOELECTRONICS

6.1 Introduction

Bioelectronic devices, while effective in acute settings, experience a range of failure modes in a chronic environment. A growing body of evidence supports the theory that many of these failure modes are linked to the mechanics of the substrate. Stiff substrates such as those made from silicon or tungsten have been shown to produce heightened inflammation and eventual scarring around the device in comparison to soft substrates. On their own, soft substrates are difficult to implant but softening materials have shown to be a promising platform for bioelectronics due to easy implantation and improved *in vivo* response. Previously studied softening materials only exhibit modest changes in modulus, are difficult to fabricate complex electronics on, or are not mechanically robust and frequently break.

This work reports the use of photo-cured polythiourethanes that use the adaptability of thiol isocyanate chemistry to tune the glass transition temperature and crosslink density for improved softening and toughness over previously synthesized substrates. The materials are compatible with photolithographic processing, ethylene oxide sterilization and exhibit no cytotoxicity. Non-functional device are shown to reduce micromotion-induced stresses in cortical tissue in comparison to traditional silicon substrates. Functional devices are implanted into the cortex of a rat and used to record nerve firings.

6.2 Experimental Methods

6.2.1 Polymer Synthesis

Stoichiometric mixtures of trimethylolpropane tris(3-mercaptopropionate) (TMTMP), hexanedithiol (HDT), hexamethylene diisocyanate (HDI), and isophorone diisocyanate (IDI) were mixed with the 0.25 wt/wt% of the previously synthesized QAS-MTX until homogenous. The pre-polymer solution was injected between glass slides separated by 20 μm, 60 μm, or 500 μm spacers. The resins were cured for 30 minutes under 365 nm irradiation in a UVP CL-1000L ultraviolet crosslinker prior to undergoing a thermal post-cure at 100 °C for at least one hour.

6.2.2 Thermogravimetric Analysis

Thermogravimetric analysis was performed on a Mettler Toledo TGA/DSC 1. Samples were cut into circular disks approximately 3 mm in diameter and 500 μm thick and placed in 70 μL alumina crucibles. The samples were heated from 25 °C to 700 °C at 10 °C min^{-1} under nitrogen flow. The thermal degradation onset was determined using the Mettler Toledo STARe Thermal Analysis Suite. At least three samples were tested for each polymer composition.

6.2.3 Differential Scanning Calorimetry

Differential scanning calorimetry was performed on a Mettler Toledo DSC1/700. Samples were cut into circular disks 3 mm in diameter and 500 μm thick and placed in 40 μL aluminum crucibles. Dry samples were inserted at 50 °C and cooled to -50 °C before undergoing three heating and cooling cycles between -50 °C and 150 °C. The second and third cycles were used to determine polymer T_g. Wet samples were inserted at 25 °C and cooled to 0 °C before heating to

100 °C. Only one cycle was performed as subsequent cycles would result in dehydration of the sample. All heating rates were 10 °C min^{-1}. Glass transition temperature was determined using the Mettler Toledo STARe Thermal Analysis Suite. At least three samples were tested for each polymer composition.

6.2.4 Dynamic Mechanical Analysis

Dynamic mechanical analysis (DMA) was performed using a TA RSA-G2. Samples were cut into rectangular sheets 40 mm long, 4 mm wide, and 60 μm thick. Samples were loaded in tension with a gage length of 15 mm, preload force of 0.05 N, oscillation frequency of 1 Hz, and deformation amplitude of 0.275% strain. Dry experiments were run from 10 °C to 100 °C with a heating rate of 2 °C min^{-1}. Soaking experiments were run using the immersion system of the RSA-G2 filled with 1X phosphate buffered saline solution. Samples were heated from room temperature to 37 °C followed by isothermal oscillation for 60 minutes. Samples were then cooled to 10 °C at 3 °C min^{-1} followed by heating from 10 °C to 80 °C at 2 °C min^{-1}. All specimens were tested in triplicate.

6.2.5 Swelling & Degradation

Samples were cut into disks approximately 3 mm in diameter and 500 μm thick. The disks were individually massed and submerged in individual well plates with phosphate buffered saline solution. Samples soaked at 37 °C for 1, 4, 7, 14, or 28 days prior to testing. On each of these days, 3 disks of each composition were removed and patted dry before being massed to determine the degree of swelling. The samples were then dried under vacuum at 125 °C for at least 12 hours before being massed once more to determine the degree of degradation.

6.2.6 Tensile Testing

Uniaxial tensile testing (UTM) was performed on a Lloyd LR5k Plus fitted with a 100 N load cell, a Laserscan 200 extensometer, and temperature controlled chamber. Polymer sheets 100 μm thick were cut into dog bones using a certified ASTM D638-V cutting die and tested according to the standard procedure. Wet samples were soaked in phosphate buffered saline solution for 3 days at 37 °C prior to testing. All tests were conducted at 37 °C.

6.2.7 Cytotoxicity Analysis

Cytotoxicity assays based on material extracts were carried out in accordance with International Organization for Standards (ISO) protocol "10993-5: Biological evaluation of medical devices". Here, substrate formulations were tested against positive and negative controls (Tygon-F-4040-Lubricant Tubing and complete cell medium, respectively) in order to determine normalized cell viability percentage. Extract treatments that resulted in viability percentages less than 70% were considered evidence of material cytotoxicity.

Briefly, NCTC clone 929 fibroblasts (ATCC, USA) were seeded in a polystyrene 24 well plate at a density of 8,000 cells/well and incubated for 48 hours at 5% CO2, 95% relative humidity, and 37 ˚C in complete cell medium (EMEM supplemented with 10% horse serum) to allow for adhesion and proliferation. Material extracts were produced by separately incubating sterilized samples of SMP (5.5 cm x 4.5 mm x 24 μm) and positive control materials (OD: 0.794 cm, ID: 0.476 cm, 0.6 cm in length) in individual wells containing 1.65 mL of complete cell medium at 37 ˚C for 24 hours. Following incubation, cell medium was either exchanged for material extract

medium (50/100%) or fresh medium in the case of negative controls. Cells were then incubated for an additional 24 hours prior to live/dead assays.

Live/dead cell staining was carried out using a LIVE/DEAD Cytotoxicity Kit for mammalian cells (Thermo Fisher, L3324). Briefly, cells were washed 3x in PBS and incubated in complete cell medium containing 2 µM Calcein AM (CaAM) and 4 µM Ethidium Homodimer (EthD-1) at 37 ˚C for 10 min. CaAM and EthD-1 dyes selectively stain the cytoplasm of live cells and the nucleus of apoptotic cells, respectively. Epifluorescence images (n=4 fields of view per well) were collected on an inverted microscope (Nikon Ti eclipse) using a 10x objective. Live/dead cell counts were carried out using ImageJ (NIH) software. Cell viability percentage was defined as the ratio of CaAM-labeled cells to the total number of cells. The reported percentages were normalized to those calculated for negative control wells. Reported error bars represent standard deviations.

6.2.8 Device Fabrication

Bioelectronic devices were fabricated by curing the pre-polymer solution between glass slides separated by 30 µm foil spacers. One slide was coated with a 400 nm layer of gold prior to curing, the other was cleaned by successive washings with acetone and isopropanol. The samples were cured for 30 minutes under 365 nm irradiation in a UVP CL-1000L ultraviolet crosslinker and post-cured at 100 °C for at least two hours. Following post-cure, the slides were separated leaving the polymer substrate adhered to the clean glass slide with the 400 nm layer of gold adhered to the surface. The gold was patterned using established photolithographic techniques. A 12 µm layer of polymer was cast onto the surface of the device using 12 µm foil spacers using the same cure and post-cure procedure as described above. This layer was then etched and

titanium nitride electrodes were deposited on the surface using established photolithographic techniques. The device shape was then etched from the substrate using an oxygen plasma etch and hard mask. An Omnetics connector was attached to devices via soldering before the completed devices were removed from the underlying glass by soaking in DI water and manual extraction.

6.2.9 Sterilization

Sterilization specimens and devices were mounted onto glass dishes and packed into a liner bag with gas indicator tape and biological indicators. The packed samples were loaded into an Anderson Products Anprolene AN74i ethylene oxide (EtO) sterilizer. A Humidichip was included to ensure at least 35% relative humidity inside the liner bag. After at least 4 hours of pre-humidification, a glass ampule containing 18 g of liquid EtO was added to the liner bag, which was then sealed. Sterilization occurred at room temperature and atmospheric pressure for 24 hours, followed by 2 hours of purging and aeration. The samples were retrieved and the indicators checked to confirm sterilization. The samples were then de-gassed for 72 h under vacuum at 37 °C to remove trace amounts of EtO.

6.2.10 Micromotion Studies

Micromotion studies and analysis were performed using the same equipment and procedures as previously described by Sridharan et al. with minor adjustments to the insertion rates and depths. Single and dual-phase insertions were done manually with an insertion rate of 300 µm s^{-1} (*82*). In step-wise insertions, the 50 µm steps were done at 120 µm s^{-1}. The dual-phase insertion had a two minute recording period between phases, with 15 minutes of recording following full

insertion in both the single and dual-phase techniques. Step-wise insertion had a two minute recording period following the initial insertion, with one minute recordings between each subsequent insertion step.

6.2.11 Device Implantation & *In Vivo* Recording

Long-Evans rats are anesthetized using isoflurane vapor and placed in stereotaxic equipment. The rats are kept unconscious using low levels of isoflurane vapor and a series of small holes are drilled into the skull. The main hole is the probe insertion location, with the minor holes used to fix the probe to the skull. The probe is manually inserted into the brain at a rate of approximately 300 μm s^{-1} to a depth of 2 mm. Silicone and dental cement are used to make a skull cap surrounding the implant and open wound. Pain and discomfort are minimized before and after surgery through the application of topical and injected analgesics.

Following the operation, the device is connected to a Plexon Ominplex Neural Data Acquisition system and the animal allowed to regain consciousness. Electrical signals are then recorded for ten minutes while the animal is fully awake and behaving freely. Subsequent measurements are taken three days and two weeks following implantation. Raw data is processed using the Plexon Omniplex software.

6.3 Results

6.3.1 Substrate Formulation

An effective substrate for implantation must remain rigid while being inserted into neural tissue prior to softening to match the modulus of the tissue. The stiffness of the substrate is most

dependent on the glass transition temperature and the crosslink density, which are independently controlled by varying the TMTMP-HDT and HDI-IDI ratios (Figure 6.1). The crosslink density was determined by the ratio of TMTMP and HDT added to the sample, as the three functional groups present on the TMTMP molecule would act to crosslink the material and the di-functional HDT would act as a chain extender. Increasing amounts of TMTMP would increase the crosslink density, therefore increasing the rubbery modulus. The glass transition of the substrate was tuned by adjusting the ratio of hexamethylene diisocyanate and isophorone diisocyanate. A substrate with the more flexible HDI would exhibit a lower glass transition than a sample containing the rigid IDI monomer. By manipulating the amounts of TMTMP, HDT, HDI, and IDI, it is possible to independently control the degree of crosslinking and the glass transition temperature. The substrate formulations were determined by choosing a desired amount of crosslinker and adjusting the radio of HDI and IDI until the glass transition temperature was tuned to the target temperature (Table 6.1).

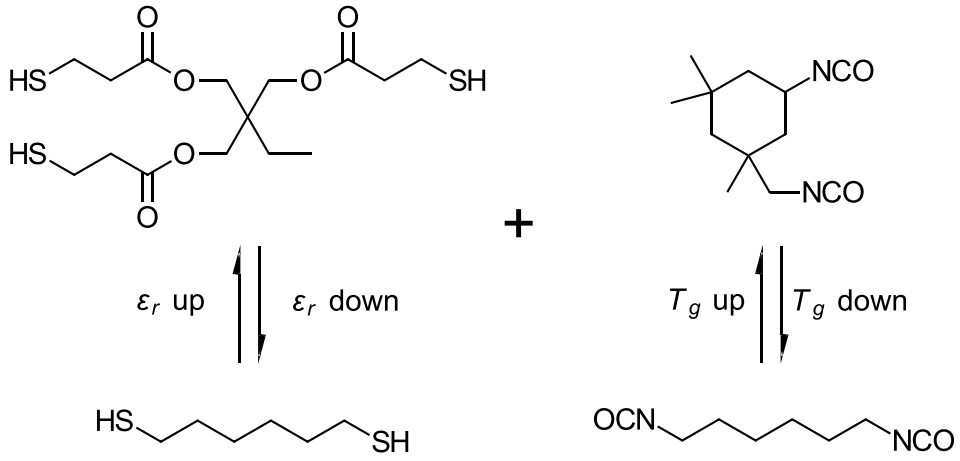

Figure 6.1. Rubbery modulus and glass transition temperature are controlled by adjusting the ratios of TMTMP to HDT and IDI to HDI, respectively.

Table 6.1. Thiourethane neural substrate formulations

Composition	Functional Group Percentage			
	TMTMP	HDT	HDI	IDI
TU-100	100	0	80	20
TU-100L	100	0	100	0
TU-100H	100	0	60	40
TU-50	50	50	80	20
TU-50L	50	50	100	0
TU-50H	50	50	60	40

6.3.2 Thermo-Mechanical Analysis

Control over glass transition temperature and rubbery modulus was confirmed via dynamic mechanical analysis. Changing the ratio of HDI to IDI alters the glass transition temperature (Figure 6.2). The TU-50L variant, containing only HDI as the diisocyanate chain extender, has a decreased glass transition temperature near 35 °C. TU-50H contains a 3:2 molar ratio of HDI to IDI, thus showing an increased glass transition temperature near 75 °C. Similarly, the rubbery modulus is adjusted via the ratio of TMTMP to HDT (Figure 6.3). TU-100L has a glass transition temperature similar to TU-50, but has a heightened rubbery modulus of 13 MPa due to a high loading of TMTMP. The TU-50 composition has a lower rubbery modulus of 7.5 MPa. TU-50 was chosen as the candidate substrate formulation due to having a decreased rubbery modulus and glass transition onset above physiological temperatures. The softening behavior of

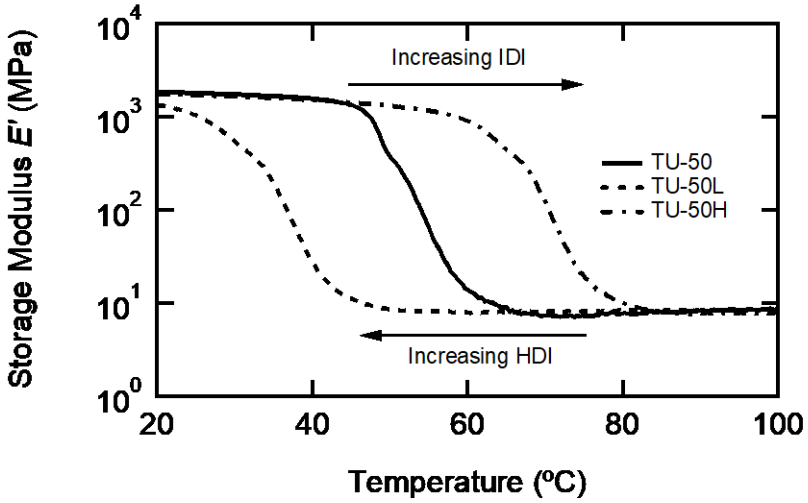

Figure 6.2. TU-50 with variants with differing HDI to IDI ratios demonstrate control over glass transition temperature, with transition points between 40 °C and 70 °C.

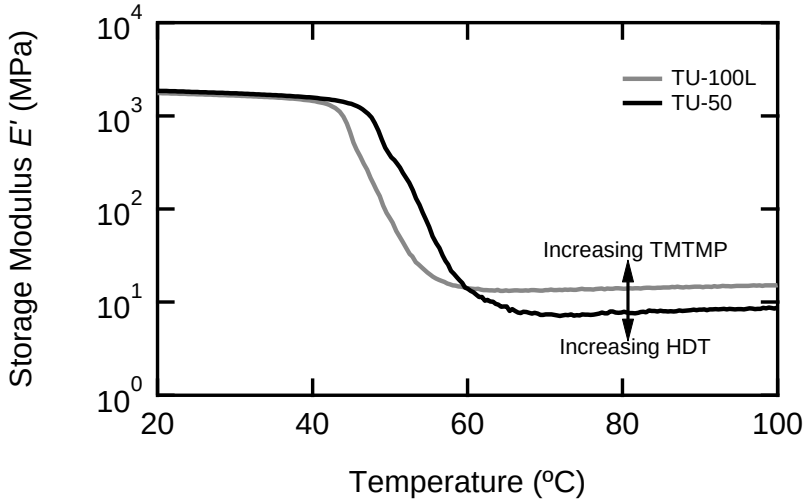

Figure 6.3. TU-50 and TU-100L show similar glass transition temperatures but different rubbery moduli, due to adjusting the ratio of TMTMP and HDT.

the material was further studied via dynamic mechanical analysis (Figure 6.4). When dry, the material has a modulus of 1600 MPa at physiological temperature, 37 °C. Upon soaking in phosphate buffered saline solution, the glass transition temperature experiences a downward shift of 25 °C. This results in a decreased modulus of 8.9 MPa at 37 °C.

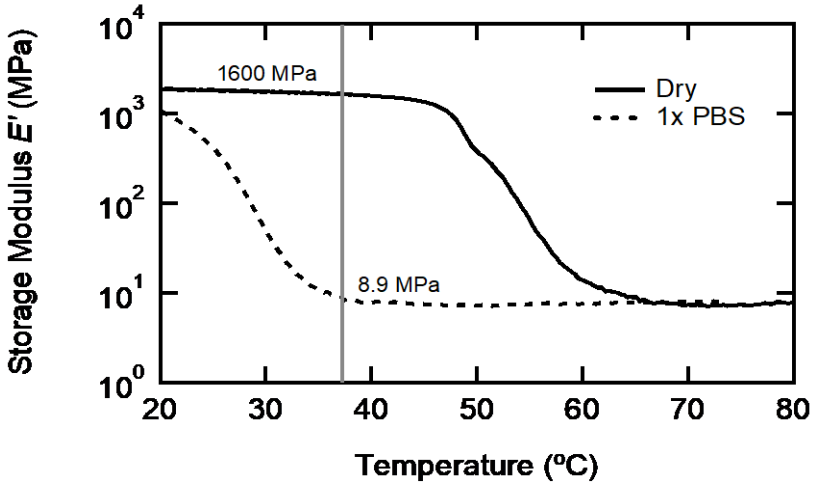

Figure 6.4. TU-50 shows a downward shift in glass transition temperature when soaked in phosphate buffered saline solution, manifesting as a decrease in modulus at 37 °C

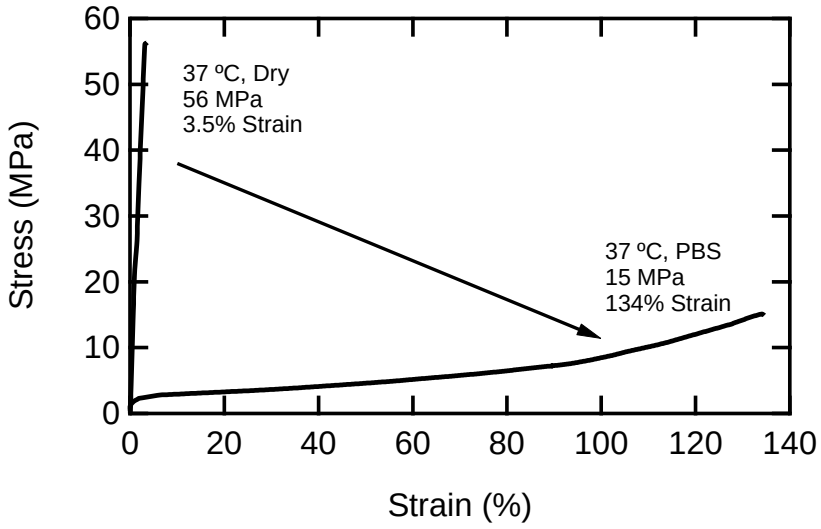

Figure 6.5. Dry tensile behavior of thiourethane neural substrate materials shows typical glassy behavior, but behaves as an elastomer after soaking in phosphate buffered saline

The softening behavior is reflected in the tensile performance of the substrate (Figure 6.5). In the dry state, TU-50 is a stiff material, straining only 3.5% before undergoing brittle failure at 56 MPa. In the wet state at 37 °C the material behaves as an elastomer, stretching over 130% before failing at 15 MPa. Deformation up to this point is largely recovered on unloading.

6.3.3 Biocompatibility & Sterilization

An understandable concern regarding the use of thiourethanes as bioelectronics substrates is the possibility of unreacted thiol or isocyanate monomer causing cell death once implanted. Cytotoxicity tests were performed according to ISO 10993-5 in order to assess the effect of the substrate or possibly unreacted monomers on cell viability (Figure 6.6). Polyurethanes have been used previously as implantable materials with little observed negative effects on the body. Unreacted isocyanates however are known toxins which can cause extensive cell inflammation and death upon excessive exposure.

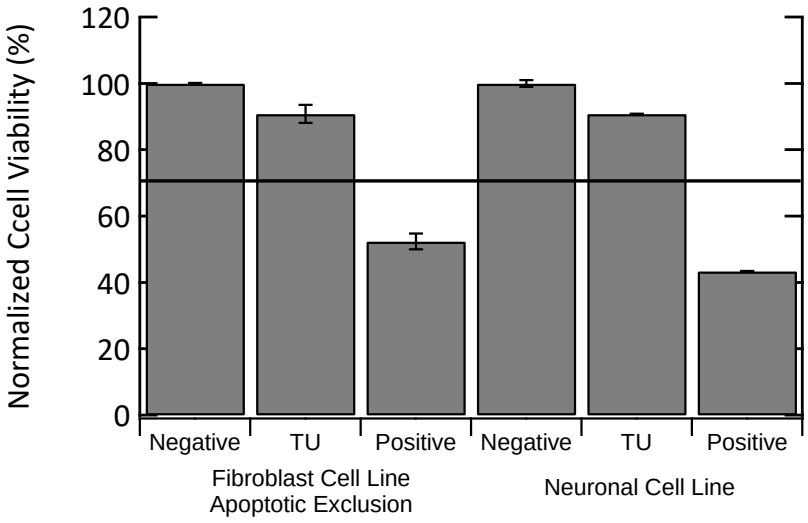

Figure 6.6. Cytotoxicity testing confirms that polythiourethane substrates do not have a significant impact on cell viability

The sample extract provided statistically equal cell viability to the negative control, while the positive (cytotoxic) control had only 40% cell viability compared to the negative. The toxicity

testing suggests that there are no remaining unreacted isocyanates that are available to cause significant cell death and that the substrate itself has little to no effect on cell viability.

Ethylene oxide is used to sterilize devices prior to implantation. While effective, ethylene oxide is known to have detrimental chemical effects on some polymers. Dynamic mechanical analysis was performed on ethylene oxide sterilized samples in order to observe any negative effects on the behavior (Figure 6.7). No change in thermo-mechanical behavior is seen between the neat and sterilized samples. The peak of tan delta remains near 59 °C and rubbery modulus remains at 8 MPa, indicating that no polymer breakdown occurred.

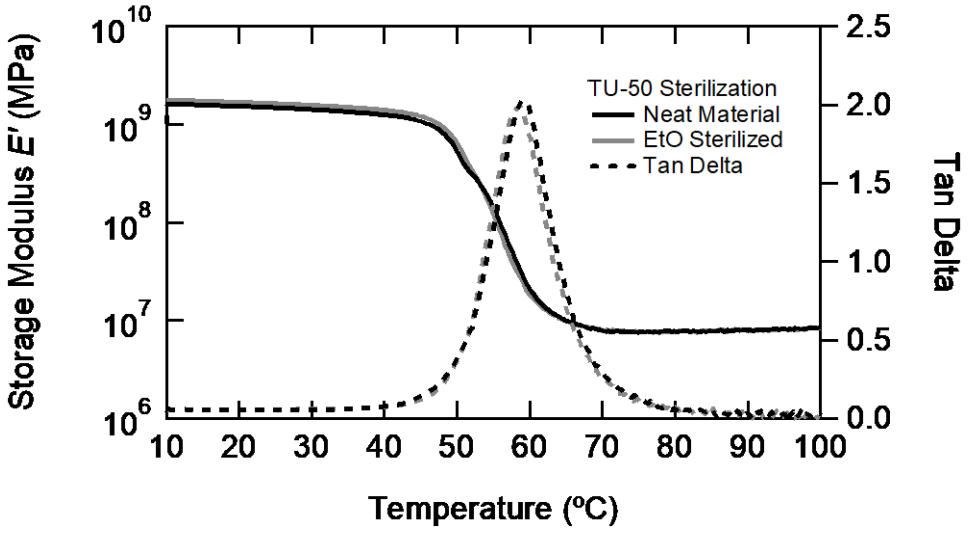

Figure 6.7. Dynamic mechanical analysis of TU-50 before and after ethylene oxide sterilization. No change in the modulus or peak of tan delta in the sterilized sample indicates that the sterilization protocol has no negative effects on substrate performance.

6.3.4 Micromotion Analysis

Micromotion levels surrounding a non-functional cortical implant were performed to assess the ability of the softening substrate to dampen movement that may damage the implant site. Single and dual phase implantations were performed with adequate time left following implantation for

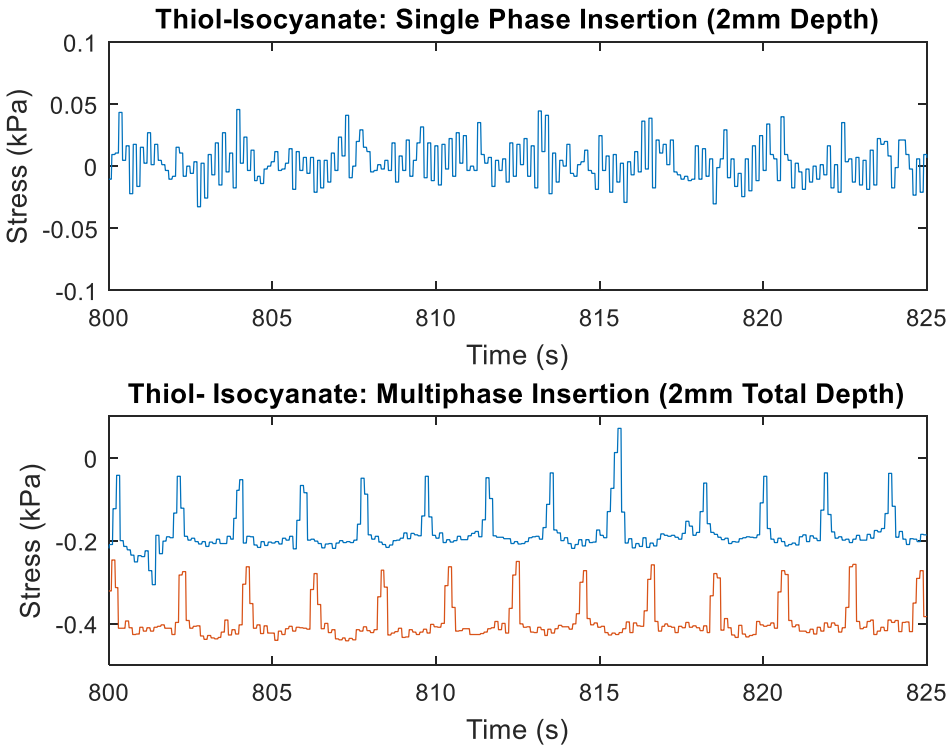

Figure 6.8. Single and dual-phase insertions of a thiourethane brain probe show steady state stresses no larger than 0.05 kPa in single phase, whereas dual-phase insertions show larger amplitude periodic stresses of up to 0.2 kPa.

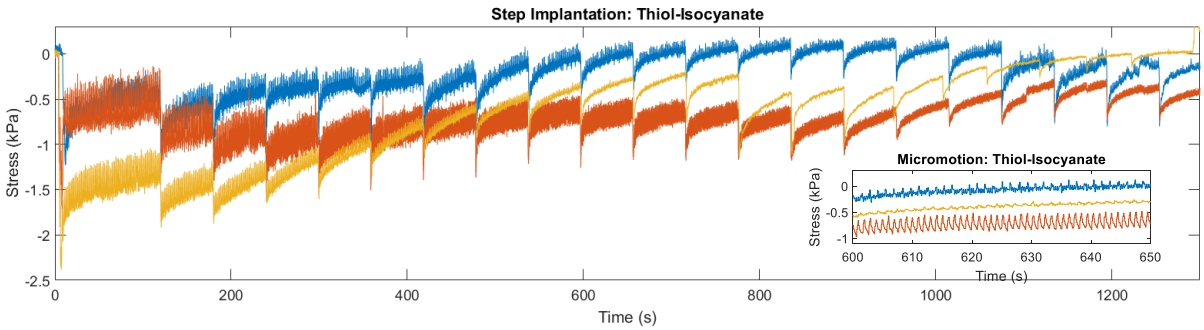

Figure 6.9. Multi-step insertion shows varying steady state behavior, with stress amplitudes as little as 0.1 kPa and as high as 0.4 kPa between samples

the micromotion to reach steady state behavior (Figure 6.8). The single phase insertion displays low levels of steady-state micromotion, with no detectable stresses surpassing 0.05 kPa. Dual-

phase insertions show different behavior. A larger periodic stress is seen with a typical amplitude of approximately 0.2 kPa once every two seconds.

However, the average noise level between periodic spikes is lower than in the single phase inserted devices, at about 0.02 kPa in amplitude. Step-wise insertions show variable behavior (Figure 6.9). Steady-state behavior is as low as 0.1 kPa or as high as 0.4 kPa, depending on the sample. Among all samples, the mean stress amplitude decreases as the sample is inserted into the brain.

6.3.5 Device Implantation & Recording

An intracortical probe based on the TU-50 substrate was manually implanted in a rat cortex to test the viability of fabricated devices. Recording of spontaneous neural activity of awake rats shows single unit action potentials immediately following implantation in two of sixteen

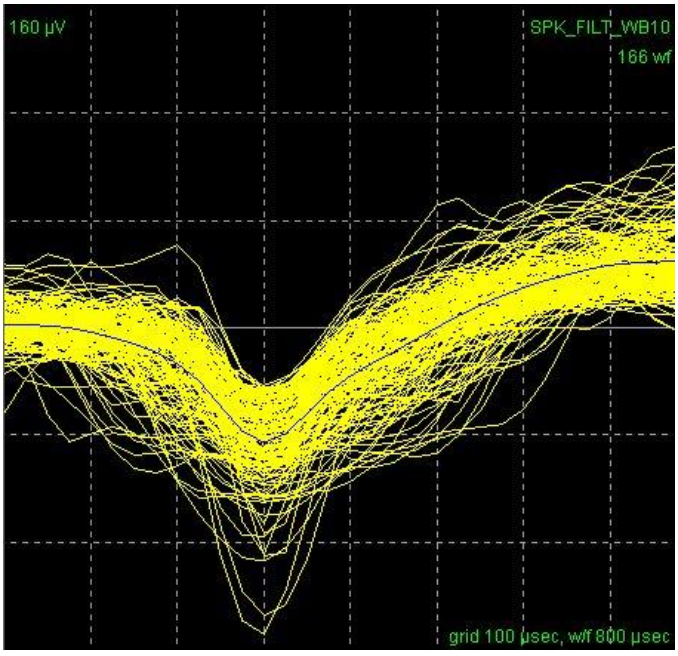

Figure 6.10. Single unit action potential immediately following implantation of the thiourethane-based intracortical probe.

recording channels, with one having an acceptable signal to noise ratio of 2.92 (Figure 6.10).Day-0 recording is typically not possible due to swelling, bleeding, and debris located around the implanted probe. Additional recordings have not been successfully completed at later stages of implantation. It is unclear at this point if the device has failed or if there are simply no active neurons within close proximity to one of the electrode sites.

6.4 Discussion

The results described in Section 5.3 offer encouraging evidence that polythiourethane substrates will offer improved softening, mechanical strength, and *in vivo* response over previously studied materials. Softening substrates currently in use only soften to a limited degree. For example, the substrates reported by Ware et al. are capable of softening to as low as 10 MPa but are unable to be implanted due to poor stiffness in the glassy state. Only semi-softening substrates which decrease to approximately 100 MPa in tension have the structural rigidity necessary for insertion into cortical tissue (*85*). In comparison, the thiourethane substrates described in this work have glassy moduli of 1600 MPa at physiological temperatures, but decrease to approximately 9 MPa following water uptake. The increased glassy modulus of the substrate can prevent excessive buckling prior to complete insertion and allow thinner devices to be fabricated, but the higher degree of softening will more closely match neural tissue. This may be enabled by increased levels up water uptake t in the thiourethane samples compared to thiol-ene substrates due to the heightened polarity of the thiourethane bond. This small but meaningful difference results in the thiourethane substrates having an over 25 °C shift in glass transition compared to approximately 20 °C in thiol-ene/acrylate materials. This enables the material to undergo a complete transition from glassy to rubbery following implantation.

The tensile results suggest that the substrates will have much-improved mechanical durability in comparison to the previously used thiol-ene/acrylate substrates. Thiol-ene networks are very brittle in the glassy state, leading to frequent failure of devices due to animal motion. The high crosslink density of thiol-enes also results in low failure strains in the rubbery state, causing more frequent tearing and subsequent failure. The thiourethane substrate has higher tensile durability than thiol-enes, especially in the rubbery state. This may reduce the occurrence of device failure via mechanical fracture, possibly enhancing average device lifespan. Cytotoxicity analysis and sterilization compatibility suggests that fabricated devices may be implanted without immediate detrimental effects on the surrounding tissue. Knowing this, we were able to move forward to processing devices via photolithography to study the *in vivo* response and recording viability. The first *in vivo* study examines the level of micromotion-induced stress surrounding the implant when in cortical tissue. Evidence thus far suggests that micromotion-induced stresses and strains in the brain tissue surrounding an implant may be one of the driving factors behind scarring, encapsulation, and eventual device failure. Rigid substrates such as those made from silicon show high levels of micromotion-induced stress, with typical amplitudes in the range of 0.2-0.3 kPa. Softening nanocomposites have shown slightly decreased stresses, typically near 0.15 kPa in amplitude. The thiourethane substrates have noticeably decreased levels of micromotion-induced stress, with stress amplitudes no larger than 0.05 kPa in the single phase-inserted samples. Dual-phase insertions show more interesting results, with large periodic stresses of approximately 0.2 kPa approximately every two seconds. However, there is minimal observable micromotion in between the periodic spikes, with amplitudes no larger than 0.05 kPa. The periodic behavior seems related to the breathing

behavior of the animal, but it is unclear at this time whether the periodic increases will contribute towards an increased glial response. There is a high degree of variability in the steady state behavior of the step-wise inserted probes, although they all remain below the stress levels seen with rigid substrates. All results show that the softening substrate produces fewer micromotion-induced stresses within the brain in comparison to rigid materials, and previous studies suggest that this should translate to decreased levels of scarring and foreign-body response. Initial implantation data is encouraging, with intracortical probes successfully recording neural activity in rats immediately following implantation. Subsequent recording sessions have not produced additional data, but the cause is unclear at this time. Electrode impedance measurements suggest that the device itself is in good condition. Therefore, lack of successful recordings may be due to factors such as glial encapsulation, tissue death, or simply bad luck. A larger sample size is necessary to determine the true effectiveness of the thiourethane-based devices.

6.5 Conclusion

Softening substrates for bioelectronics were synthesized using photo-cured polythiourethanes. The glass transition temperature and rubbery modulus may be controlled by varying the rigidity of the chain extending monomers and the amount of crosslinking monomer, respectively. The substrates undergo a 27 °C downward shift in glass transition temperature following exposure to physiological conditions, decreasing the modulus from 1600 MPa prior to implantation to approximately 9 MPa post implantation. Tensile data suggests that the substrates will resist mechanical failure at both the implantation site and at rigid connectors. The substrates do not exhibit cytotoxic behavior, and are compatible with ethylene oxide sterilization protocols. The substrates are compatible with microelectronic fabrication techniques, allowing functioning

intracortical probes to be fabricated. *In vivo* testing shows decreased micromotion induced stresses in comparison to rigid substrates, and apparent nerve firings recorded immediately following implantation in a rat cortex. Further studies will examine the long-term recording ability of devices on the substrate and refine the device fabrication process for improved yield and control.

CHAPTER 7

HIGH-PERMITTIVITY DIELECTRIC ELASTOMER ACTUATORS VIA THIOL-ISOCYANATE CLICK CHEMISTRY

7.1 Introduction

Dielectric elastomer materials must be soft, highly elastic, and have a high dielectric constant in order to actuate well at low voltages. Currently used materials do not achieve these properties well. Much of the potential impact for dielectric elastomers is limited due to the high driving voltages necessary for operation. This is due to the low dielectric constants of the acrylic and silicone-based materials most commonly used. Materials with higher dielectric constants have been synthesized through the use of filler materials, but these often compromise the mechanical properties or breakdown strength. Limited research in new chemistries have been done, but results have not yet provided large-scale improvements in performance.

This work aims to use thiol-isocyanate chemistry to produce soft, elastic polymers with high dielectric constants. The versatility of thiol-click chemistries and high polarity of the thiourethane bond suggests that these materials may effectively mitigate some of the drawbacks currently experienced by acrylic or silicone-based systems.

7.2 Experimental Methods

7.2.1 Synthesis of DEA Films

Elastomer films for thermomechanical and dielectric testing were produced by mixing stoichiometrically equivalent amounts of EDDT, TMTMP, HDI, and TMHDI in a 20 mL glass

vial with 0.25 wt% of the photo-catalyst QAS-MTX. The solution was then injected between glass slides separated by 100 μm or 500 μm spacers and cured under 365 nm irradiation in a UVP CL-1000L for at least 30 minutes.

7.2.2 Differential Scanning Calorimetry

Differential scanning calorimetry was performed on a Mettler Toledo DSC1/700 in 40 μL aluminum crucibles. Samples were cut into pucks approximately 4 mm in diameter and 0.5 mm in thickness. The samples were inserted at 50 °C, then cooled to -50 °C and heated to 100 °C three times to eliminate thermal history, measure, and confirm the result. All heating rates were 10 °C min^{-1}. Glass transition temperatures were determined via the Mettler Toledo STARe Thermal Analysis Suite. All samples were tested in triplicate.

7.2.3 Dynamic Mechanical Analysis

Dynamic mechanical analysis was performed on a Mettler Toledo DMA/SDTA861e. Samples approximately 25 mm long, 3 mm wide, and 0.5 mm thick were loaded into the large tension assembly with a 10.5 mm gage length. The samples were cooled to -50 °C or -90 °C and heated to 50 °C while undergoing oscillation at 1 Hz. The force amplitude limit was 5 N, the displacement amplitude limit was 21 μm, and the offset was 300%. All samples were tested in triplicate.

7.2.4 Dielectric Testing

Samples were cured or placed between glass slides coated with circular gold electrodes separated by 100 μm spacers. The electrodes were connected to an HP 4284 LCR meter. The capacitance

and dielectric loss was recorded using 1 V excitation at frequencies between 20 Hz and 1 MHz. The dielectric constant was recorded from the capacitance, electrode area, and film thickness according to the formula shown below.

$$\varepsilon_r = \frac{Cd}{\varepsilon_o A} \tag{1}$$

7.2.5 Actuation Testing

Actuation samples were cast as films approximately 12 cm long, 10 cm wide, and 100 μm thick. Samples were biaxially stretched 100% and fitted on a circular frame. Graphite nanoparticles were applied as compliant electrodes. The actuation area was a circle in the center of the sample approximately 2 cm in diameter. A high voltage power supply was connected to the electrodes. The voltage was increased from 0 V until breakdown occurred at 200 V increments. The sample was allowed to equilibrate at each voltage for one minute. The actuation was captured on a DSLR camera and the actuation was calculated using ImageJ.

7.3 Results

7.3.1 Elastomer Formulation & Thermo-Mechanical Characterization

The dielectric elastomer was formulated to have a glass transition temperature sufficiently low to ensure that the material is fully elastic at 20 °C. It uses a minimal amount of TMTMP to crosslink the material, as a higher degree of crosslinking would result in both increased modulus and T_g which are undesired effects. A 50:50 molar ratio of HDI and TMHDI was used as the isocyanate monomer to prevent crystallization as previously described in Chapter 4.

Differential scanning calorimetry was first performed to demonstrate sub-ambient glass transition temperatures and non-crystalline behavior (Figure 7.1). The thiourethane elastomer, has a glass transition temperature midpoint of 13.3 °C, which is near room temperature. No crystal melt transitions are seen in the material, as it is fully amorphous.

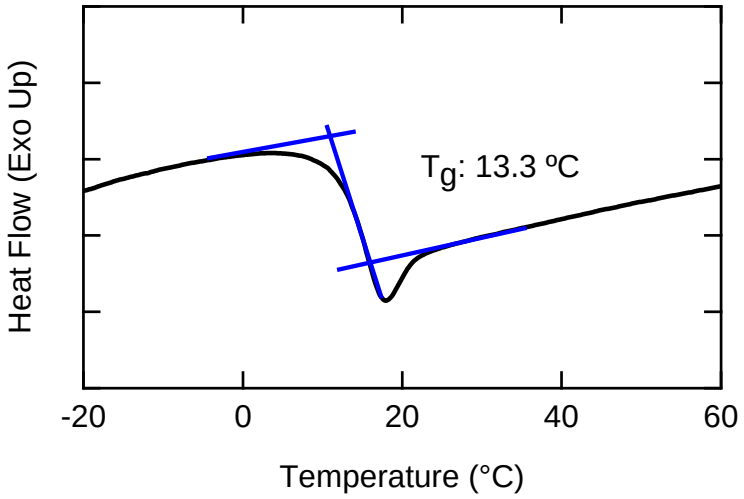

Figure 7.1. Differential scanning calorimetry shows sub-ambient glass transition temperatures of DEA films

Dynamic mechanical analysis confirms the glass transition measurements via DSC and illustrates the variation in modulus as a function of formulation (Figure 7.2). Glass transition temperature by DMA is measured by the peak of tan delta, with the thiourethane elastomer at 15.6 °C. The tan delta has a full-width-half-max of only 8 °C, indicating very high network uniformity. The rubbery modulus of the thiourethane at 20 °C is 8.2 MPa and not yet through the entire glass transition. The rubbery modulus further decreases further to 3.38 MPa at 40 °C. Uniaxial tensile testing was performed in order to assess the Young's modulus and failure strain of the elastomers (Figure 7.3). The thiourethane elastomer demonstrates hyperelastic behavior, with the effective modulus decreasing after the initial strain past 50%. The material continues to strain at

moderately low stresses until reaching 350%, where the stress begins increasing rapidly until failure at 18 MPa and 400% strain.

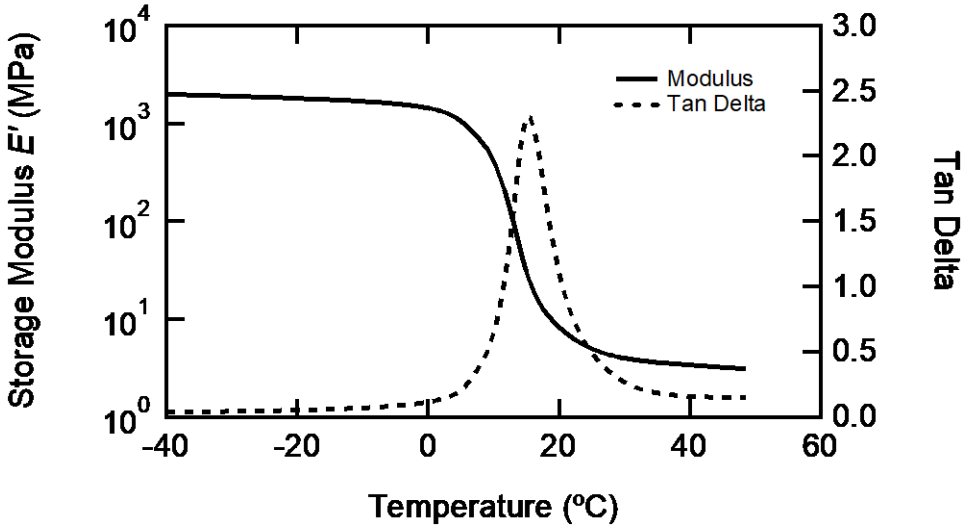

Figure 7.2. Dynamic mechanical analysis demonstrates that decreasing crosslink density lowers the glass transition temperature and rubbery modulus

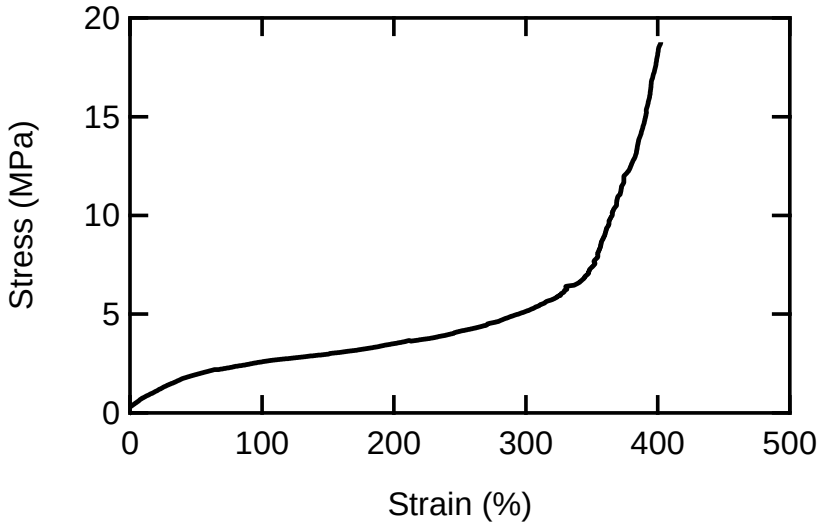

Figure 7.3. Uniaxial tensile testing shows decrease in Young's modulus and increase in failure stress as crosslink density is decreased

The relative permittivity was assessed via capacitance and loss measurement as a function of excitation frequency (Figure 7.4). The film displays dielectric performance highly dependent on

the excitation frequency. The elastomer has a relative permittivity of 11.5 at 20 Hz, which continuously decreases as the frequency increases to 6.5 at 1 kHz and 4.5 at 1 MHz. The greatest

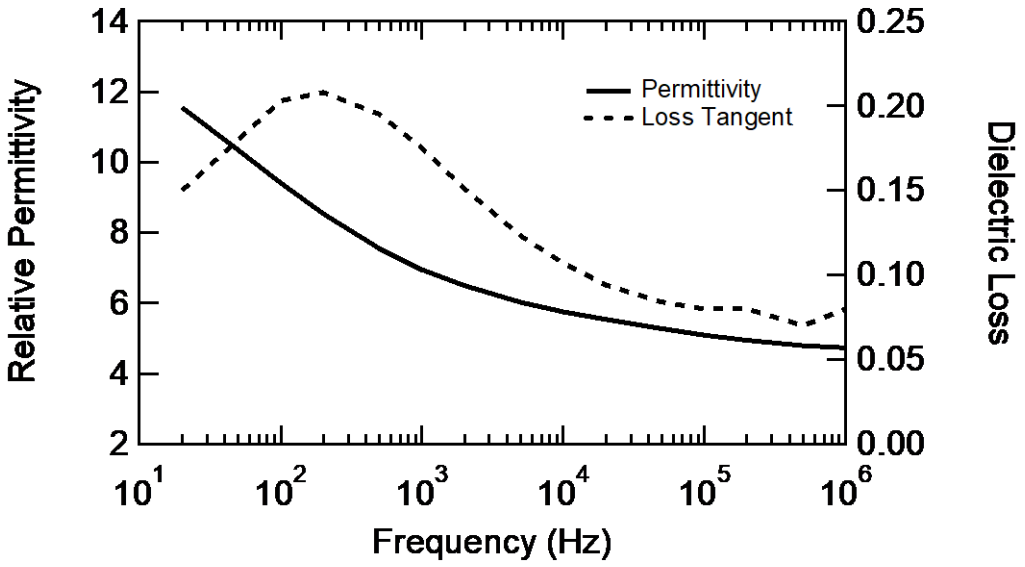

Figure 7.4. Polythiourethane films have high dielectric constants at low frequencies, gradually decreasing as frequency increases

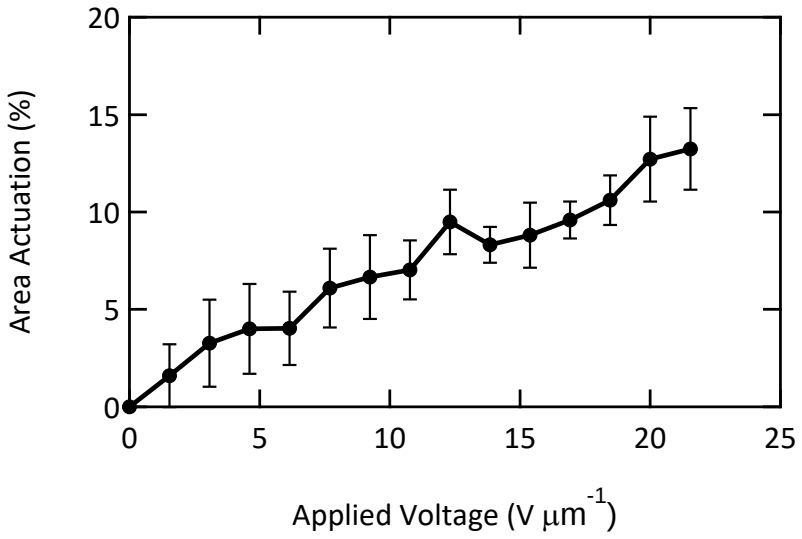

Figure 7.5. Actuation testing shows modest area changes in pre-strained films at low fields

change is seen between 20 Hz and 1 kHz, as is suggested by the dielectric loss. The dielectric loss begins at 0.15 at 20 Hz and peaks at 0.21 at 200 Hz. Following its peak, the loss dereases to approximately 0.08 at 1 MHz.

The actuation characteristics of the thiourethane film under 100% biaxial prestrain were investigated by applying a DC voltage to an active area of the film (Figure 7.5). Actuation shows a roughly linear trend, with the active area increasing in size by approximately 13% under a 20 V μm^{-1} applied field. Most samples experience dielectric failure when exposed to fields above this point.

7.4 Discussion

Results suggest that while the polythiourethane elastomer has improved dielectric properties in comparison to current materials, it falls short on other properties. The thiourethane network is stiff in comparison to VHB and silicones, which tend to have moduli in the hundreds of kPa. The dielectric performance of the thiourethane is good at low frequencies, with values more than double that of VHB and silicone materials. The high permittivity suggests that relatively high actuation at low voltages should be possible, but the increased stiffness in combination with low dielectric strength results in relatively low overall actuation of 13%. In comparison, VHB elastomers at low prestrains achieve 40% area actuation at 55 V μm^{-1}, and can have upwards of 300% actuation at over 100 V μm^{-1} using high levels of prestrain. Silicones with similar pre-stretching achieve area strains of 93% at 110 V μm^{-1}; very high fields.

It is unlikely that the thiourethane elastomers in its current form can achieve performance on-par with these materials. Even when far above the glass transition, the material remains an order of magnitude more stiff than the VHB and silicones. Furthermore, the increased permittivity of the

thiourethane does not fully account for the decreased dielectric strength, as the dielectric constant is increased by just over 2 times but the strength is reduced by four to five times. Performance increases gained by use of thiourethane chemistry do not outweigh the losses in performance elsewhere.

7.5 Conclusion

Thiourethane elastomer films have been synthesized through the photopolymerization of thiol and isocyanate monomers. These elastomers have glass transition temperatures below ambient levels, displaying elastomeric properties at room temperature. Dielectric constant is relatively high for a polymeric material at low excitation frequencies. Actuation up to 13% is achieved using 20 V μm^{-1} applied fields. Actuation underperforms in comparison to currently used materials such as VHB and silicones, despite the increased dielectric constant. This seem related to the high stiffness and a decreased breakdown strength of the elastomer in comparison to commonly used films. While it may be possible to decrease the elastomer stiffness, it would likely come at the cost of lowering the dielectric constant of the material. It is unlikely that the breakdown strength may be improved without compromising dielectric constant entirely. Thus, thiourethane elastomers do not, in their present form, make a strong basis for dielectric elastomer actuators.

CHAPTER 8

CONCLUSIONS AND FUTURE WORK

8.1 Conclusions

This goal of this work was to leverage the advantages inherent to thiol-isocyanate chemistry to address fundamental materials challenges in the additive manufacturing, bioelectronics, and electroactive polymer fields. Thiol-isocyanates have been under-utilized in comparison to other thiol systems due to processing difficulties related to the cure speed. Chapter 3 demonstrates that quaternary ammonium salt photo-bases may be synthesized which allow thiol-isocyanate resins to be processed in a manner similar to the more common free-radical based thiol-ene or acrylate systems. The photo-bases can be synthesized at scale, are stable in solution, and rapidly cure resins under irradiation at wavelengths up to visible light. Chapter 4 describes the development of a semi-crystalline thiol-isocyanate resin system in which the thermal and mechanical properties may be adjusted by tuning the crystallinity. In combination with the photo-bases described in Chapter 3, this constitutes a photopolymer system which has an order of magnitude increase in toughness and double the heat deflection temperatures of comparable acrylic materials used in the 3D printing field. 3D printing is demonstrated as a proof of concept using SLA techniques. A thermoplastic variant of this resin is extended to FFF-type printing in Chapter 5, showing performance matching a commercially available engineering grade filament. In Chapter 6, photocured thiol-isocyanates are used to implement a resin system for bioelectronics substrates that allows for independent control of the glass transition temperature and rubbery modulus. These substrates show increased softening and mechanical durability in comparison to previously used thiol-ene/acrylate softening substrates. This corresponds to improved

physiological responses *in vivo*, with minimal inflammation and scarring post-implantation. Functional intra-cortical neural probes are fabricated and used to record neuronal activity in rats. Chapter 7 shows that thiourethane elastomers have a heightened dielectric constant in comparison to other materials used for dielectric elastomer actuators. While overall performance still lags behind the state of the art materials, it may provide a basis for further ways to improve DEA performance. This work demonstrates that photo-cured thiol-isocyanate resins may have useful applications across a wide range of industries where current photo-cured polymer systems fall short.

8.2 Future Work

While the ability to use thiol-isocyanate photopolymers in 3D printing, bioelectronics, and soft actuator applications has been demonstrated, further work is necessary to achieve the full potential of these materials. The photo-bases shown in Chapter 3 are highly effective, but improvements to the synthetic procedure are likely necessary to reduce cost and improve yields if commercial scales are to be considered. The 3D printing resins demonstrated in Chapter 4 have vastly improved performance in comparison to the acrylic materials available today. However, challenges remain in the printing system itself. The SLA technique used to print the resin is both slow and wasteful, as the resin has a limited shelf life once the thiol and isocyanate components are mixed. Alternative printing techniques such as polymer jetting have been demonstrated, but further refinements to the resin and printing system would likely be needed to ensure reliability. Improvements to the photopolymer resins thermal operating range might be achieved through new combinations of monomers to both decrease the glass transition temperature and increase the crystal melt. New semi-crystalline resins based on aromatic structures are also a possibility.

These might have high stiffness, glass transition temperatures, and impact resistance similar to commercially available poly-aromatics. Further development is also necessary for the bioelectronics substrates described in Chapter 6. Chronic performance needs to be further studied, and there are concerns that long-term behavior might be compromised by polymer degradation due to the sensitivity of the esters in TMTMP to hydrolysis. In this case, an ester-free crosslinking molecule will need to be procured or, if possible, synthesized. Previously synthesized thiol-ene/acrylate devices tend to suffer from delamination and electronics failure over time *in vivo*. Similar studies need to be done on the thiourethane-based devices to determine if they suffer from the same effects. It may take a combination of substrate modification, encapsulation materials, and processing control to ensure that the electronics placed on the substrate are able to continue operating with predictable behavior in a chronic *in vivo* environment. The dielectric elastomer actuators demonstrated in Chapter 7 have a high dielectric constant, but fall short in actuation efficiency due to high stiffness and low breakdown strength. One potential route towards reducing stiffness is curing a thiol-ene/isocyanate hybrid polymer using the initiators shown in Chapter 3, although this would come at the expense of decreasing the dielectric constant. It is unclear if this will have a meaningful effect on the dielectric strength of the material, although this must be increased if the actuator is to compete with acrylic or silicone elastomers. While further development is needed to bring each of these applications to the world stage, this work shows the potential of polythiourethanes to bring exciting new properties to these fields.

APPENDIX

SUPPLEMENTARY FIGURES

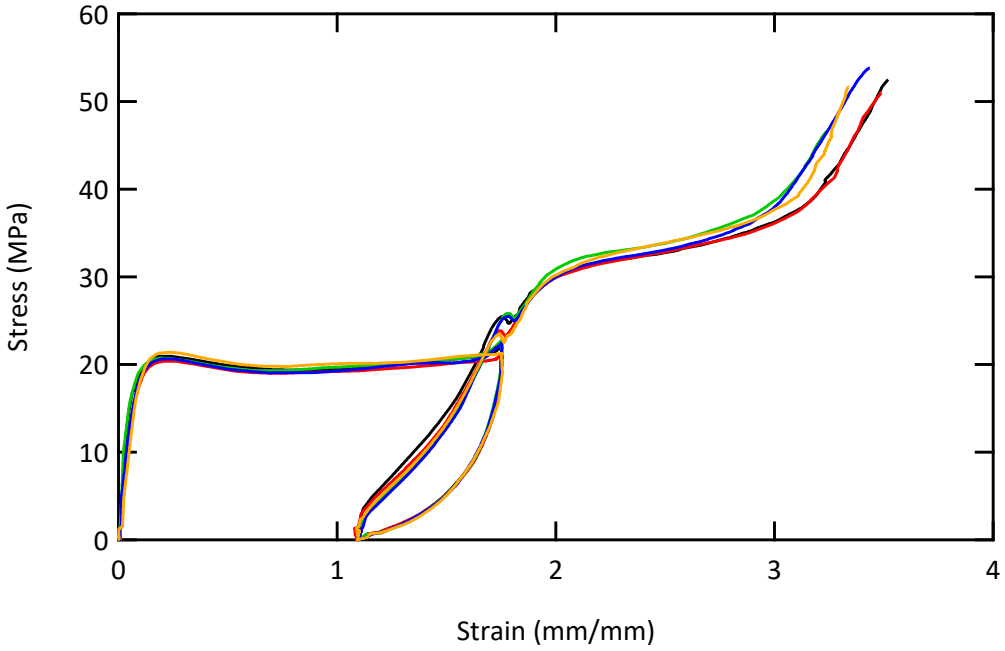

Figure A.1. Hysteretic behavior of a semi-crystalline polythiourethane thermoset

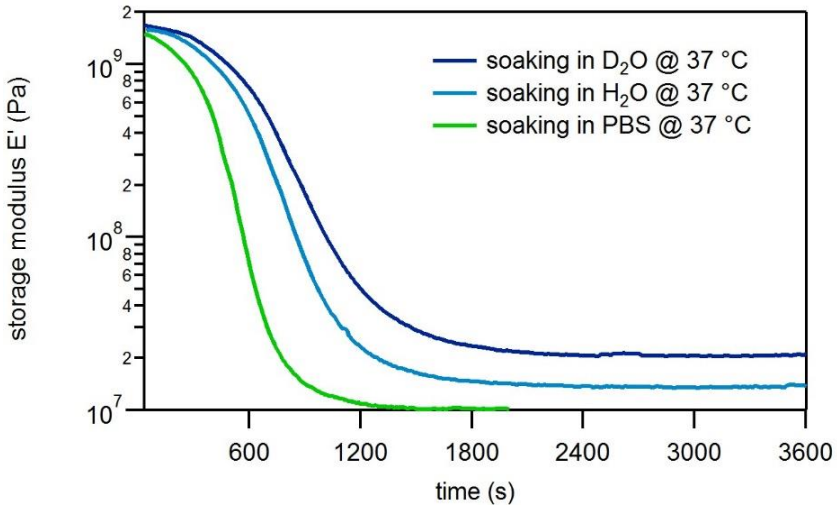

Figure A.2. Time-dependent softening behavior of TU-50 softening thiourethane substrate when exposed to different aqueous media

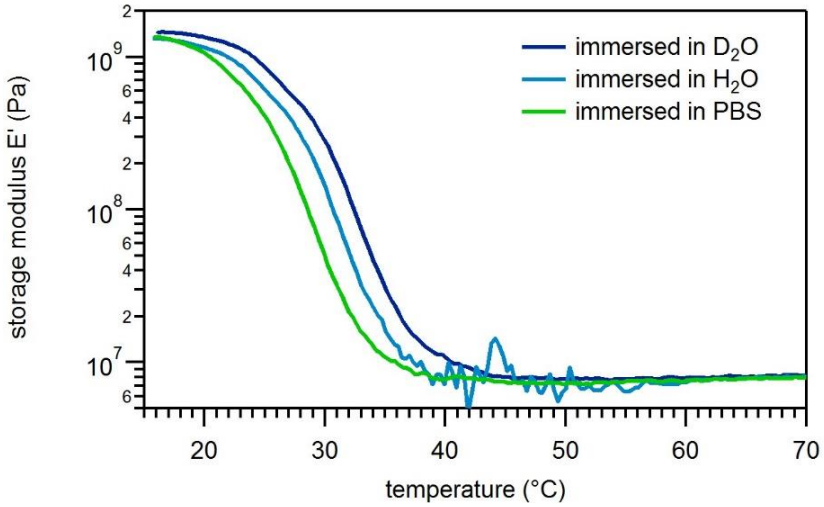

Figure A.3. Modulus as a function of temperature for the TU-50 thiourethane substrate when soaked in varying aqueous media

REFERENCES

1. R. Arnold, J. Nelson, J. Verbanc, Recent advances in isocyanate chemistry. *Chemical Reviews* **57**, 47-76 (1957).

2. H. C. Kolb, M. Finn, K. B. Sharpless, Click chemistry: diverse chemical function from a few good reactions. *Angewandte Chemie International Edition* **40**, 2004-2021 (2001).

3. C. E. Hoyle, A. B. Lowe, C. N. Bowman, Thiol-click chemistry: a multifaceted toolbox for small molecule and polymer synthesis. *Chemical Society Reviews* **39**, 1355-1387 (2010).

4. R. M. Hensarling *et al.*, Thiol–isocyanate "click" reactions: rapid development of functional polymeric surfaces. *Polymer Chemistry* **2**, 88-90 (2011).

5. H. Li, B. Yu, H. Matsushima, C. E. Hoyle, A. B. Lowe, The thiol− isocyanate click reaction: facile and quantitative access to ω-end-functional poly (N, N-diethylacrylamide) synthesized by RAFT radical polymerization. *Macromolecules* **42**, 6537-6542 (2009).

6. S. De, A. Khan, Efficient synthesis of multifunctional polymers via thiol–epoxy "click" chemistry. *Chemical Communications* **48**, 3130-3132 (2012).

7. E. Dyer, J. F. GLENN, E. G. LENDRAT, The Kinetics of the Reactions of Phenyl Isocyanate with Thiols1. *The Journal of Organic Chemistry* **26**, 2919-2925 (1961).

8. H. Matsushima, J. Shin, C. N. Bowman, C. E. Hoyle, Thiol-isocyanate-acrylate ternary networks by selective thiol-click chemistry. *Journal of Polymer Science Part A: Polymer Chemistry* **48**, 3255-3264 (2010).

9. J. Shin, H. Matsushima, J. W. Chan, C. E. Hoyle, Segmented Polythiourethane Elastomers through Sequential Thiol− Ene and Thiol− Isocyanate Reactions. *Macromolecules* **42**, 3294-3301 (2009).

10. J. Shin, H. Matsushima, C. M. Comer, C. N. Bowman, C. E. Hoyle, Thiol− Isocyanate− Ene Ternary Networks by Sequential and Simultaneous Thiol Click Reactions. *Chemistry of Materials* **22**, 2616-2625 (2010).

11. Z. Zhu, B. G. Risch, Z. Yang, Y.-N. Lin, "Optical thermoplastic thiourethane-urethane copolymers" US5679756 A (1997)

12. N. Nakayama, T. Hayashi, Synthesis of novel UV-curable difunctional thiourethane methacrylate and studies on organic–inorganic nanocomposite hard coatings for high refractive index plastic lenses. *Progress in Organic Coatings* **62**, 274-284 (2008).

13. C. E. Hoyle, T. Y. Lee, T. Roper, Thiol–enes: chemistry of the past with promise for the future. *Journal of Polymer Science Part A: Polymer Chemistry* **42**, 5301-5338 (2004).

14. J. A. Carioscia, J. W. Stansbury, C. N. Bowman, Evaluation and control of thiol–ene/thiol–epoxy hybrid networks. *Polymer* **48**, 1526-1532 (2007).

15. K. Dietliker *et al.*, Advancements in photoinitiators—Opening up new applications for radiation curing. *Progress in organic coatings* **58**, 146-157 (2007).

16. S. Katogi, M. Yusa, Photobase generation from amineimide derivatives and their use for curing an epoxide/thiol system. *Journal of Polymer Science Part A: Polymer Chemistry* **40**, 4045-4052 (2002).

17. M. Sangermano, A. Vitale, K. Dietliker, Photolatent amines producing a strong base as photocatalyst for the in-situ preparation of organic–inorganic hybrid coatings. *Polymer* **55**, 1628-1635 (2014).

18. C. M. Seubert, M. E. Nichols, Epoxy thiol photolatent base clearcoats: curing and formulation. *Journal of coatings technology and research* **7**, 615-622 (2010).

19. K. Suyama, M. Shirai, Photobase generators: recent progress and application trend in polymer systems. *Progress in Polymer Science* **34**, 194-209 (2009).

20. A. Kuramoto, M. Sumino, N. Sakai. "Photobase generator" US8957212 B2 (2015).

21. J.-X. Li, L. Liu, A.-H. Liu, Study on synthesis and photoactivity of N-substituted diazabicyclononane derivatives with different substituents. *International Journal of Adhesion and Adhesives* **57**, 118-124 (2015).

22. A. Sarker, D. Neckers, Tetraorganylborate salts as convenient precursors for photogeneration of tertiary amines. *Journal of the Chemical Society, Perkin Transactions 2*, 2315-2322 (1998).

23. A. M. Sarker, Y. Kaneko, A. V. Nikolaitchik, D. Neckers, Photoinduced Electron-Transfer Reactions: Highly Efficient Cleavage of CN Bonds and Photogeneration of Tertiary Amines 1. *The Journal of Physical Chemistry A* **102**, 5375-5382 (1998).

24. A. M. Sarker, Y. Kaneko, D. Neckers, Synthesis of tetraorganylborate salts: photogeneration of tertiary amines. *Chemistry of materials* **13**, 3949-3953 (2001).

25. A. Shiraishi, "Organic quaternary ammonium borate photobase generators, photocurable compositions containing them, and cured products of the compositions" JP 2014094974 (2014)

26. X. Zhang, W. Xi, C. Wang, M. Podgórski, C. N. Bowman, Visible-Light-Initiated Thiol-Michael Addition Polymerizations with Coumarin-Based Photobase Generators: Another Photoclick Reaction Strategy. *ACS Macro Letters* **5**, 229-233 (2016).

27. H. Tachi, M. Shirai, M. Tsunooka, Photolysis of Quaternary Ammonium Dithiocarbamates and Their Use as Photobase Generators. *Journal of Photopolymer Science and Technology* **13**, 153-156 (2000).

28. M. Tsunooka, H. Tachi, T. Yamamoto, K. Akitomo, M. Shirai, Stability of Quaternary Ammonium Salts in Various Solvents and their Use as Photobase Generators. *Journal of Photopolymer Science and Technology* **14**, 153-154 (2001).

29. H. Tachi, T. Yamamoto, M. Shirai, M. Tsunooka, Photochemical reactions of quaternary ammonium dithiocarbamates as photobase generators and their use in the photoinitiated thermal crosslinking of poly (glycidyl methacrylate). *Journal of Polymer Science Part A: Polymer Chemistry* **39**, 1329-1341 (2001).

30. M. Tsunooka, T. Yamamoto, Y. Kurokawa, K. Suyama, M. Shirai, Photocuring Systems Using Quaternary Ammonium Thiocyanates. *Journal of Photopolymer Science and Technology* **15**, 47-50 (2002).

31. K. Suyama, K. Fuke, M. Shirai, M. Tsunooka, Photo-and thermochemical behavior of quaternary ammonium thiocyanates and their use as crosslinkers. *Journal of Photopolymer Science and Technology* **16**, 83-86 (2003).

32. K. Suyama *et al.*, Photochemical formation of ammonium/thiolate complexes from quaternary ammonium thiocyanates and its use in crosslinking of polymers. *Journal of Photochemistry and Photobiology A: Chemistry* **179**, 87-94 (2006).

33. K. Suyama, K. Fuke, M. Shirai, Effect of anions on photoreactivity and stability of quaternary ammonium salts as photobase generators. *Journal of Photopolymer Science and Technology* **17**, 15-18 (2004).

34. K. Suyama, H. Araki, M. Shirai, Quaternary ammonium salt as DBU-generating photobase generator. *Journal of Photopolymer Science and Technology* **19**, 81-84 (2006).

35. H. Salmi, X. Allonas, C. Ley, Polythiourethane networks catalyzed by photobase generators. *Progress in Organic Coatings*, (2016).

36. I. Gibson, D. W. Rosen, B. Stucker, *Additive manufacturing technologies*. (Springer, 2010).

37. S. H. Huang, P. Liu, A. Mokasdar, L. Hou, Additive manufacturing and its societal impact: a literature review. *The International Journal of Advanced Manufacturing Technology* **67**, 1191-1203 (2013).

38. J.-P. Kruth, M.-C. Leu, T. Nakagawa, Progress in additive manufacturing and rapid prototyping. *CIRP Annals-Manufacturing Technology* **47**, 525-540 (1998).

39. I. Gibson, D. W. Rosen, B. Stucker, *Additive manufacturing technologies*. (Springer, 2010), vol. 238.

40. T. Wohlers, *Wohlers report 2016*. (Wohlers Associates, Inc, 2016).

41. P. F. Jacobs, *Rapid prototyping & manufacturing: fundamentals of stereolithography*. (Society of Manufacturing Engineers, 1992).

42. P. Sitthi-Amorn *et al.*, MultiFab: a machine vision assisted platform for multi-material 3D printing. *ACM Transactions on Graphics (TOG)* **34**, 129 (2015).

43. C. M. Yakacki, S. Willis, C. Luders, K. Gall, Deformation Limits in Shape-Memory Polymers. *Advanced Engineering Materials* **10**, 112-119 (2008).

44. D. L. Safranski, K. Gall, Effect of chemical structure and crosslinking density on the thermo-mechanical properties and toughness of (meth) acrylate shape memory polymer networks. *Polymer* **49**, 4446-4455 (2008).

45. W. K. Neo, M. B. Chan-Park, A New Model and Measurement Technique for Dynamic Shrinkage during Photopolymerization of Multi-Acrylates. *Macromolecular rapid communications* **26**, 1008-1013 (2005).

46. J. W. Stansbury *et al.*, Conversion-dependent shrinkage stress and strain in dental resins and composites. *Dental Materials* **21**, 56-67 (2005).

47. P. J. Bártolo, *Stereolithography: materials, processes and applications*. (Springer Science & Business Media, 2011).

48. B. Mueller, Additive Manufacturing Technologies–Rapid Prototyping to Direct Digital Manufacturing. *Assembly Automation* **32**, (2012).

49. Carbon 3D, "Rigid Polyurethane Technical Datasheet" (2016).

50. Carbon 3D. "Flexible Polyurethane Technical Datasheet" (2016).

51. Carbon 3D, "Elastomeric Polyurethane Technical Datasheet" (2016).

52. Carbon 3D, "Cyanate Ester Technical Datasheet" (2016).

53. J. R. Tumbleston *et al.*, Continuous liquid interface production of 3D objects. *Science* **347**, 1349-1352 (2015).

54. ASTM D638-14, Standard Test Method for Tensile Properties of Plastics, A. International, West Conshohocken, PA, 2014

55. ASTM D256-10e1, Standard Test Methods for Determining the Izod Pendulum Impact Resistance of Plastics, A. International, West Conshohocken, PA, 2010

56. R. J. Young, in *Comprehensive Polymer Science and Supplements*, G. A. C. Bevington, Ed. (Pergamon, Amsterdam, 1989), pp. 511-532.

57. A. Galeski, Strength and toughness of crystalline polymer systems. *Progress in Polymer Science* **28**, 1643-1699 (2003).

58. ASTM D648-16, Standard Test Method for Deflection Temperature of Plastics Under Flexural Load in the Edgewise Position, A. International, West Conshohocken, PA, 2016

59. Formlabs Inc., "FLTOTL03 Materials Properties Datasheet," (2016).

60. Formlabs Inc., "FLDUCL01 Material Properties Datasheet," (2017).

61. Stratasys Ltd., "PolyJet Materials Data Sheet," (2016).

62. J. E. Mark, *Polymer data handbook*. (Oxford University Press, 2009).

63. N. G. Hatsopoulos, J. P. Donoghue, The science of neural interface systems. *Annual review of neuroscience* **32**, 249-266 (2009).

64. D. R. Kipke *et al.*, Advanced neurotechnologies for chronic neural interfaces: new horizons and clinical opportunities. *The Journal of neuroscience : the official journal of the Society for Neuroscience* **28**, 11830-11838 (2008).

65. M. A. Nicolelis, Brain-machine interfaces to restore motor function and probe neural circuits. *Nature reviews. Neuroscience* **4**, 417-422 (2003).

66. A. B. Schwartz, X. T. Cui, D. J. Weber, D. W. Moran, Brain-controlled interfaces: movement restoration with neural prosthetics. *Neuron* **52**, 205-220 (2006).

67. M. Brus-Ramer, J. B. Carmel, S. Chakrabarty, J. H. Martin, Electrical stimulation of spared corticospinal axons augments connections with ipsilateral spinal motor circuits after injury. *The Journal of Neuroscience* **27**, 13793-13801 (2007).

68. J. B. Carmel, L. J. Berrol, M. Brus-Ramer, J. H. Martin, Chronic electrical stimulation of the intact corticospinal system after unilateral injury restores skilled locomotor control and promotes spinal axon outgrowth. *The Journal of Neuroscience* **30**, 10918-10926 (2010).

69. A. L. Benabid, S. Chabardes, J. Mitrofanis, P. Pollak, Deep brain stimulation of the subthalamic nucleus for the treatment of Parkinson's disease. *The Lancet. Neurology* **8**, 67-81 (2009).

70. M. P. Ward, P. Rajdev, C. Ellison, P. P. Irazoqui, Toward a comparison of microelectrodes for acute and chronic recordings. *Brain Res* **1282**, 183-200 (2009).

71. P. A. Tresco, B. D. Winslow, The challenge of integrating devices into the central nervous system. *Critical Reviews™ in Biomedical Engineering* **39**, (2011).

72. W. He, R. V. Bellamkonda, A molecular perspective on understanding and modulating the performance of chronic central nervous system (CNS) recording electrodes. (2008).

73. A. Prasad *et al.*, Comprehensive characterization and failure modes of tungsten microwire arrays in chronic neural implants. *Journal of neural engineering* **9**, 056015 (2012).

74. J. C. Barrese *et al.*, Failure mode analysis of silicon-based intracortical microelectrode arrays in non-human primates. *Journal of neural engineering* **10**, 066014 (2013).

75. J. C. Sanchez, N. Alba, T. Nishida, C. Batich, P. R. Carney, Structural modifications in chronic microwire electrodes for cortical neuroprosthetics: a case study. *Neural Systems and Rehabilitation Engineering, IEEE Transactions on* **14**, 217-221 (2006).

76. E. Patrick, M. E. Orazem, J. C. Sanchez, T. Nishida, Corrosion of tungsten microelectrodes used in neural recording applications. *Journal of neuroscience methods* **198**, 158-171 (2011).

77. K. A. Potter, A. C. Buck, W. K. Self, J. R. Capadona, Stab injury and device implantation within the brain results in inversely multiphasic neuroinflammatory and neurodegenerative responses. *Journal of neural engineering* **9**, 046020 (2012).

78. A. Gilletti, J. Muthuswamy, Brain micromotion around implants in the rodent somatosensory cortex. *Journal of neural engineering* **3**, 189 (2006).

79. P. Stice, A. Gilletti, A. Panitch, J. Muthuswamy, Thin microelectrodes reduce GFAP expression in the implant site in rodent somatosensory cortex. *Journal of Neural Engineering* **4**, 42 (2007).

80. T. Ware, D. Simon, R. L. Rennaker, W. Voit, Smart polymers for neural interfaces. *Polymer Reviews* **53**, 108-129 (2013).

81. J. Harris *et al.*, Mechanically adaptive intracortical implants improve the proximity of neuronal cell bodies. *Journal of neural engineering* **8**, 066011 (2011).

82. A. Sridharan, J. K. Nguyen, J. R. Capadona, J. Muthuswamy, Compliant intracortical implants reduce strains and strain rates in brain tissue in vivo. *Journal of neural engineering* **12**, 036002 (2015).

83. J. R. Capadona, D. J. Tyler, C. A. Zorman, S. J. Rowan, C. Weder, Mechanically adaptive nanocomposites for neural interfacing. *MRS bulletin* **37**, 581-589 (2012).

84. T. Ware *et al.*, Fabrication of responsive, softening neural interfaces. *Advanced Functional Materials* **22**, 3470-3479 (2012).

85. T. Ware *et al.*, Thiol-ene/acrylate substrates for softening intracortical electrodes. *Journal of Biomedical Materials Research Part B: Applied Biomaterials* **102**, 1-11 (2014).

86. J. Reeder *et al.*, Mechanically adaptive organic transistors for implantable electronics. *Advanced Materials* **26**, 4967-4973 (2014).

87. P. Brochu, Q. Pei, Advances in dielectric elastomers for actuators and artificial muscles. *Macromolecular rapid communications* **31**, 10-36 (2010).

88. R. Pelrine *et al.*, in *SPIE's 9th Annual International Symposium on Smart Structures and Materials*. (International Society for Optics and Photonics, 2002), pp. 126-137.

89. T. Mirfakhrai, J. D. Madden, R. H. Baughman, Polymer artificial muscles. *Materials today* **10**, 30-38 (2007).

90. F. Carpi, D. De Rossi, R. Kornbluh, R. E. Pelrine, P. Sommer-Larsen, *Dielectric elastomers as electromechanical transducers: Fundamentals, materials, devices, models and applications of an emerging electroactive polymer technology*. (Elsevier, 2011).

91. R. Pelrine *et al.*, High-field deformation of elastomeric dielectrics for actuators. *Materials Science and Engineering: C* **11**, 89-100 (2000).

92. R. D. Kornbluh *et al.*, in *1999 Symposium on Smart Structures and Materials*. (International Society for Optics and Photonics, 1999), pp. 149-161.

93. R. Pelrine, R. Kornbluh, Q. Pei, J. Joseph, High-speed electrically actuated elastomers with strain greater than 100%. *Science* **287**, 836-839 (2000).

94. R. Pelrine, R. Kornbluh, G. Kofod, High-Strain Actuator Materials Based on Dielectric Elastomers. *Advanced Materials* **12**, 1223-1225 (2000).

95. S. Michel, X. Q. Zhang, M. Wissler, C. Löwe, G. Kovacs, A comparison between silicone and acrylic elastomers as dielectric materials in electroactive polymer actuators. *Polymer international* **59**, 391-399 (2010).

96. B. Kussmaul *et al.*, Enhancement of dielectric permittivity and electromechanical response in silicone elastomers: molecular grafting of organic dipoles to the macromolecular network. *Advanced Functional Materials* **21**, 4589-4594 (2011).

97. B. Kussmaul, S. Risse, M. Wegener, G. Kofod, H. Krüger, Matrix stiffness dependent electro-mechanical response of dipole grafted silicones. *Smart Materials and Structures* **21**, 064005 (2012).

98. C. G. Cameron, R. S. Underhill, M. Rawji, J. P. Szabo, in *Smart Structures and Materials*. (International Society for Optics and Photonics, 2004), pp. 51-59.

99. G. Gallone, F. Carpi, D. De Rossi, G. Levita, A. Marchetti, Dielectric constant enhancement in a silicone elastomer filled with lead magnesium niobate–lead titanate. *Materials Science and Engineering: C* **27**, 110-116 (2007).

100. B. Guiffard, L. Seveyrat, G. Sebald, D. Guyomar, Enhanced electric field-induced strain in non-percolative carbon nanopowder/polyurethane composites. *Journal of Physics D: Applied Physics* **39**, 3053 (2006).

101. F. Carpi, D. D. Rossi, Improvement of electromechanical actuating performances of a silicone dielectric elastomer by dispersion of titanium dioxide powder. *IEEE Transactions on Dielectrics and Electrical Insulation* **12**, 835-843 (2005).

102. W. Hu, S. N. Zhang, X. Niu, C. Liu, Q. Pei, An aluminum nanoparticle–acrylate copolymer nanocomposite as a dielectric elastomer with a high dielectric constant. *Journal of Materials Chemistry C* **2**, 1658-1666 (2014).

103. J. G. Speight, *Lange's handbook of chemistry*. (McGraw-Hill New York, 2005), vol. 1.

BIOGRAPHICAL SKETCH

Gregory Ellson grew up in Briarcliff Manor, New York. He had an early interest in the sciences and as a sophomore in high school was lucky to receive the opportunity to perform shape memory polymer research with Dr. Ken Gall and then-PhD student Walter Voit at The Georgia Institute of Technology. The guidance and support he received allowed him to become an Intel Science Talent Search National Semi-Finalist and set him upon a path of research into novel polymers. While an undergraduate at Georgia Tech, he helped develop orthopedic implants utilizing shape memory polymers and graduated with a BS in mechanical engineering in the Class of 2014. He then chose to pursue his PhD in materials science & engineering at The University of Texas at Dallas where Dr. Walter Voit is now a tenured Associate Professor.

CURRICULUM VITAE

Gregory Ellson

Gregory.Ellson@utdallas.edu

EDUCATION

Doctor of Philosophy in Materials Science & Engineering, GPA 3.81 (07/2017)
THE UNIVERSITY OF TEXAS AT DALLAS, Richardson, TX

Master of Science in Materials Science & Engineering, GPA 3.78 (08/2016)
THE UNIVERSITY OF TEXAS AT DALLAS, Richardson, TX

Bachelor of Science in Mechanical Engineering, GPA 3.49 (05/2014)
GEORGIA INSTITUTE OF TECHNOLOGY, Atlanta, GA

RESEARCH EXPERIENCE

2014 – 2017 — The University of Texas at Dallas — Richardson, TX
Eugene McDermott Graduate Research Fellow
- Development of high toughness, high heat deflection temperature photopolymers for additive manufacturing
- Design of lithography-compatible substrates for bioelectronic devices

2013 - 2014 — The University of Texas at Dallas — Richardson, TX
Undergraduate Research Assistant
- Synthesis and characterization of thiol-epoxy foams for neural interfaces

2011 – 2012 — Medshape, Inc — Atlanta, GA
Materials Researcher
- Characterized shape memory response of available surgical plastics
- Development of PEEK shape memory surgical implants

2009 - 2010 — Georgia Institute of Technology — Atlanta, GA
Undergraduate Research Assistant
- Synthesis and characterization of shape memory polymer composites

TECHNICAL SKILLS

- Synthetic chemistry (Custom visible-light photo-catalysts)
- Polymer chemistry & synthesis (Tough thermosets & thermoplastics for SLA and FFF 3D printing, polymer substrates for flexible electronics & bioelectronic devices)

- Materials characterization (thermogravimetric analysis, differential scanning calorimetry, dynamic mechanical analysis, universal testing machines, Fourier-transform infrared spectroscopy, nuclear magnetic resonance spectroscopy, UV-visible spectroscopy, XRD
- 3D Printing (Custom printer design, fabrication, software coding, and use)
- Machining (mill, lathe)
- Software programming (Matlab, Python)
- Project & team management (Managed tasks & finances of 10+ person team over two years)

PUBLICATIONS & PRESENTATIONS

G. Ellson, X .Carrier, T.J. Wallin, W.E. Voit. Tough thiourethane photopolymers with tunable crystallinity for additive manufacturing. *Science.* (Under Review)

G. Ellson, X. Carrier, J. Walton, S.F. Mahmood, K. Yang, J. Salazar, W.E. Voit. Tough Thiourethane Thermoplastics for Fused Filament Fabrication. *Journal of Applied Polymer Science.* (Under Revision)

G. Ellson, X. Carrier, B. Lund. W.E. Voit. Tough stereolithography 3D printing via thiol-isocyanate photopolymerization. *Shape Memory Applications, Research, and Technology Symposium*. (2016)

G. Ellson, K. Yang, B. Lund, W.E. Voit. New chemistries for tough, isotropic additive manufacturing. *Materials Research Society Fall National Meeting*. (2016)

G. Ellson, Y. Qattan, T. Blair, R. Modi, W.E. Voit. Thiol-isocyanate substrates for durable, softening neural electronics. *Materials Research Society Fall National Meeting*. (2016)

G. Ellson, X. Carrier, B. Lund. W.E. Voit. Tough stereolithography resins through thiol-isocyanate photopolymerization. *Materials Research Society Fall National Meeting*. (2016)

G. Ellson, R. Smaldone, B. Lund. W.E. Voit. Quaternary Ammonium Salta for Rapid Long-Wavelength Photopolymerization of Polythiourethanes. *5th Texas Soft Matter Meeting*. (2016)

E. Bolivar, D. Allen, **G. Ellson**, J. Cossio, W.E. Voit, R Gregg. Towards a series elastic actuator with electrically modulated stiffness for Powered Ankle-Foot Orthoses. *Automation Science and Engineering (CASE)* 1086-1093. (2016)

G. Ellson, K. Yang, B. Lund, W.E. Voit. New chemistries for tough, isotropic additive manufacturing. *252nd American Chemical Society National Meeting*. (2016)

G. Ellson, Y. Qattan, T. Blair, R. Modi, W.E. Voit. Thiol-isocyanate substrates for durable, softening neural electronics. *252nd American Chemical Society National Meeting*. (2016)

S. Parker, R. Reit, H. Abitz, **G. Ellson**, K. Yang, B. Lund, W.E. Voit. High-Tg Thiol-Click Thermoset Networks via the Thiol-Maleimide Michael Addition. *Macromolecular rapid communications* 37: 1027–1032. (2016)

G. Ellson, X. Carrier, B. Lund, W.E. Voit. Ultra-Tough Aliphatic Thiol-Isocyanate Elastomers Achieved Through Thiol-Click Reactions. *251st American Chemical Society National Meeting*. (2016)

K.V. Maaraoui, **G. Ellson**, W.E. Voit. Hybrid cured thiol-ene/epoxy networks for core-shell semiconductor packaging. *MRS Advances* 1 (01), 57-62. (2016)

G. Ellson, M. Di Prima, T. Ware, X. Tang, W.E. Voit. Tunable thiol–epoxy shape memory polymer foams. *Smart Materials and Structures* 24 (5), 055001. (2015)

T. Ware, **G. Ellson**, A. Kwasnik, S. Drewicz, K. Gall, W.E. Voit. Tough shape-memory polymer-fiber composites. *Journal of Reinforced Plastics and Composites* 30 (5), 371-380. (2011)